



# **POLITECNICO DI TORINO**

Master Degree in Mechanical Engineering

Master Degree Thesis

## **Characterization of Metamaterials through Advanced Beam Elements**

Supervisors:

**Prof. Maria Cinefra**

**Prof. Alfonso Pagani**

**Prof. Alberto García De Miguel**

Candidate:

**Luca Mucelli**

---

July, 2019



*A chi non ci puo' essere,  
ma c'e' sempre*

*Non andartene docile in quella buona notte,  
i vecchi dovrebbero bruciare e delirare al serrarsi del giorno;  
infuria, infuria, contro il morire della luce.*

*Benche' i saggi conoscano alla fine che la tenebra e' giusta  
perche' dalle loro parole non diramarono fulmini  
non se ne vanno docili in quella buona notte.*

*I probi, con l'ultima onda, gridando quanto splendide  
le loro deboli gesta danzerebbero in una verde baia,  
s'infuriano, s'infuriano contro il morire della luce.*

*Gli impulsivi che il sole presero al volo e cantarono,  
troppo tardi imparando d'averne afflitto il cammino,  
non se ne vanno docili in quella buona notte.*

*Gli austeri, prossimi alla morte, con cieca vista accorgendosi  
che occhi spenti potevano brillare come meteore e gioire,  
s'infuriano, s'infuriano contro il morire della luce.*

*E tu, padre mio, la sulla triste altura maledicimi,  
benedicimi, ora, con le tue lacrime furiose, te ne prego.  
Non andartene docile in quella buona notte.  
Infuriati, infuriati contro il morire della luce.*

*Dylan Thomas, 1965*



# Summary

The thesis work is set in development and extension of  $MUL^2$  micromechanics code, based on CUF, or well known as Carrera Unified Formulation.

Carrera Unified formulation is a class of theories of Structure on which Finite Elements are formulated. Its main aim is to lighten FEM analysis computational costs and to cover a wide range of field of application. The thesis work is focused on applying CUF to metamaterials analysis, it could be divided into five main parts:

- Training: one month-long period spent to learn about how to use  $MUL^2$  micromechanics code, namely how to create input files and to become familiar with *Fortran* programming language.
- Code Implementation: four months-long period used to create a new tool able to provide metamaterial unit cell dispersion curves and modes of vibration.
- Benchmarking: two months-long period with the aim to look for similar works in literature, useful to be used as solid benchmark for understanding if the new code effectively works in the correct way.
- Obtaining transmission curves: a month-long period where have been carried out dynamic analysis in order to capture the transmission properties of an array composed of few metamaterial unit cells. The utility of this kind of graph is to be compared with the dispersion curves, in order to check out the bandgap position.
- Case study: three-month period (May, June, July) spent at California Institute of technology in Pasadena, CA. In this period have been carried out further refinements to the code and it has been studied a new metamaterial, provided by the European project CASTLE, composed of a Melamine Foam matrix with cylindrical Aluminum inclusion. Finally, a parametric analysis is carried out by varying the relative dimension proportion of matrix and inclusion.

The visiting period at California Institute of technology has been an outstanding growth period, that gives the possibility to learn about a wide range of aspects related to metamaterials and to work and collaborate with subject matter experts.



# Table of contents

<b>Summary</b>	III
<b>1 Introduction</b>	<b>1</b>
1.1 Metamaterials . . . . .	1
1.2 Relevant Metamaterials Application in Aeronautics . . . . .	2
1.3 The CASTLE Project . . . . .	3
1.3.1 Main Purpose regarding the Thesis Work . . . . .	3
1.3.2 Overview of CASTLE Project . . . . .	5
<b>2 Theory</b>	<b>7</b>
2.1 Carrera Unified Formulation . . . . .	7
2.1.1 Introduction . . . . .	7
2.1.2 The Finite Element Method (FEM) . . . . .	7
2.1.3 Fundamental Nuclei Definition . . . . .	11
2.1.4 Matrices Assembly . . . . .	12
2.1.5 An Unique Approach . . . . .	12
2.1.6 Resume . . . . .	13
2.2 Introduction to Micromechanics . . . . .	16
2.2.1 Introduction . . . . .	16
2.2.2 Main Definitions . . . . .	16
2.2.3 Mechanics of Structure Genome . . . . .	17
2.3 Metamaterials . . . . .	18
2.3.1 Introduction . . . . .	18
2.3.2 Acoustic Metamaterials and Phononic Crystals . . . . .	18
2.3.3 Origin of Negative Density in Acoustic Metamaterials . . . . .	20
2.3.4 Bragg Scattering . . . . .	23
2.3.5 Local Resonances . . . . .	25
2.3.6 Bragg Scattering vs Local Resonance . . . . .	27
2.4 Methods to Compute the Dispersion Relation for the Wave Propagation Characterization of a Periodic Medium . . . . .	29
2.4.1 Introduction . . . . .	29
2.4.2 Finite Element Method for 1D Problem . . . . .	29
<b>3 Training and Introductory Numerical Analysis</b>	<b>31</b>
3.1 Premises . . . . .	31
3.2 Circular fibre in square pack analysis . . . . .	32
3.2.1 Boron-Aluminum . . . . .	32

3.2.2	Graphite-epoxy . . . . .	33
3.3	Circular fibre in hexagonal pack analysis . . . . .	34
3.4	Square fibre in square pack with interface . . . . .	37
3.4.1	Square fibre, square interface in a square pack . . . . .	38
3.4.2	Original circular fibre, circular interface in a square pack . . . . .	39
3.5	First dynamic analysis . . . . .	40
3.5.1	Physical meaning of the analysis and introduction to acoustic metamaterials . . . . .	42
<b>4</b>	<b>Benchmark Analysis Evidence</b>	<b>45</b>
4.1	Introduction . . . . .	45
4.2	Langlet: Homogeneous and Isotropic Material . . . . .	47
4.3	Langlet: Square Inclusion . . . . .	49
4.4	Geers . . . . .	51
4.5	Wang: Dispersion Curves . . . . .	53
4.6	Wang: Transmission curves . . . . .	59
<b>5</b>	<b>Case Study: Metamaterial for Aeronautical Applications</b>	<b>65</b>
5.1	Introduction . . . . .	65
5.2	Melamine Foam and Aluminum properties . . . . .	66
5.3	Geometrical features . . . . .	68
5.4	Mesh . . . . .	68
5.5	Dispersion Curves . . . . .	68
5.5.1	Bandgap Analysis . . . . .	70
5.6	Transmission Curves . . . . .	74
5.6.1	Pressure Wave Polarization . . . . .	74
5.6.2	Shear Wave Polarization . . . . .	74
5.7	Parametric Analysis . . . . .	76
<b>6</b>	<b>Conclusions</b>	<b>79</b>
	<b>Bibliography</b>	<b>81</b>



# List of figures

1.1	Section of the fuselage trunk [1] . . . . .	2
1.2	Components of the fuselage section [1] . . . . .	3
1.3	Heterogeneous metamaterial panel with a focus in the meaning of mass - spring - damper system [2]. . . . .	4
2.1	Local reference system and node numeration of a bar [3] . . . . .	8
2.2	Example of linear shape function in a two nodes bar element [3] . . . . .	9
2.3	Matrices assembly process [3] . . . . .	12
2.4	Example of FEM models [3] . . . . .	13
2.5	Approaches for the three dimensions [3] . . . . .	14
2.6	CUF resuming table [3] . . . . .	15
2.7	Different UCs choices [4] . . . . .	17
2.8	Structure Genome creation for a 3D structure [4] . . . . .	18
2.9	Hidden and external forces for the case of a rolling wheel [5] . . . . .	20
2.10	Normalized plot of the effective mass as a function of the hidden force [5] . . . . .	21
2.11	Hidden and external forces for the case of a simple harmonic oscillator [5] . . . . .	22
2.12	Unit cell and Acoustic Metamaterial sketch [5] . . . . .	23
2.13	Normalized plot of the effective density as a function of frequency [5] . . . . .	24
2.14	Types of interference [6] . . . . .	24
2.15	Two equal scatterers at a distance $\Delta x$ [6] . . . . .	25
2.16	Band gap of a phononic crystal [6] . . . . .	25
2.17	Two oscillators coupled [6] . . . . .	26
2.18	(a) Effect of the coupling $\gamma$ on the eigenfrequency of the two oscillators. (b) Wave dispersion (black) and the location of a local resonance (blue). (c) Coupling the local resonance to the wave leads to the opening of a band gap at the frequency $\omega_0$ of the local resonance [6] . . . . .	27
3.1	Different configurations Fibre-matrix and their domain . . . . .	32
3.2	HLE beam model of the hexagonal pack cell RUC . . . . .	34
3.3	. . . . .	36
3.4	. . . . .	36
3.5	Cell geometry sketch [7] . . . . .	37
3.6	Representation of square meshes employed . . . . .	39
3.7	Longitudinal stress $\sigma_{yy}$ generated by unitary longitudinal strain in all directions . . . . .	39
3.8	Deformation $\epsilon_{xx}$ generated by unitary longitudinal strain in all directions . . . . .	40
3.9	Representation of the original geometry mesh . . . . .	41
3.10	Longitudinal stress $\sigma_{yy}$ (a) and deformation $\epsilon_{xx}$ (b) generated by unitary longitudinal strain in all directions . . . . .	41

3.11	Homogenizable region [8] . . . . .	42
4.1	Unit cell mesh for homogeneous and isotropic material . . . . .	47
4.2	Comparison between dispersion curves for a homogeneous and isotropic elastic medium obtained with $MUL^2$ micromechanics code (a) and obtained by Langlet et al. [9] . . . . .	48
4.3	Main views of the first and second mode at $0.68339 \cdot 10^5 Hz$ . . . . .	48
4.4	Unit cell configuration with a square brass inclusion: geometric sketch (a) and mesh model used (b) [9]. . . . .	49
4.5	Comparison between Langlet dispersion curve (a) [9] and dispersion curves obtained with $MUL^2$ micromechanics code (b). . . . .	50
4.6	Main views of the first and second mode at $0.6114 \cdot 10^5 Hz$ . . . . .	50
4.7	Dispersion curve obtained by $MUL^2$ micromechanics code. . . . .	51
4.8	Modes obtained by $MUL^2$ micromechanics code. . . . .	52
4.9	Modes obtained by Geers et al. [10] . . . . .	52
4.10	Phononic crystal geometry sketch [11] . . . . .	54
4.11	$\Gamma - X - M$ path delimiting the first Brillouin zone [11] . . . . .	55
4.12	Dispersion curves obtained by Wang et al. [12] . . . . .	55
4.13	Dispersion curves obtained by $MUL^2$ micromechanics code showing extreme band-gap modes. . . . .	56
4.14	Comparison of the S3 point mode between $MUL^2$ micromechanics code and Wang et al. results . . . . .	56
4.15	Comparison of the S4 point mode between $MUL^2$ micromechanics code and Wang et al. results . . . . .	57
4.16	Full reduced dispersion curves obtained by $MUL^2$ micromechanics code. . . . .	57
4.17	Full dispersion curves obtained by $MUL^2$ micromechanics code. . . . .	58
4.18	Transmission curves analysis set up . . . . .	59
4.19	Transmission curve for a x-polarized plane wave . . . . .	61
4.20	Detail of the transmission curve for a x-polarized plane wave, showing most important modes shapes . . . . .	61
4.21	Transmission curve for a z-polarized plane wave . . . . .	62
4.22	Detail of the transmission curve for a z-polarized plane wave, showing most important modes shapes . . . . .	62
4.23	Transmission curves for both x- and z- polarized plane waves . . . . .	63
4.24	Transmission curves for both x- and z-polarized plane waves obtained by Wang [11] . . . . .	63
5.1	Melamine chemical description [13] . . . . .	65
5.2	Transmission curve plotted by Wang et al. by changing the matrix viscosity coefficient [11]. . . . .	67
5.3	Periodic Unit Cell of the metamaterial with matrix of viscoelastic foam and cylindrical inclusions of aluminum [1]. . . . .	69
5.4	Mesh model of the array composed by eight Unit Cells mad with Abaqus. . . . .	69
5.5	First Irreducible Brillouin Zone for an orthotropic material [14]. . . . .	70
5.6	Complete Melammine-Aluminum metamaterial dispersion curve. . . . .	71
5.7	First five modes of propagation in the $\Gamma - X_1$ direction for $k = 0$ . . . . .	71
5.8	First four modes of propagation in the $\Gamma - X_1$ direction for $k = 0.5$ . . . . .	72
5.9	First four modes of propagation in the $\Gamma - X_1$ direction for $k = 1$ . . . . .	72
5.10	First five modes of propagation in the $X_1 - M$ direction for $k = 0.5$ . . . . .	73
5.11	First five modes of propagation in the $X_1 - M$ direction for $k = 1$ . . . . .	73

5.12	Comparison between Melamine-Aluminum metamaterial dispersion and transmission curves for pressure wave polarization case. . . . .	74
5.13	Mode propagation analysis of the most relevant points of pressure wave polarization transmission curve. . . . .	75
5.14	Comparison between Melamine-Aluminum metamaterial dispersion and transmission curves for shear wave polarization case. . . . .	75
5.15	Bandgap width by varying the volume fraction of the Unit Cell . . . . .	76
5.16	Graphical evolution of the bandgap width by increasing volume fraction. . . . .	77



# List of tables

2.1	CUF formulation for the three dimensions . . . . .	13
2.2	Expansions for the three dimensions . . . . .	13
3.1	Boron-Aluminum composite properties . . . . .	33
3.2	Effective properties of the Boron-Aluminum cell (square pack). . . . .	33
3.3	Graphite-Epoxy composite properties . . . . .	33
3.4	Effective properties of the Graphite-Epoxy cell (square pack). . . . .	34
3.5	Carbon-Epoxy composite properties . . . . .	34
3.6	Effective properties of the Carbon-Epoxy cell (square pack): Young and shear modulus. . . . .	35
3.7	Effective properties of the Carbon-Epoxy cell (square pack): Poisson's coefficient. . . . .	35
3.8	Composite material properties . . . . .	37
3.9	Model geometry features . . . . .	37
3.10	Properties of the two mesh considered . . . . .	38
3.11	Effective properties of the Epoxy-Silicone-Lead cell (square pack, square fibre and square interface): Young and shear modulus. . . . .	38
3.12	Effective properties of the Epoxy-Silicone-Lead cell (square pack, square fibre and square interface): Poisson's coefficient. . . . .	38
3.13	Circular mesh properties . . . . .	40
3.14	Effective properties of the Epoxy-Silicone-Lead cell (original model): Young and shear modulus. . . . .	40
3.15	Effective properties of the Epoxy-Silicone-Lead cell (original model): Poisson's coefficient. . . . .	41
4.1	Aluminum properties . . . . .	47
4.2	Brass properties . . . . .	49
4.3	Phononic crystal geometry properties . . . . .	53
4.4	Phononic crystal materials properties [12] . . . . .	53
4.5	Three main directions of the first Brillouine zone [11] . . . . .	55
5.1	Density and Real Young modulus for Melamine [2]. . . . .	67
5.2	Real Shear modulus for Melamine [2]. . . . .	68
5.3	Poisson coefficient for Melamine [2]. . . . .	68
5.4	Properties for Aluminum [2]. . . . .	68
5.5	Geometric features of the Unit Cell [1]. . . . .	69



# Chapter 1

## Introduction

### 1.1 Metamaterials

Metamaterials have been a hot-topic in the past ten years in the scientific communities and this has driven their development. The scientific communities excitement is due to the countless application fields they could cover, that are almost infinite: medical, aeronautical, mechanical, civil applications are only few of the complete list of functions they could cover.

For definition, a metamaterial (from the Greek word meta, meaning "beyond") is a material engineered to have properties that are not found in naturally occurring materials. They are made from assemblies of multiple elements fashioned from composite materials such as metals and plastics. The materials are usually arranged in repeating patterns, at scales that are smaller than the wavelengths of the phenomena they influence.

Metamaterials derive their properties not completely from the properties of the materials they are composed of, but from their newly purposely designed structures. Their precise shape, geometry, size, orientation and arrangement gives them their smart properties capable of manipulating electromagnetic waves: by blocking, absorbing, enhancing, or bending waves, to achieve benefits that go beyond what is possible with conventional materials [15].

Appropriately designed metamaterials can affect waves of electromagnetic radiation or sound in a manner not observed in bulk materials. Some of them exhibit a negative index of refraction for particular wavelengths, these materials are known as negative-index metamaterials.

There are different type of metamaterials: optical, electromagnetic, mechanical and even robotics, but this work is going to take into consideration only acoustic metamaterials.

An acoustic metamaterial could consists of a periodic locally resonant structure (lattice or inclusion type), able to create bandgaps, namely windows in the dispersion graph, where no frequency can propagate. Bandgaps are useful for cloaking and soundproofing, and they can be induced, by varying the geometric feature of the unit cells they are composed, at lower and higher frequencies. In acoustics, low frequency ranges are really complex to absorb with conventional materials, because the order of magnitude of the sound wavelength is more or less of one meter. One can imagine how much difficult it would be to build and use a damping system with a thickness of one meter. Through local resonance and Bragg scattering phenomena, acoustic metamaterials are able to perform better than conventional material because their structure is such that they do not respect physical properties like positive density or bulk modulus on a global scale at resonance. Naturally, they locally respect at any time all the physical laws.

An important aspect related and necessary to study a generic metamaterial is the *homogenization*,

namely the method able to transform a heterogeneous material with inclusion or holes into an equivalent homogeneous material with identical mechanical behaviour. This method is worth to be mentioned because its aim is to avoid meshing holes of the real material in Finite Element codes and therefore to improve computation time and costs of the analysis.

## 1.2 Relevant Metamaterials Application in Aeronautics

Modern technologies applications require materials able to provide peculiar combinations of different properties, that are not found in traditional materials as metal alloys, ceramics or polymers.

As far as the aeronautical applications are concerned, structural materials presenting low density, good stiffness, high resistance and low corrosion properties are sought after.

Generally, high stiffness materials present high density, and the increase of stiffness brings to a decrease of impact resistance.

By using the so called *composite materials*, has been possible to combine different properties in a unique material and to expand the range of applications.

The majority of composite materials are composed of a *matrix* and a *phase*, and their final properties are called *homogenized properties* and they strongly depend on the constituent phases, their relative quantities and geometries.

Considering this general concept, it is possible to consider an acoustic metamaterial as a composite material.

Acoustic metamaterials can be used as solution to the problem of noise vibration in the cabin, by covering the fuselage with a metamaterial layer. In figures 1.1 and 1.2 are represented briefly some schemes of the fuselage composition and dimensions, [1].

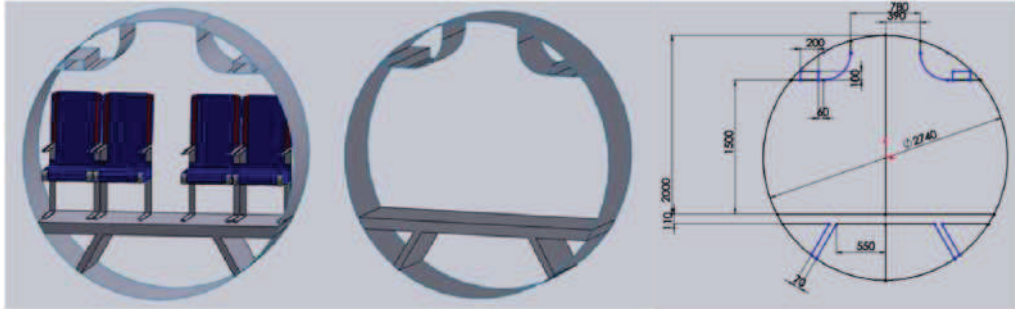


Figure 1.1: Section of the fuselage trunk [1]

As far as the problem of the cabin soundproofing is concerned, it is worth to remind that regulations like FAR and EASA have to be considered as safety standards. These regulation do not provide a quantitative information of internal noise requirement, but only a qualitative indication. As Cinefra et al. [2] describe, standards highlight safety aspect and for the sake of clarity some examples can be provided.

For instance, it is requested that vibration and noise of cockpit equipment do not interfere with safe operation of the aircraft, and that means that noise levels should allow a safe and easy communication among pilots and flight crewmembers, but also that they should not cause distraction or nuisance. As explained in [1], noise in civil airplanes is mainly produced by two sources: fuselage boundary layers and turbojet exhaust.

Other four relevant sources are turbomachinery, cabin conditioning and pressurization system, structure and aerodynamic flow.



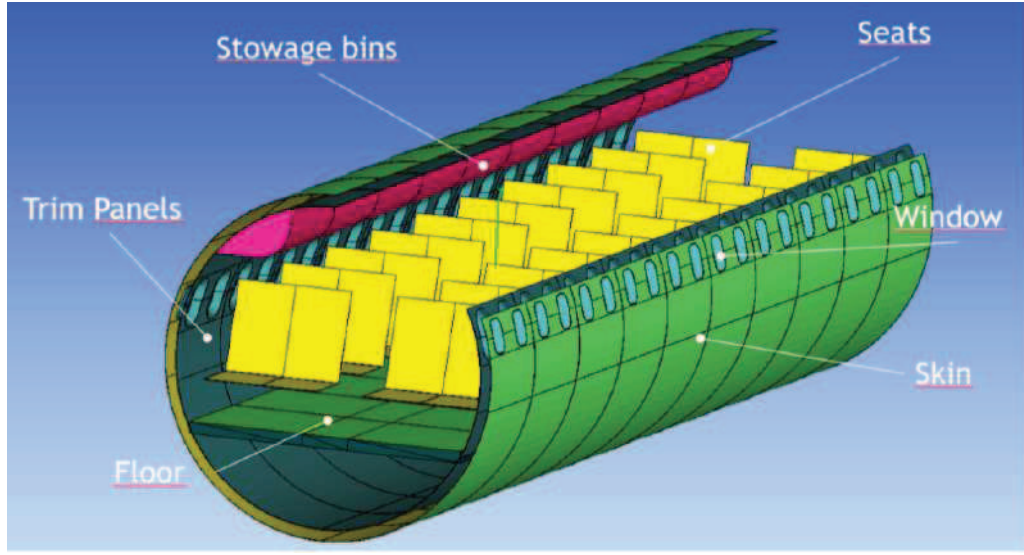


Figure 1.2: Components of the fuselage section [1]

Noise is transmitted to the cabin along airborne paths through the fuselage sidewall and along structure borne paths through the engine mounts or the wing structure.

Every airplane has its own characteristic sound, used by pilots as a diagnosis system. Usually, sound pressure level is comprised between 60 and 88  $dB$ , but it has been experienced that a long exposure over 85  $dB$  could cause hearing lost. Considering that for a turboprop airplane the near field noise excitation is mainly due to the propeller and then the major part of the acoustic energy is concentrated in the low frequency range ( $0 - 200Hz$ ).

An aspect of fundamental importance in defining internal noise requirements is referred to the acoustic treatments (all the technical solutions or means installed on board) to increase the noise attenuation through the fuselage wall and to control the internal noise sources.

Thermo - acoustic blankets, skin damping, furnishing panels, mufflers and active noise control system are examples of noise treatment items. Basically, the system configuration needs to be designed taking into account several parameters, but the two most important factors that cover really important role (in aeronautic applications) are weight and cost.

As far as the weight is concerned, if a regional turboprop is considered, the mass of fuselage blankets should be less than the 1.4% of the MEW (Manufacturer's Empty Weight, the weight of the aircraft "as built").

## 1.3 The CASTLE Project

### 1.3.1 Main Purpose regarding the Thesis Work

The main purpose of this thesis work is to contribute to the development of CASTLE project. The study case provided in chapter 5 aims to study and analyse the proposed Melamine - Aluminum metamaterial, applied as a layer covering the fuselage of a turboprop regional airplane.

The novelty that has been made is the complete definition and study of the lower bandgap presented by the orthotropic metamaterial. Dispersion and transmission relation has been obtained and

plotted so that it may be possible to compare them. Moreover, a parametrical analysis has been done with the aim of find an "optimum" in terms of bandgap width by changing the volume fraction of the unit cell.

A contribution that is worth to mention is the work of Cinefra et al. [2] [1], where a numerical evaluation of the transmission loss of the acoustic metamaterial is carried out.

As described in [2], in this work will be considered the concept of *heterogeneous metamaterial*, that is a system composed of multiple small masses embedded within a passive poro - elastic matrix material. These masses create an array of resonant mass - spring -damper systems meanwhile the poro - elastic material (in this case the Melamine foam) remains ineffective.

These kind of metamaterials are usually used to control lower frequency sound radiation, increasing transmission lost if connected to structures subject to vibrations.

These materials shows a significant reduction of interior noise with only a slightly increase in the overall mass of the structure. It is possible to demonstrate that heterogeneous metamaterials can be used as lightweight blanket treatments for effectively controlling low frequency sound radiating from structures.

In figure 1.3 is graphically described what said in this paragraph.

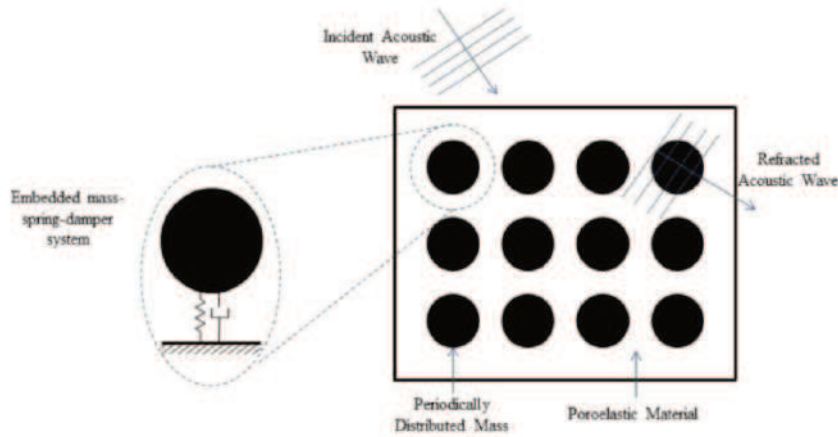


Figure 1.3: Heterogeneous metamaterial panel with a focus in the meaning of mass - spring - damper system [2].

Melamine foam is the poro - elastic material elided for the frame because it is characterized by lightness, sound absorption and fire-repellant properties.

Aluminium has been considered for the inclusions thanks to its good stiffness and mismatch with the density of the foam.

By increasing the number of the Aluminum cylinders, one can increase the damping properties of the melamine in the low-frequency range (approximately  $0 - 500\text{ Hz}$ ) avoiding the increase of the thickness of the materials and using as little weight as possible.

Actually, melamine should be modelled as viscoelastic material and their properties should be defined frequency - dependent. Unfortunately, for time reasons, in this work the complex solver has not been implemented in the *MUL*<sup>2</sup> micromechanics code.

For instance, if one consider the Young modulus of Melamine, it can be noticed that it has a real and a complex part. The majority of the properties of viscoelastic material is described through a real and an imaginary part.

As described in chapter 5, it is possible to consider only the real part of these properties for the bandgap analysis, because it has been demonstrated that the position of the bandgap does not change by varying the viscoelastic coefficient [11].

### 1.3.2 Overview of CASTLE Project

The CASTLE project is involved in the so called Marie Skłodowska-Curie actions.

The Marie Skłodowska-Curie actions are a set of major mobility research grants created by the European Union/European Commission to support research in the European Research Area (ERA) supporting researchers at all stages of their careers, regardless of age and nationality [16].

Researchers working across all disciplines are eligible for funding. The MSCA also support cooperation between industry and academia and innovative training to enhance employability and career development.

The main aim of the CASTLE project could be summarized by the following description, easily found in the European Union site: "By 2020 the increasing demand for biomass as a feedstock for fuel, fibre and food will have measurable economic, environmental and social effects.

The forest-based sector is responding to the competition for biomass with innovative products, such as renewable chemicals produced in biorefineries.

The agricultural sector is also reinforcing innovations based on fast growing biomass crops. Such innovations may bear completely new bio-based production systems, the long-term impact of which on environment, economic viability and social cohesion is difficult to foresee.

Policy makers, business and civil society organisations urge to safeguard the sustainability of new production systems. Hence, sustainability assessment methods that quantify environmental, economic and social impacts are needed for the bio-based economy.

However, so far academic training insufficiently reflects the relevance of sustainability impact assessment in business and policy making. "Careers in Sustainability Excellence" (CASTLE) closes this gap as it combines scientific innovative problem-oriented research and practical training of young academics on methods used for sustainability impact assessments in the bio-energy and forest-based sector in Europe. CASTLE educates sustainability experts for the broader bio-based economy.

The scientific program of CASTLE refines and improves state-of-the art sustainability assessment methods and applies them to current sustainability challenges in industry and policy making. With its training program CASTLE imparts a wide range of methods and skills. It covers, among other topics, assessments of direct environmental, economic and social sustainability impacts like GHG-emissions, carbon footprint, structures beneficial for biological diversity, water consumption and pollution, land use, value added."

A CASTLE subproject is regarding acoustic metamaterials for aeronautical applications. All the details and the results are reported in chapter 5 of this report, where the case originally proposed by the CASTLE project is taken into account.



# Chapter 2

## Theory

### 2.1 Carrera Unified Formulation

#### 2.1.1 Introduction

*Carrera Unified Formulation* (CUF) [3] is a class of theories of structure on which Finite Elements are formulated.

The CUF provides 1D (beam) and 2D (plate and shell) theories that go beyond classical theories, by exploiting condensed notation and by expressing the displacement fields over the cross-section (beam case) and along the thickness (plate and shell cases) in terms of base functions whose forms and orders are arbitrary. The condensed notation leads to the so-called *fundamental nucleus* (FN) of all the FEM matrices and vectors involved.

The FNs consist of a few mathematical statements whose forms are independent of the theory of structures employed. The FNs stem from the 3D elasticity equations via the principle of virtual displacements and can be easily obtained for all the dimensional cases.

The 1D and 2D FEs that stem from the CUF have enhanced capabilities since they can obtain results that are usually only provided by 3D elements with much lower computational costs.

#### 2.1.2 The Finite Element Method (FEM)

##### General Concept

The *Finite Element Method* was developed when the advances in technology and mathematics became relevant, namely with the advent of computers and the possibility to solve complex differential equations in "weak forms". The main concept of this computational method relies into few passages:

- The general problem is discretized into a number of finite domains called *elements*;
- Mathematical tools work properly on each domain;
- The problem is assembled and solved with the help of a computer.

The elements (or domains) can have several geometries, or may be one, two or at least three-dimensional. Moreover, it is worth to cite the important rule of boundary conditions (BCs) that can be geometric or mechanical.

Focusing into mathematical aspect, solving a structural problem means to find a solution to a given set of governing equations, which are defined in one of the three dimensional domain cases:

$$O(\Phi) = \Xi \quad (2.1)$$

where  $O$  can be a differential, integral and algebraic operator or a combination of these, whereas  $\Phi$  represents the unknown functions. As said before, the Finite Element Method solves this set of equations at the element level, for the sake of precision, in weak form. As far as the unknown functions are concerned, it is assumed to be a combination of a finite number of equations  $\Phi$  in a determined set of points called the *nodes* of the element. For instance, if the three-dimensional case is taken into account, the nodes-referred equation can be written as:

$$\Phi(x,y,z) = N_i(x,y,z)\Phi_i \quad (2.2)$$

Then, the *Weight Residual Method* (WRM) is applied for the governing equations, obtaining a system of algebraic equations for each element  $E$ :

$$\mathbf{K}_E \mathbf{U}_E = \mathbf{P}_E \quad (2.3)$$

The equation 2.3 is referred to the results of the mathematical problem. Subsequently, the whole structure governing equation is assembled by imposing compatibility/equilibrium conditions on the  $\Phi$  values at the nodes:

$$\mathbf{K}_S \mathbf{U}_S = \mathbf{P}_S \quad (2.4)$$

Differently from equation 2.3, equation 2.4 needs an automatic calculator for computation.

### Definition of the Stiffness Matrix for a two nodes bar

Taking the simplest example of a bar, it is now fundamental to introduce the  $\mathbf{K}$  stiffness bar. As far as its derivation is concerned, it may be performed by following two ways such as the classic equilibrium of the forces and the Principle of virtual work. Particularly in static and dynamic cases and with linear and non linear problems, applying the principle of virtual displacement is the best choice. Now, focusing on the bar, this will be the finite element under investigation. Nodes of the element are located at the ends of the bar with coordinates  $y = 0$  and  $y = L$ . For the notation, attention should be drawn to figure 2.1.



Figure 2.1: Local reference system and node numeration of a bar [3]

Taking into account equation 2.2:

$$u_y(y) = N_1(y)u_{y1} + N_2(y)u_{y2} \quad (2.5)$$

where  $u_1$  and  $u_2$  are the values of the displacement at the nodes 1 and 2 respectively and  $N_1(y)$  and  $N_2(y)$  are two linear Lagrange polynomials known as *shape functions* in the Finite Element context that are graphically represented in 2.2:

$$N_1(y) = 1 - \frac{y}{L}, \quad N_2(y) = \frac{y}{L} \quad (2.6)$$

which have to satisfy the conditions:

$$y = 0 \rightarrow u_y = u_{y1}, \quad y = L \rightarrow u_y = u_{y2} \quad (2.7)$$

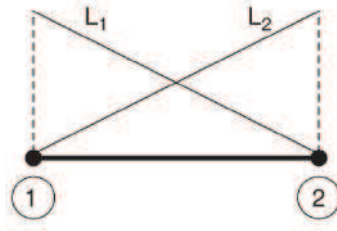


Figure 2.2: Example of linear shape function in a two nodes bar element [3]

Introducing principle of virtual displacement, for the sake of convenience, equation of displacement 2.5 is rewritten:

$$u_y(y) = N_1(y)u_{y1} + N_2(y)u_{y2} = \mathbf{N}\mathbf{U} \quad (2.8)$$

where obviously

$$\mathbf{N} = [N_1, N_2] \quad (2.9)$$

is the matrix of shape functions and

$$\mathbf{U}^T = (u_{y1}, u_{y2}) \quad (2.10)$$

is the vector of the unknown displacements.

As in 2.7, one has to derive the shape functions taking into consideration the condition aforementioned:

$$u_y(y = 0) = u_{y1}, \quad u_y(y = L) = u_{y2} \quad (2.11)$$

that obviously mean

$$N_1(y = 0) = 1, \quad N_1(y = L) = 0 \quad N_2(y = 0) = 0 \quad N_2(y = L) = 1 \quad (2.12)$$

Because of linear Lagrange polynomial are used, Thales theorem can be applied to find an expression for shape function, leading to the same expression of equation 2.6. Complete mathematical passages can be found directly on [3]. Differential operator of the strain -displacements relations  $\mathbf{b}$  is now introduced in order to express the displacement  $u_y$  in terms of nodal displacements. Attention should be payed on the new formulation of axial strain:

$$\epsilon_{yy} = \frac{du_y}{dy} = u_{y,y} = \mathbf{b}u_y = \mathbf{b}\mathbf{N}\mathbf{U} = \mathbf{B}\mathbf{U} \quad (2.13)$$

where  $\mathbf{B}$  is a matrix composed as:

$$\mathbf{B} = \mathbf{bN} \quad (2.14)$$

For the sake of brevity, explicit form of 2.13 is not reported here. In the static case, the principle of virtual displacements states that

$$\delta L_{int} = \delta L_{ext} \quad (2.15)$$

where  $\delta L_{int}$  and  $\delta L_{ext}$  are respectively the variation of the work done by internal and external forces that can be expressed as:

$$\delta L_{int} = \int_V \delta \epsilon_{yy} \sigma_{yy} dV = \delta \mathbf{U}^T \mathbf{K} \mathbf{U} \quad (2.16)$$

$$\delta L_{ext} = \delta u_{y1} P_{y1} + \delta u_{y2} P_{y2} = \delta \mathbf{U}^T \mathbf{P} \quad (2.17)$$

applying equation 2.15:

$$\delta \mathbf{U}^T \mathbf{K} \mathbf{U} = \delta \mathbf{U}^T \mathbf{P} \quad (2.18)$$

In order to provide another useful expression of  $\mathbf{K}$ , it is worth to remember Hooke's law:

$$\sigma = E \epsilon \quad (2.19)$$

the variation of work due to the internal forces can be reformulated as:

$$\delta L_{int} = \int_V \delta \epsilon_{yy}^T E \epsilon_{yy} dV \quad (2.20)$$

taking into account axial strain new notation expressed in equation 2.13, its variation turns on:

$$\delta \epsilon_{yy}^T = \delta \mathbf{U}^T \mathbf{B} \quad (2.21)$$

Substituting equations 2.21 2.13 and into 2.20 it yields

$$\delta L_{int} = \int_V \delta \mathbf{U}^T \mathbf{B}^T E \mathbf{B} \mathbf{U} dV \quad (2.22)$$

but  $\mathbf{U}$  and  $\delta \mathbf{U}$  are constant coefficient that can be taken out of the integral:

$$\delta L_{int} = \delta \mathbf{U}^T \left( \int_V \mathbf{B}^T E \mathbf{B} dV \right) \mathbf{U} \quad (2.23)$$

Finally, the stiffness matrix can be written as:

$$\mathbf{K} = \int_V \mathbf{B}^T E \mathbf{B} dV \quad (2.24)$$

and consequently

$$\delta L_{int} = \delta \mathbf{U}^T \mathbf{K} \mathbf{U} \quad (2.25)$$

Referring to an element with constant cross section it is possible to write the stiffness matrix of the element in the form:



$$\mathbf{K} = \frac{EA}{L} \begin{bmatrix} 1 & -1 \\ -1 & 1 \end{bmatrix} \quad (2.26)$$

Stiffness matrix is symmetric, singular and positive definite. Commonly, stiffness matrices of linear elastic problems are positive definite. The equilibrium equation of a single bar can therefore be written as:

$$\mathbf{K} \mathbf{U} = \mathbf{P} \quad (2.27)$$

### 2.1.3 Fundamental Nuclei Definition

The main novelty of CUF approach certainly is the Fundamental Nuclei definition (FN) through which it is possible to derive Finite Elements matrices and vectors. It is necessary to extend the index notation to the theory of structures, obtaining a 3D-square array unchanged for 1D, 2D or 3D cases, characterised by four indexes  $(i, j, \tau, s)$ . In order to proof the useful property of FE matrix/vector derivation, it has been presented the procedure to compute the stiffness matrix of the two nodes bar already calculated in the previous paragraph basing on traditional approach (eq. 2.35).

#### Definition of the Stiffness Matrix for a two nodes bar with FN approach

A compact index approach has been used, then is worth to distinguish the displacements (denoted by  $i$ ) from their virtual variations (denoted by  $j$ ):

$$u_y(y) = N_i(y)u_{y_i} \quad (2.28)$$

$$\delta u_y(y) = N_j(y)u_{y_j} \quad (2.29)$$

Starting from the latter equations strains and strain variations are expressed as:

$$\epsilon = N_{i,y}u_{y_i} \quad (2.30)$$

$$\delta u_y(y) = N_{j,y}u_{y_j} \quad (2.31)$$

where it is known that

$$N_{i,y} = \frac{dN}{dy} \quad (2.32)$$

In order to understand the real meaning of the FN it is needed to recall the expression of the virtual variation of internal work:

$$\delta L_{int} = \int_V \delta \epsilon^T E \epsilon dV = \delta u_{y_j} \left( \int_V N_{j,y} E N_{i,y} dV \right) u_{y_i} = \delta u_{y_j} k^{ij} u_{y_i} \quad (2.33)$$

where  $k^{ij}$  is the so called *fundamental nucleus* of a bar:

$$k^{ij} = \int_V N_{j,y} E N_{i,y} dV \quad (2.34)$$

Two properties can be particularly appreciated namely the invariance with respect the number of nodes of the element and to the choice of the shape function.

Calculating all the Fundamental Nuclei it is possible to derive the stiffness matrix of the bar as in the previous paragraph:

$$\mathbf{K} = \begin{bmatrix} k^{11} & k^{12} \\ k^{21} & k^{22} \end{bmatrix} = \frac{EA}{L} \begin{bmatrix} 1 & -1 \\ -1 & 1 \end{bmatrix} \quad (2.35)$$

Obviously, FN approach can be extended even to a bar with several internal nodes (example of calculation can be found in [3]).

#### 2.1.4 Matrices Assembly

One of the advantages of CUF is that the assembly of the matrices can be easily implemented in a code. Basically, this process is characterised by four loops on the indexes already mentioned ( $i, j, \tau, s$ ) and for each index combination a FN is computed. In picture 2.3 is shown how the building of the matrix is performed, respectively for a node, for an element and finally the global matrix for the structure. The core is the FN, the loops on  $\tau$  and  $s$  give the node matrix, consequently, the loops on  $i$  and  $j$  give the element matrix and then the final loop on the elements builds the global stiffness matrix.

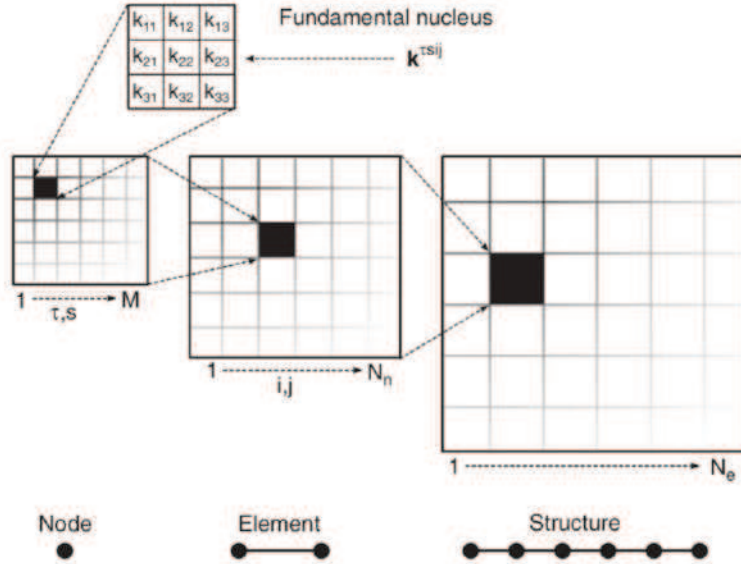


Figure 2.3: Matrices assembly process [3]

#### 2.1.5 An Unique Approach

The CUF formulation, based on the indexes already mentioned, can be extended to any structural theory (plates and shell model). In figure 2.4 are shown the FEM models for the sake of comparison.

Combining Finite Element Method with the approximation of the theory of structures, formulations in table 2.1 are obtained.

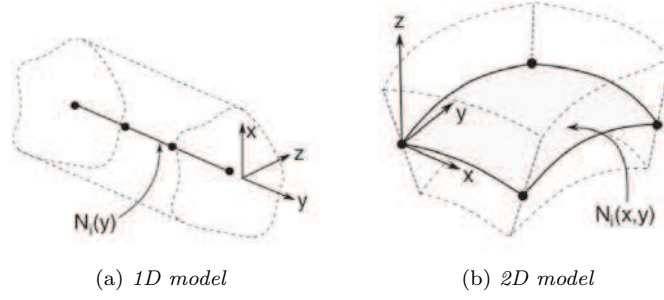


Figure 2.4: Example of FEM models [3]

1D	$\mathbf{u}(x, y, z) = N_i(y)F_\tau(x, z)$
2D	$\mathbf{u}(x, y, z) = N_i(x, y)F_\tau(z)$
3D	$\mathbf{u}(x, y, z) = N_i(x, y, z)$

Table 2.1: CUF formulation for the three dimensions

Where  $N_i$  are the shape functions and  $F_{tau}$  are called *expansions*. Focus on the latter, it could be noticed the way it is defined for the three dimensions:

Figures 2.5 are helpful to better understand expansion  $F_\tau$  meaning. Taking into account the 1D approach,  $F_\tau(x, z)$  approximates the displacements of the cross section, meanwhile the Finite Element model can be used to define the problem along the y-axis. As far as the 2D approach is concerned,  $F_\tau(z)$  expresses displacements along the thickness of the shell/plate element, instead Finite Elements are used to describe the problem on the surface.

### 2.1.6 Resume

At the end of this section it could be useful to provide a CUF resuming table (2.6) directly taken from the book of Professor Carrera repeatedly quoted in this paragraph [3].

1D	$F_\tau(x, z)$
2D	$F_\tau(z)$
3D	1

Table 2.2: Expansions for the three dimensions

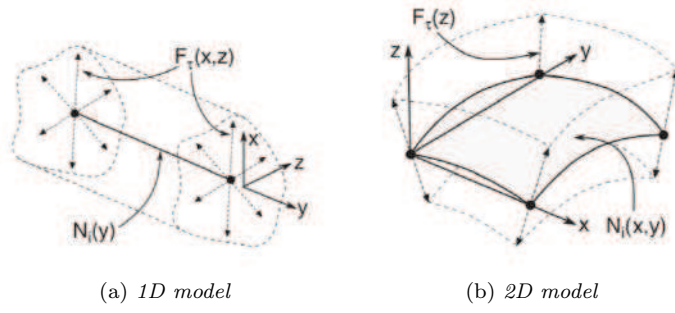
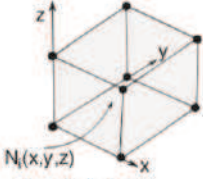
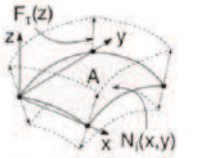
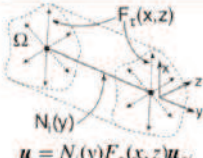
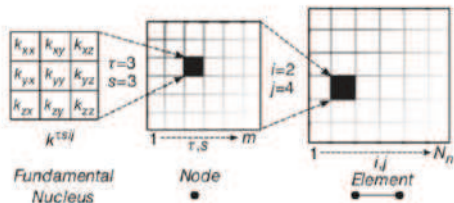


Figure 2.5: Approaches for the three dimensions [3]

Equilibrium equations in Strong Form $\rightarrow \delta L_i = \int_V \delta u k u dV + \int_S \dots dS$	
$\begin{bmatrix} k_{xx} & k_{xy} & k_{xz} \\ k_{yx} & k_{yy} & k_{yz} \\ k_{zx} & k_{zy} & k_{zz} \end{bmatrix} \begin{Bmatrix} u_x \\ u_y \\ u_z \end{Bmatrix} = \begin{Bmatrix} p_x \\ p_y \\ p_z \end{Bmatrix}$	$\begin{aligned} k_{xx} &= -(\lambda + 2G) \partial_{xx} - G \partial_{zz} - G \partial_{yy}; \\ k_{xy} &= -\lambda \partial_{xy} - G \partial_{yx}; \\ k_{xz} &= \dots \end{aligned}$
$\lambda = (Ev)/[1 + \nu](1 - 2\nu); \quad G = E/[2(1 + \nu)]$	
$u = u(x, y, z)$ $\delta u = \delta u(x, y, z)$	The diagonal (e.g. $k_{xx}$ ) and the non-diagonal (e.g. $k_{xy}$ ) terms can be obtained through proper index permutations.
 $u = N_i(x, y, z) u_i$ $\delta u = N_j(x, y, z) \delta u_j$	<b>3D FEM Formulation</b> $\rightarrow \delta L_i = \delta u k^{ij} u_j$ $k_{xx}^{ij} = (\lambda + 2G) \int_V N_{i,x} N_{j,x} dV + G \int_V N_{i,z} N_{j,z} dV + G \int_V N_{i,y} N_{j,y} dV;$ $k_{xy}^{ij} = \lambda \int_V N_{i,y} N_{j,x} dV + G \int_V N_{i,x} N_{j,y} dV$
 $u = N_i(x, y) F_\tau(z) u_{\tau i}$ $\delta u = N_j(x, y) F_s(z) \delta u_{sj}$	<b>2D FEM Formulation</b> $\rightarrow \delta L_i = \delta u_{sj} k^{\tau s ij} u_{\tau i}$ $k_{xx}^{\tau s ij} = (\lambda + 2G) \int_\Omega N_{i,x} N_{j,x} d\Omega \int_h F_\tau F_s dz$ $+ G \int_\Omega N_i N_j d\Omega \int_h F_{\tau,z} F_{s,z} dz + G \int_\Omega N_{i,y} N_{j,y} d\Omega \int_h F_\tau F_s dz;$ $k_{xy}^{\tau s ij} = \lambda \int_\Omega N_{i,y} N_{j,x} d\Omega \int_h F_\tau F_s dz + G \int_\Omega N_{i,x} N_{j,y} d\Omega \int_h F_\tau F_s dz$
 $u = N_i(y) F_\tau(x, z) u_{\tau i}$ $\delta u = N_j(y) F_s(x, z) \delta u_{sj}$	<b>1D FEM Formulation</b> $\rightarrow \delta L_i = \delta u_{sj} k^{\tau s ij} u_{\tau i}$ $k_{xx}^{\tau s ij} = (\lambda + 2G) \int_l N_i N_j dy \int_A F_{\tau,x} F_{s,x} dA$ $+ G \int_l N_i N_j dy \int_A F_{\tau,z} F_{s,z} dA + G \int_l N_{i,y} N_{j,y} dy \int_A F_\tau F_s dA;$ $k_{xy}^{\tau s ij} = \lambda \int_l N_{i,y} N_{j,x} dy \int_A F_\tau F_{s,x} dA + G \int_l N_i N_{j,y} dy \int_A F_{\tau,x} F_s dA$
CUF leads to the automatic implementation of any theory of structures through 4 loops (i.e. 4 indexes):	
<ul style="list-style-type: none"> <li>• <math>\tau</math> and <math>s</math> deal with the functions that approximate the displacement field and its virtual variation along the plate/shell thickness (<math>F_\tau(z), F_s(z)</math>) or over the beam cross-section (<math>F_\tau(x, z), F_s(x, z)</math>);</li> <li>• <math>i</math> and <math>j</math> deal with the shape functions of the FE model, (3D: <math>N_i(x, y, z), N_j(x, y, z)</math>; 2D: <math>N_i(x, y), N_j(x, y)</math>; 1D: <math>N_i(y), N_j(y)</math>).</li> </ul>	
	

This Table shows the essential features of the CUF. The strong form of the equilibrium equations allows one to derive a compact formulation for the fundamental nucleus. The nine elements of the FN can be written using only 2 terms. In this table,  $k_{xx}$  and  $k_{xy}$  are reported. All the remaining terms can be derived by a permutation of the indexes. This compact formulation is used to derive the 3D, 2D and 1D models in weak form

Figure 2.6: CUF resuming table [3]

## 2.2 Introduction to Micromechanics

### 2.2.1 Introduction

Reached that point, it is necessary to focus on the problems could arise dealing with metamaterials. This matter is postponed to a specific section where it will be treated with good care, but for now, basically it is sufficient to consider a metamaterial simply as composite material, neglecting all its relevant properties.

It is known that the main difference between composite materials and common materials like metals, is substantially that they cannot be considered easily isotropic and homogeneous, being usually anisotropic and heterogeneous. While anisotropy can be faced with a coordinate transformation, dealing with heterogeneity could be harder from the computational cost point of view, because using direct numerical simulations requires an extremely fine scale Finite Element mesh with enormous numbers of degrees of freedom.

In response to that issue composite material can be replaced with an *effective* homogeneous material which is imaginary and this procedure is called *homogenization*.

Through a micromechanics model it is possible to find out the effective properties of the substitutive equivalent material. So, one could state that the main goal of micromechanics is to replace a heterogeneous material with an imaginary homogeneous one so that the analysis of the original structure made of heterogeneous materials can be simplified and consequently to predict the effective macroscopic properties of heterogeneous materials in terms of microstructure [4]. The second purpose of micromechanics is to predict the *local fields* (stress and strain fields into the microstructure). This procedure is called *dehomogenization* and it is a very relevant for the evaluation of strength and failure of heterogeneous materials.

### 2.2.2 Main Definitions

Micromechanics modelling cannot be carry out with the help of microscopic analysis, because the complexity of the problem cannot be handly using this technique.

Yu defines an heterogeneous material representation as "*a point in our macroscopic structural analysis, the size of that material point is irrelevant and it could contain one or many fundamental building blocks of the material, if such fundamental building blocks can be identified*",[4].

According to Yu, the first step to be faced is to find out a microstructure representative of the material. The choice of this microstructure depends on the kind of the analysis that one want to carry out and on the micromechanics model chosen. There are four methods to model a right microstructure:

- Idealizing the previously observed microscopical features of the material with simple geometrical models;
- Reconstructing the microstructure starting from statistical information;
- Reconstructing the microstructure starting from images from X-ray microtomography;
- Predicting the microstructure from simulating the manufactory process.

In order to comply with the need to find an analysis domain that is representative of the heterogeneous material microstructure, the *Representative Volume Element* (RVE) is defined. It must contain a sufficient amount of heterogeneities for the effective properties regardless of boundary conditions and it must be tiny enough to be considered as a material point for the macroscopic structural analysis. There are a lot of definitions of RVE, but most of them are a

posteriori and focus on play down statistical scattering of the effective properties, which are known only after the RVE has been chosen and the micromechanics analysis has been carried out.

If one assumes that the material is characterised by periodic heterogeneities it is possible to interchange the RVE concept with the *Unit Cell* (UC) concept.

According to Yu [4], UC is referred to the fundamental building block of the material, and it can be defined as a repeating unit cell in the case of materials featuring periodic heterogeneities.

However UC should correspond to the smallest building block of the heterogeneous material, whilst RVE can include multiple UCs. Both UCs and RVE are not unique in the material, this fact is easily demonstrated looking at figure 2.7.

Naturally, if an ideal case is taken into account, one must be able to obtain the same effective properties despite the choices of UCs, contrariwise, in a real case only a good micromechanics theory can provide similar values of effective properties.

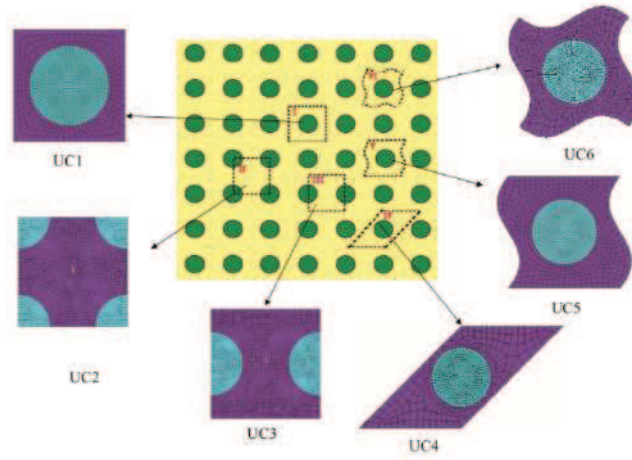


Figure 2.7: Different UCs choices [4]

### 2.2.3 Mechanics of Structure Genome

Mechanics of structure genome is defined as *The smallest mathematical building block of the structure*. The term *Genome* is used to highlight that MSG actually contains all the constitutive information required for the description of a structure as a genome contains all the information needed for the development of an organism.

Basically, MSG is used to face the problem related to the loss of the information. That issue arises when the passage from heterogeneous body to equivalent homogeneous one happens.

MSG is an unified approach used for multiscale analysis of composite structures [4]. Structure Genome for 3D bodies has a similar role to Unit Cell or RVE, but its meaning changes.

Considering figure 2.8, if the binary composed structure is taken into account (1D heterogeneity case), the Structure Genome will be a line composed by two straight segments representing the different phases. For a composite structure presenting 2D heterogeneity, Structure genome will be described by two dimensions.

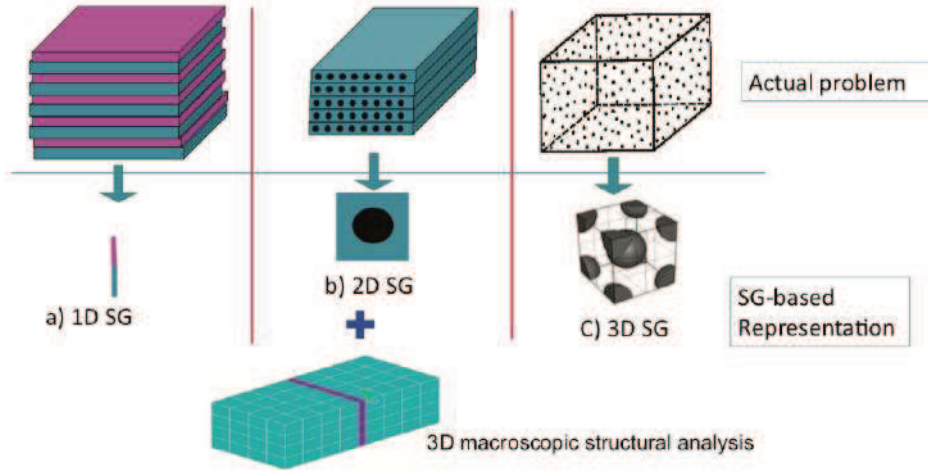


Figure 2.8: Structure Genome creation for a 3D structure [4]

## 2.3 Metamaterials

### 2.3.1 Introduction

The term *Metamaterial* has been introduced by R.M. Walser [17] in 2000, so it is almost 19 years old.

A common definition, provided by several authors, characterizes them as heterogeneous "artificial" materials, that show particular, unusual responses to different physical excitations or constraints. It is possible to distinguish between acoustic, electromagnetic, optical and other classes of metamaterials. Each of them is able to manifest peculiar behavior when related with waves which origin can be elastic (mechanical) or electromagnetic.

Historically, metamaterial were first considered from the idea of simultaneously negative dielectric constant and magnetic permeability for electromagnetic waves. Later on, Pendry et al. presented the first man made structure to achieve negative permeability and also showed that the negative refractive could be fulfilled by aperiodic structure.

The ideas of creating acoustic metamaterials, follows those of electromagnetic ones thanks to concept analogy [18].

### 2.3.2 Acoustic Metamaterials and Phononic Crystals

Phononic crystals are different from acoustic metamaterials and differences between them are absolutely needed to understand the two different band gap phenomena: Bragg scattering and local resonance.

#### Phononic Crystals

As said in the previous paragraphs, if a certain frequency range is considered, it is possible to obtain the complete sound attenuation basically relying on the concept of "classical wave spectral gap" that it was originally concerned for electromagnetic waves, and subsequently extended to



elastic waves.

Starting from [19], it is possible to create spectral gaps that forbids wave propagation by means of strong periodic modulation in density and/or sound velocity.

Problems arise when one recognise that these spatial modulations must be of the same order as the wavelength in the gap. For the sake of understanding, for sound waves in air, the speed of sound is 343 m/s (at room temperature and atmospheric pressure). Using the simple relation 2.36, wavelengths of sound frequencies audible to the human ear (20 Hz - 20 kHz) are thus between approximately 17 m and 17 mm, respectively [20]. Then, one can notice that, in order to shield a normal acoustic sound, it would be required a structure with dimensions comprised between 17 mm and 17m, and it would be too complicate to realize.

Briefly, a phononic crystal is a periodic structure (elastic/density contrast) based on the Bragg mechanism which means that the created band gap is due to the periodicity effect induced by destructive interferences.

So the band gap is opened at a frequency directly related to the periodicity, but they are limited in the low-frequency ranges because, as seen before referring to 2.36, their unit cell size scales with wavelength.

$$\lambda f = c \rightarrow f = \frac{c}{\lambda} \quad (2.36)$$

### Acoustic Metamaterials

The story is different for metamaterials. Indeed, a metamaterial is an artificial composite structure composed of inclusions called *resonators*, that can interact/couple with the hosting media in 1D, 2D or 3D case.

The created band gap in that case is a result of the coupling between the local resonance of the inclusions (resonators = spring - mass system for example) and the waves propagating in the hosting media.

Usually, the band gap is opened at much lower frequencies than the frequencies allowed by the Bragg mechanism in phononic crystals, so that it is associated at the so called *subwavelength regime*.

In fact, because the band gap is opened at very low frequencies, the associated wavelengths are then very large.

In comparison to phononic crystals, the dimensions of the resonators are usually extremely smaller, namely subwavelength resonators. The metamaterial can then be considered as a homogenous material or a continuum (the inclusions are so small in comparison with the involved wavelengths) having homogeneous properties, called effective properties, that can be, under some specific conditions, negative.

Acoustic metamaterials show peculiar acoustic characteristics that materials in nature are not able to possess such as negative effective mass density and negative effective modulus. These unique aspects make these material really useful for different applications as acoustic or elastic filters, acoustic mirrors and sound insulators [12] [21].

As Chen describes [22], the usual composition of acoustic metamaterial is characterized by a series of unit cells that are periodically arranged and the single unit cell consists in a resonance unit.

As far as the phononic crystal problem is concerned, thanks to acoustic metamaterials design there are several solutions trying to comply with it, for instance those proposed by [19] and [23]. In particular, the latter explains how architected 3D- printed material can be used to control elastic/acoustic wide ranges due to the fact that, in the linear regime, the more the size of the geometrical feature is decreased, the more the operational frequency is increased.

According to [18], the very first approach utilized composite materials composed of lead balls,

epoxy and rubber [19], as said before, negative density can be induced by the local-resonance of this structure. Since that, other acoustic metamaterials have emerged in this area.

### 2.3.3 Origin of Negative Density in Acoustic Metamaterials

In this paragraph have been reported some information about Lee et al. work [5], and its aim is to provide a brief and simple introduction to the non - intuitive concept of *negative density*, and so deeply focusing on the phenomenon of the *local resonance* in acoustic metamaterials.

Lee introduces the terminology of *hidden force* and *hidden source of volume* specifying that: "*the effective density or modulus is negative when the hidden force or source of volume is larger than, and operates in antiphase to, respectively, the force or volume change that would be obtained in their absence*".

- *hidden force*, resulting in an effective mass or density, involves local, time-dependent non - apparent forces that provide a net force on the unit cell of the acoustic metamaterial.
- *hidden source of volume*, resulting in an effective elastic modulus, involves time - dependent hidden-source of volume or displacement that only produces pairs of force acting equally and oppositely on either side of the unit cell.

#### Hidden Forces definition

It is worth to introduce the precise meaning of *hidden forces* in order to better understanding the *effective mass* concept in system that contain non - apparent mechanical elements.

With the aim to derive the first important definition of effective mass, the author consider a first example when a wheel of mass M, radius R and moment of inertia I rolling in the x direction without slipping on a flat, horizontal surface, as shown in the figure 2.9.

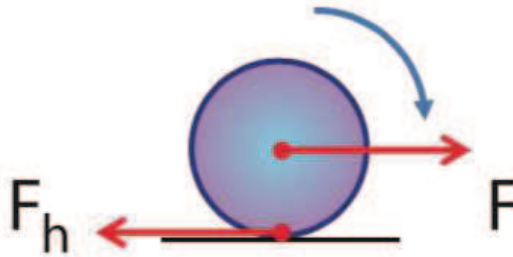


Figure 2.9: Hidden and external forces for the case of a rolling wheel [5]

If one applies Newton's laws, it is possible to derive the acceleration:

$$\ddot{x} = \frac{F}{[M(1 + \frac{I}{MR^2})]} \quad (2.37)$$

where actually the denominator is the first definition of effective mass:

$$M_{eff} = \frac{F}{\ddot{x}} = [M(1 + \frac{I}{MR^2})] \quad (2.38)$$

In that case, the hidden force is connected with the frictional force on the wheel rim and for this reason  $\ddot{x} < \frac{F}{M}$ .

Defining the effective mass, it is possible to find the correct acceleration using a single equation. The concept rely on the fact that in general, if an external force is applied to a mass, a hidden force may also act on the mass with its direction assumed collinear with the direction of the external force. In that way it holds:

$$\ddot{x} = \frac{F + F_h}{M} \quad (2.39)$$

and then:

$$M_{eff} = \frac{M}{1 + \frac{F_h}{F}} \quad (2.40)$$

Then, the autor plots a graph reported in figure 2.10 in which one can notice that if  $F_h$  approaches  $-F$ ,  $M_{eff}$  infinity large and if  $F_h < -F$ ,  $M_{eff}$  becomes negative.

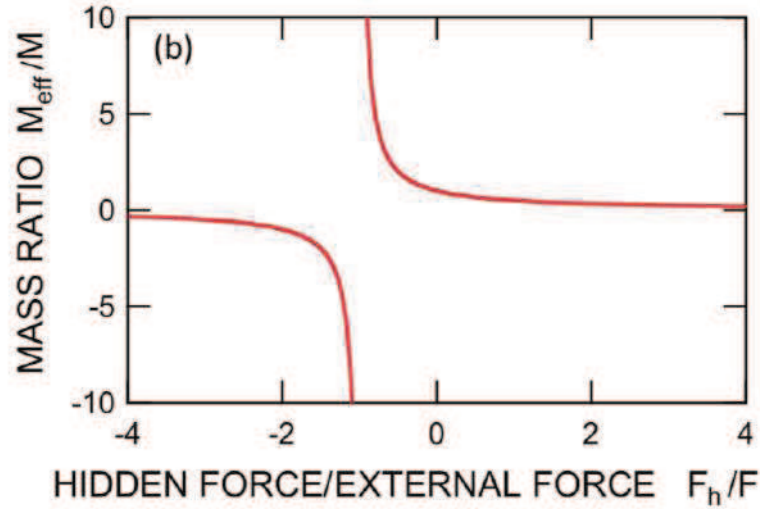


Figure 2.10: Normalized plot of the effective mass as a function of the hidden force [5]

As it is possible to see in figure 2.11, ignoring the presence of the spring and regarding the system as a free mass subject to hidden force  $F_h$ , one can demonstrate that this is a prototype of a system exhibiting negative mass  $M_{eff}$ .

In this case, hidden force has been defined as:

$$F_h = -kx \quad (2.41)$$

where  $k$  is the spring constant and  $x$  the displacement. Considering a sinusoidal external excitation as:

$$F = F_0 e^{-i\omega t} \quad (2.42)$$

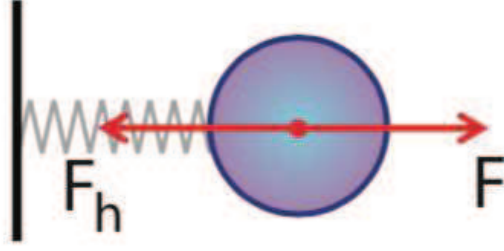


Figure 2.11: Hidden and external forces for the case of a simple harmonic oscillator [5]

it is possible to write the system equation of motion:

$$M\ddot{x} = F_0 e^{-i\omega t} + F_h \quad (2.43)$$

Considering the harmonic solution for the system equation of motion:

$$x = x_0 e^{-i\omega t} \quad (2.44)$$

and deriving twice is obtained:

$$\omega^2 M x e^{-i\omega t} = F_0 e^{-i\omega t} + F_h \quad (2.45)$$

From hidden force definition in eq. 2.46 it is known:

$$x = -\frac{F_h}{k} \quad (2.46)$$

and remembering the expression of natural frequency:

$$\omega_0 = \sqrt{\frac{k}{M}} \quad (2.47)$$

substituting eq. 2.46 and eq. 2.47 into the equation of motion of the system 2.45, one can give another expression for the hidden force:

$$F_h = -kx = -\frac{F\omega_0^2}{\omega_0^2 - \omega^2} \quad (2.48)$$

Finally, in order to achieve the expression of the effective mass for the harmonic system eq. 2.48 has to be substituted into eq. ?? obtaining:

$$M_{eff} = M \left( 1 - \frac{\omega_0^2}{\omega^2} \right) \quad (2.49)$$

Integrating the acceleration it is possible to obtain the displacement and to see that it oscillates near the resonance because  $M_{eff}$  becomes very small.

Another aspect interesting to considerate is the sudden shift of the phase of the displacement by

$\pi$  with respect the driving force as the frequency passes through the resonance. The meaning of this fact is simply found in eq. 2.49: when  $\omega = \omega_0$  the sign of  $M_{eff}$  changes.

As seen before, negative effective mass is a consequence of  $F_h < -F$  and it implies, when a sinusoidal excitation is taken into account, that the hidden force is not only in antiphase with but also has a magnitude that is larger than that of external force.

Approaching  $\omega = \infty$ , the effective mass tends to  $-\infty$  because  $F$  for a given oscillation amplitude becomes small with respect the oppositely directed spring force  $F_h$  to the real mass  $M$ .

Otherwise, if  $\omega$  is near to zero, the effective mass tends to  $M$  because  $F$  for a given oscillation becomes very large in comparison to  $F_h$ .

### Example of Acoustic Metamaterial negative density evaluation

In figure 2.12 it is possible to see a basically designed acoustic metamaterial really similar to the cases faced in this work.

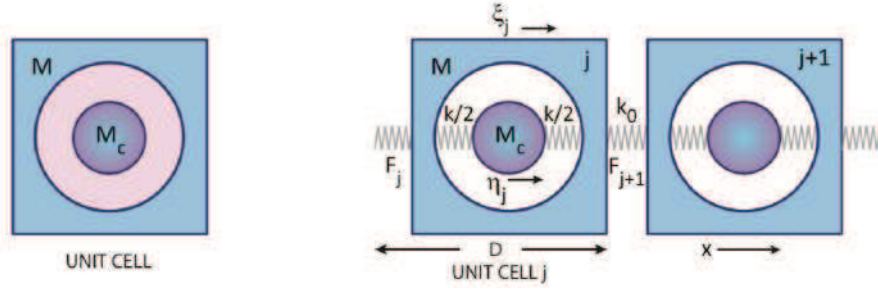


Figure 2.12: Unit cell and Acoustic Metamaterial sketch [5]

The aim of this paragraph is only to show, in figure 2.13 the relation between the effective density (based on the effective mass definition) as a function of the frequency, for the acoustic metamaterial taken into account.

### 2.3.4 Bragg Scattering

To understand how vibration propagates in a medium, more specifying, in a material, it is crucial to introduce the properties of waves and the equation related to them. then, it will be taken into account how to manipulate waves through *Bragg Scattering* and the use of *Local Resonance*. The equation that describe the travelling modulation can be written as:

$$f(x,t) = \cos(\omega t - kx + \phi) \quad (2.50)$$

Waves can interfere with each others in two absolute different ways that are shown in figure 2.14:

- on the left (a) destructive interference happens when the difference in phase of the two waves taken into account is of  $\Delta\phi = \pi$ , in this case is said that the waves are in antiphase;
- on the right (b) constructing interference happens when the difference in phase of the two waves taken into account is of  $\Delta\phi = 0$ , in this case is said that the two waves are in phase.

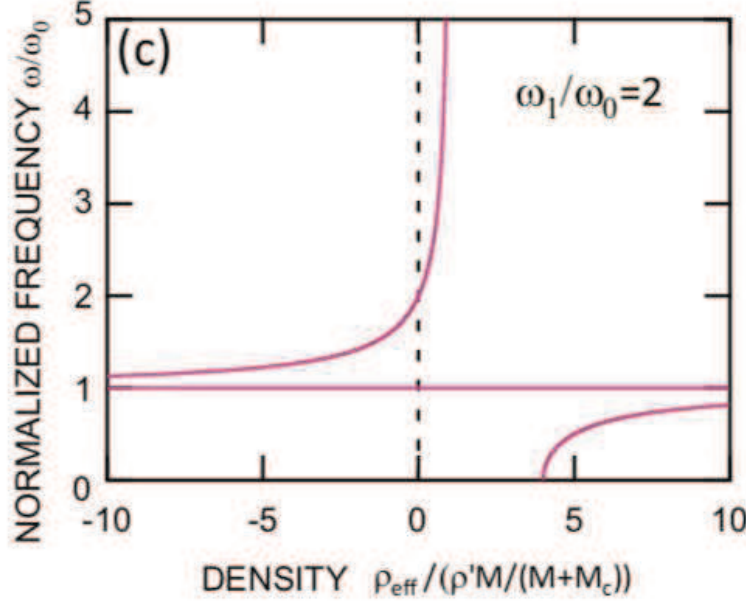


Figure 2.13: Normalized plot of the effective density as a function of frequency [5]



Figure 2.14: Types of interference [6]

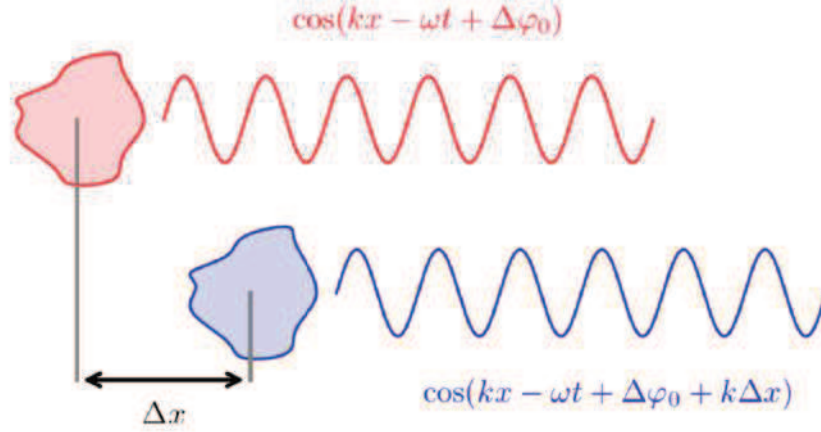
Now, taking into account a generic scatterer, it is obvious that when a generic wave excites it, the radiated outgoing waves will present changes in phase. Two generic scatterers are considered at a distance  $\Delta x$  as in figure 2.15. It is possible to notice from the equation in the figure that if  $k\Delta x = \pi$  the scatterers waves interfere destructively and if  $k\Delta x = \frac{\lambda}{2}$ , it leads to a strong destructive effect on the propagation of waves. This phenomenon is called *Bragg Scattering* and it occurs when one deal with periodic arrays of scatterers.

As said before, Bragg scattering is at the heart of phononic crystals and if a periodic array of scatterers of length  $\Delta L$  is used, one can imagine how much dramatic could be the effect on wave propagation if the Bragg Condition in eq. 2.51 is fulfilled.

$$\Delta L = \frac{\lambda}{2} \quad (2.51)$$

"If one wants to change the propagation of waves at a frequency  $\nu = \frac{\omega}{2\pi}$ , it has to design structures with dimension  $\Delta L \approx \frac{c}{\nu}$ " [6].

Finally, at the frequencies where the Bragg condition is met, a windows opens where no waves can propagate and it is called *band gap*. In figure 2.16 is shown the effect of the Bragg scattering

Figure 2.15: Two equal scatterers at a distance  $\Delta x$  [6]

on the dispersion relation of a phononic crystal.

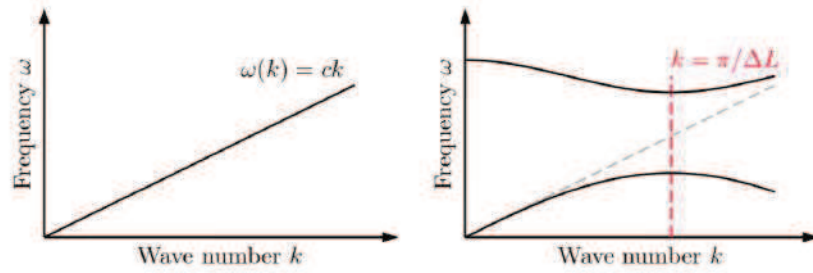


Figure 2.16: Band gap of a phononic crystal [6]

Now, it is simpler to understand the limitations of phononic crystals in cloaking of environmental acoustic sounds applications.

### 2.3.5 Local Resonances

In the previous chapter the mechanism at the base of Bragg Scattering has been explained, namely that periodic structures, under well defined conditions, can have an influence on the propagation of waves. It has been seen taken into account all the possible limitations imposed by the size of the structure, and for this reason, it is worth to introduce and understand the concept of *Local Resonance*. It is Bragg scattering similar effect, but in this case it is necessary to understand the coupling of two oscillators.

In order to explain that concept, Huber [6] consider two oscillators like those considered in figure 2.17 that are described by the equations:

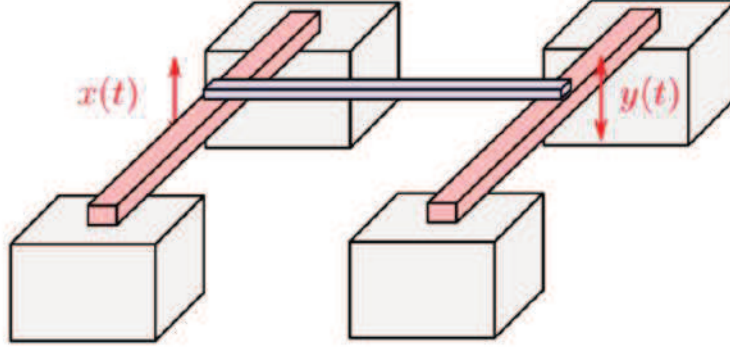


Figure 2.17: Two oscillators coupled [6]

$$\ddot{x}(t) = -\omega_0^2 x(t) + \gamma^2 y(t) \quad (2.52)$$

$$\ddot{y}(t) = -\omega_0^2 y(t) + \gamma^2 x(t) \quad (2.53)$$

The assumption that  $\gamma \ll \omega_0$  than  $\gamma = 0$  can be done, and knowing that the solutions of eq. 2.52 and 2.53 are:

$$x(t) = x_0 e^{i\omega_0 t} \quad (2.54)$$

$$y(t) = y_0 e^{i\omega_0 t} \quad (2.55)$$

If the two oscillators are coupled,  $\gamma \neq 0$ , and one has to find the combined solutions.

$$\begin{pmatrix} x(t) \\ y(t) \end{pmatrix} = \begin{pmatrix} x_0 \\ y_0 \end{pmatrix} e^{i\omega t} \rightarrow \quad (2.56)$$

$$-\omega^2 \begin{pmatrix} x_0 \\ y_0 \end{pmatrix} e^{i\omega t} = \begin{bmatrix} \omega_0^2 & \gamma^2 \\ \gamma^2 & -\omega_0^2 \end{bmatrix} \begin{pmatrix} x_0 \\ y_0 \end{pmatrix} \quad (2.57)$$

Obviously, this is an eigenvalue problem for  $\omega$  and consequently solving the characteristic equation:

$$\det \begin{bmatrix} \lambda - \omega_0^2 & \gamma^2 \\ \gamma^2 & \lambda - \omega_0^2 \end{bmatrix} = (\lambda - \omega^2)^2 - \gamma^4 = 0 \rightarrow \quad (2.58)$$

$$\lambda_{\pm} = \omega^2 \pm \gamma^2 \rightarrow \omega_{\pm} = \sqrt{\omega^2 \pm \gamma^2} \quad (2.59)$$

If the two oscillators are degenerate, namely they have the same frequency ( $\gamma = 0$ ), the coupling effect between them is strongest as illustrated in figure 2.18 (a).

The more  $\gamma$  increases, the more the main effect of this coefficient is accentuated: it splits the



frequency of the two-oscillator system.

But what happens onto the dispersion curves? In figure 2.18 (b) and (c), is possible to notice how the coupling splits the degenerate system of the wave and the local oscillator and this effect is stronger when the two waves cross.

As in the Bragg scattering effect, a window is opened where no waves propagate. The difference is that this time the frequency is not dictated by the spacing of the periodic array but by the frequency of the local oscillator. So, resuming:

*"It is possible to modify the propagation of wave in the vicinity of a frequency  $f$  by coupling the wave to a local resonance with frequency  $f_0 \approx f$ " [6].*

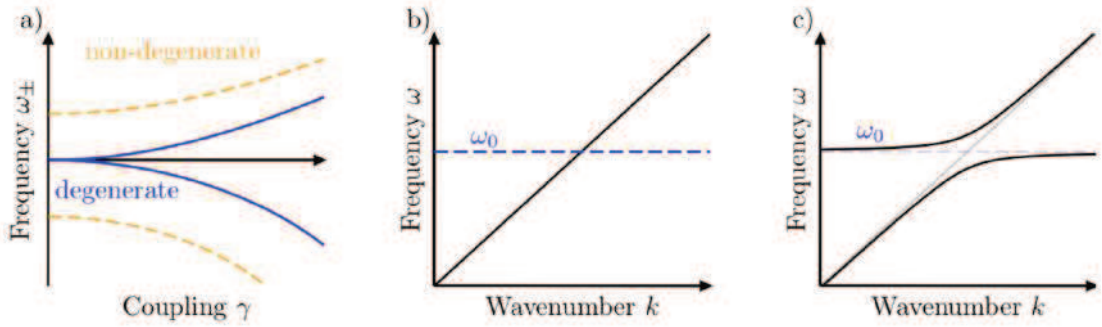


Figure 2.18: (a) Effect of the coupling  $\gamma$  on the eigenfrequency of the two oscillators. (b) Wave dispersion (black) and the location of a local resonance (blue). (c) Coupling the local resonance to the wave leads to the opening of a band gap at the frequency  $\omega_0$  of the local resonance [6]

### 2.3.6 Bragg Scattering vs Local Resonance

One can wonder, looking at the dispersion curves, how could be possible to recognize the a Bragg scattering bandgap instead of a Local Resonance one.

For a general rule, a Bragg scattering bandgap is recognizable by looking at the position of the maximum extreme points (lower and higher): If the maximum of the bandgap lower mode has the same abscissa value (reduced wave number) of the minimum of the bandgap higher mode, the bandgap turn out as a bragg scattering one. This effect is due to the periodicity of the phononic crystal, that, as explained before, induces destructive interferences causing a lack of wave propagation.

Otherwise, if the maximum of the lower bandgap mode is "shifted" with respect the minimum of the higher bandgap mode, it is possible to say that, in most cases, the bandgap will be locally resonant.

This rule is general, and sometimes it couldn't work. The only way to discover what is really happening into the bandgap is looking at the modes placed near the extremes of it. Firstly, is important to understand which are the extremes of the "longitudinal" bandgap and the "transversal" one. In other words, by analysing the characteristic mode motion, one can easily understand where the cloaking begins if considering the mode motion longitudinal to the wave propagation direction or considering the mode motion transversal to the wave propagation direction.

This process may be confirmed with comparing the consideration done with the longitudinally and transversally polarized transmission curves.

The original, total bandgap that one has to consider is the one that doesn't permit the wave propagation, in both the longitudinal and the transversal propagation motion.

## 2.4 Methods to Compute the Dispersion Relation for the Wave Propagation Characterization of a Periodic Medium

### 2.4.1 Introduction

This section aims to provide a mathematical description of the numerical method used to determine dispersion relations implemented in *MUL*<sup>2</sup> micromechanics code.

This section is fully explained with an eye for detail in the work of Paolo Celli [24]. Propagation of waves in a periodic medium could be expressed by several relations but the best way to characterize it is the dispersion relation, namely a relation between wave properties such as frequency and wave vector.

Dispersion relations are obtained by analyzing the behavior of a single Repetitive Volume Element (RVE), under proper periodic boundary conditions that account for the wave propagation behavior, from this fact one can notice its convenience concerning analysis computational cost.

As explained in the micromechanics chapter, periodic media are structures or materials consisting of the spatial repetition of a repetitive volume element (RVE), or unit cell (UC). Obtaining this "signature" of the periodic medium is fundamental because it allows to understand which frequencies are allowed to propagate and which ones are forbidden. Various techniques to obtain a dispersion relation are available in the literature, their common denominator being that they all leverage the Floquet-Bloch's principle. In other words, imposing Bloch's principle means to imposing periodic boundary conditions to the wave problem: the unknowns (displacement in the case subsequently proposed) at certain locations on the boundary of the RVE are related to the same unknowns at different locations of the boundary by means a complex exponential function of the components of the wave vector. Which boundaries of the RVE are related to which depends on the periodic arrangement of the RVE.

Due to these boundary conditions, the periodic medium has been considered having infinite dimensions: consequently, only structures in which the RVE is repeated "enough times" are precisely represented by these dispersion relations, even if they are theoretical. Most of the methods lies to the solution of an eigenvalue problem for the frequency as a function of the wavenumber or vice versa.

What makes the difference between methods is the way in which the governing equations are considered in order to obtain the eigenproblem.

### 2.4.2 Finite Element Method for 1D Problem

Always referring to the work of Paolo Celli, it is possible to briefly mathematically describe the procedure only mentioned in the introduction. The bar problem (1D) is taken into account for the sake of simplicity.

It is assumed that the mass and stiffness matrix of the element and the global ones for the bar problem have already been derived.

As known from the theory, mass and stiffness global matrix dimensions depend on how many elements have been chosen in order to describe the RVE problem.

The reduced eigenproblem formulated is explained in 2.60:

$$([\mathbf{W}]^H [\mathbf{K}] [\mathbf{W}] - \omega^2 [\mathbf{W}]^H [\mathbf{M}] [\mathbf{W}]) [u_r] = 0 \quad (2.60)$$

Where the <sup>H</sup> apex stays for Hermitian Transposition. The discretized RVE degrees of freedom are expressed in the vector 2.61:

$$[u] = [u_0, [u_i], u_L]^T \quad (2.61)$$

where:

- $u_0$  is the axial displacement at  $x = 0$ ;
- $u_L$  is the axial displacement at  $x = L$ .

These two axial displacements are related through the Bloch's relation expressed in equation 2.62

$$u_L = u_0 e^{-i\xi} \quad (2.62)$$

Where  $\xi$  is called adimensional wavenumber.

This relation justifies the expression of the reduced vector of degrees of freedom (2.64) that appears in the reduced eigenproblem:

$$[u_r] = [u_0, [u_i]]^T \quad (2.63)$$

So it is possible to say that  $[u]$  and  $[u_r]$  are related through:

$$[u] = [\mathbf{W}][u_r] \quad (2.64)$$

where  $[W]$  is defined in eq. 2.65:

$$[\mathbf{W}] = \begin{bmatrix} [I]_{1 \times 1} & [0]_{1 \times in} \\ [0]_{1 \times in} & [I]_{in \times in} \\ e^{-i\xi}[I]_{1 \times 1} & [0]_{1 \times in} \end{bmatrix} \quad (2.65)$$

It is clear the eigenproblem shown in eq. 2.60 has to be solved in order to obtain the dispersion relation.

The solution of the reduced eigenproblem ( $\omega$ ), has to be determined by considering a specific range of values of non - dimensional wavenumber  $\xi$ . It is sufficient to consider values of  $\xi$  that belong to the First Brillouine Zone of the RVE. The choice of the First Brillouine Zone could change depending on the type of material considered or depending on the RVE geometry. Examples of common ranges are  $\xi = [0, \frac{\pi}{2}]$  or  $\xi = [0, \pi]$ . Obviously, the more the mesh is refined, more precise are the solutions of the eigenproblem.

## Chapter 3

# Training and Introductory Numerical Analysis

### 3.1 Premises

The aim of this chapter is to represent some analysis carried out with the micromechanics code *MUL2-UC* [25], namely a high-fidelity tool for the computation of the effective stiffness matrix, and the recovery of the local fields of periodically heterogeneous composite structure. This preliminary work is understood as an "introductory training" for the candidate in order to take confidence with the tools.

With the purpose to recall the basics theory elements and concepts which on the code is based, two assumptions must have done that are respectively:

- the arrangement of reinforcements of the composite material follows a regular and periodic pattern, recalling the concept of *repeating unit cell* (RUC). The latter is defined as the minimum geometrical entity that can be periodically repeated over the space to shape the higher scale structure [26];
- RUC must be much smaller than the global structure.

In order to solve the RUC problem, the micromechanics code refers to the Yu's *mechanics structure genome*(MSG)[27], using the correspondent concept of *structure genome*, defined as the smallest mathematical building block of the structure. MSG makes use of the *variational asymptotic method*(VAM)[28], to solve mechanical problems that involve smaller parameters and to provide efficient solutions for composite problems. It is worth to recall another concept from the theory that will be considered herein, namely the *Hierarchical Legendre Expansion*(HLE) beam models [29] that exploit the hierarchical characteristics of Legendre-based polynomials to construct a set of high-order polynomials that are used as arbitrary function over the cross-section. Finally, at the end of this introductory part, two main purposes have to be achieved using micromechanical analysis:

- Obtain effective properties of heterogeneous material represented by the RUC, to be used as inputs for the equivalent homogeneous material employed in the higher scale analysis. The procedure to obtain these kind of results is known as *homogenization*;

- Recover the displacements, strains and stresses local fields over the RUC volume from the outputs of the macroscopic structural analysis at the point of interest. The procedure to obtain these kind of results is known as *dehomogenization*.

What is presented in the following sections is the analysis of two main fiber-pack configurations that are circular fibre in square and hexagonal pack.

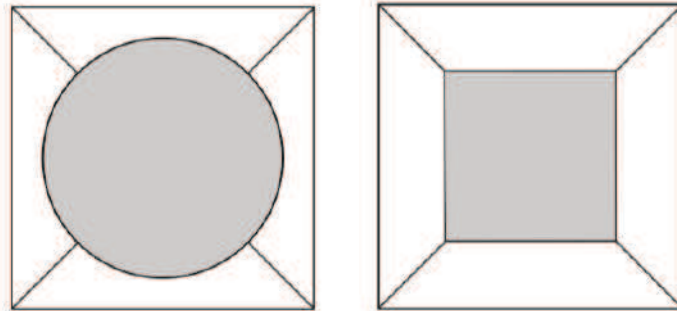
## 3.2 Circular fibre in square pack analysis

As previously stated, this section aims to provide a comparison between different results obtained by growing increasingly the polynomial orders of beam model.

The analysis has been carried out for two composite microstructures, respectively Boron-Aluminum and graphite-epoxy microstructure. Figure 3.1 shows the cell configuration and one can see how fibre is described by a single domain, whereas four domains model the matrix, for connectivity reasons.

At each of these domains, the polynomial order of expansion can be chosen by the tool user. Due to the high polynomial orders can be used in HLE theories, it is convenient to keep the domain as large as possible.

To fulfill this premise, a non-isoparametric mapping technique is applied to adapt the edges of HLE domains to the geometrical features of the different components of microstructure. For instance, in the case of square fibre, the distribution of domains over the cross-sectional surface is equivalent to that of the previous case, although no mapping technique is required since all the interfaces are straight.



(a) Circular fibre in a square pack      (b) Square fibre in a square pack

Figure 3.1: Different configurations Fibre-matrix and their domain

### 3.2.1 Boron-Aluminum

In table 3.1 is shown a resume of single homogeneous material properties, namely the key element to perform the analysis. As seen, in this initial case, both fibre and matrix are considered isotropic. Besides the polynomial order, that will be the unique variable of the analysis, another data input is required from the code, i.e. the *volume fraction of the fiber*, that take into account the encumbrance of the fiber with respect to the matrix in the considered pack. Here is used a volume fraction of the fiber equal to 0.47 (47%).

Once the analysis has been conducted (i.e the first homogenization step is concluded), the code generates several data as the number of effective DOFs and the homogenization computational

Material	$E[GP a]$	$\nu$
<i>Boron(fibre)</i>	379.3	0.1
<i>Aluminum(matrix)</i>	68.3	0.3

Table 3.1: Boron-Aluminum composite properties

time that actually are not important to the purpose of the discussion. Particular results which one would wish to highlight are for instance the stiffness and compliance matrix, but above all the effective (transversely isotropic) properties obtained for the equivalent heterogeneous material. The latter results are shown in table 3.2 changing the polynomial order of expansion.

CUF-MSG	$E_1[GP a]$	$E_2[GP a]$	$G_{12}[GP a]$	$G_{23}[GP a]$	$\nu_{12}$	$\nu_{23}$
<i>HL2</i>	215.6564	145.9942	55.15073	47.65003	0.1931988	0.250268
<i>HL3</i>	215.5731	144.9625	54.53747	46.55363	0.1943021	0.2507435
<i>HL4</i>	215.5683	144.3213	54.43739	45.98646	0.1943647	0.2537884
<i>HL5</i>	215.5644	144.1411	54.42109	45.85777	0.1944163	0.2544990
<i>HL6</i>	215.5637	144.1125	54.42065	45.84347	0.1944257	0.2546092
<i>HL7</i>	215.5634	144.1048	54.42005	45.84177	0.1944301	0.2546338
<i>HL8</i>	215.5633	144.1045	54.42009	45.84149	0.1944305	0.2546390

Table 3.2: Effective properties of the Boron-Aluminum cell (square pack).

As can be seen from table 3.2, from HL6, all the results tend to converge up to the three decimals. This is a proof of the micromechanics code *MUL2-UC* efficiency, that thanks to the 1D simplification (CUF) can achieve optimum results starting from not - so - high polynomial order degrees.

### 3.2.2 Graphite-epoxy

For the sake of completeness, the same kind of results obtained for Boron-Aluminum composite are reported. Care should be taken to notice that the fibre in this case is transverse isotropic, while matrix is still isotropic.

Table 3.3 shows the resume of single homogeneous material properties and table 3.4 shows the properties obtained for the equivalent heterogeneous material.

The volume fraction of the fiber is considered equal to 0.6 (60%).

Material	$E_1[GP a]$	$E_2[GP a]$	$G_{12}[GP a]$	$G_{23}[GP a]$	$\nu_{12}$	$\nu_{23}$
<i>Graphite(fibre)</i>	235	14	28	5.6	0.2	0.25
<i>Epoxy(matrix)</i>	4.8	—	—	—	0.34	—

Table 3.3: Graphite-Epoxy composite properties

CUF-MSG	$E_1[GPa]$	$E_2[GPa]$	$G_{12}[GPa]$	$G_{23}[GPa]$	$\nu_{12}$	$\nu_{23}$
<i>HL2</i>	143.1730	9.701994	6.288535	3.194313	0.2512880	0.3465209
<i>HL4</i>	143.1667	9.635702	6.089646	3.122848	0.2520889	0.3489441
<i>HL6</i>	143.1665	9.621785	6.085038	3.117086	0.2521234	0.3497985
<i>HL8</i>	143.1665	9.621002	6.084850	3.116947	0.2521256	0.349848

Table 3.4: Effective properties of the Graphite-Epoxy cell (square pack).

### 3.3 Circular fibre in hexagonal pack analysis

For benchmarking scope, the circular fibre in hexagonal pack case is proposed. Figure 3.2 shows a graphical example.

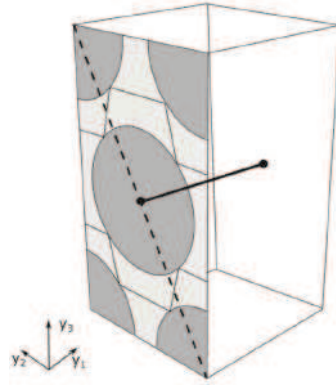


Figure 3.2: HLE beam model of the hexagonal pack cell RUC

The same homogenization process has been carried out for hexagonal pack cell, taking into account carbon-epoxy composite.

Single homogeneous materials properties and the effective properties of the equivalent heterogeneous material are set out respectively in table 3.5 and tables 3.6, 3.7.

The volume fraction of the fiber is considered equal to 0.6 (60%).

Material	$E_1[GPa]$	$E_2[GPa]$	$G_{12}[GPa]$	$G_{23}[GPa]$	$\nu_{12}$	$\nu_{23}$
<i>Graphite(fibre)</i>	276	19.5	70	5.74	0.28	0.7
<i>Epoxy(matrix)</i>	4.76	—	—	—	0.37	—

Table 3.5: Carbon-Epoxy composite properties

The novel aspect that has been introduced in this section is the process of dehomogenization: it allows to start with the outputs of the macroscopical or real analysis in order to accurately recover the local fields.

It has a great impact in the prediction of strength and failure of the composite structure. In this section the performance of higher - order models on capturing high gradient in the hexagonal cell



CUF-MSG	$E_1[GP a]$	$E_2[GP a]$	$E_3[GP a]$	$G_{12}[GP a]$	$G_{13}[GP a]$	$G_{23}[GP a]$
<i>HL2</i>	167.6538	10.8359	10.8079	6,5632	6.6897	3.3980
<i>HL4</i>	167.6530	10.7148	10.7083	6.42351	6.4370	3.3563
<i>HL7</i>	167.6528	10.6828	10.6887	6.3981	6.4111	3.3398

Table 3.6: Effective properties of the Carbon-Epoxy cell (square pack): Young and shear modulus.

CUF-MSG	$\nu_{12}$	$\nu_{13}$	$\nu_{23}$
<i>HL2</i>	0.3115	0.3119	0.5986
<i>HL4</i>	0.3119	0.3120	0.6001
<i>HL7</i>	0.3121	0.3120	0,6003

Table 3.7: Effective properties of the Carbon-Epoxy cell (square pack): Poisson's coefficient.

is illustrated.

Unitary values of strain have been used in dehomogenization, and then it has been represented in graph local stresses in only one or a few directions.

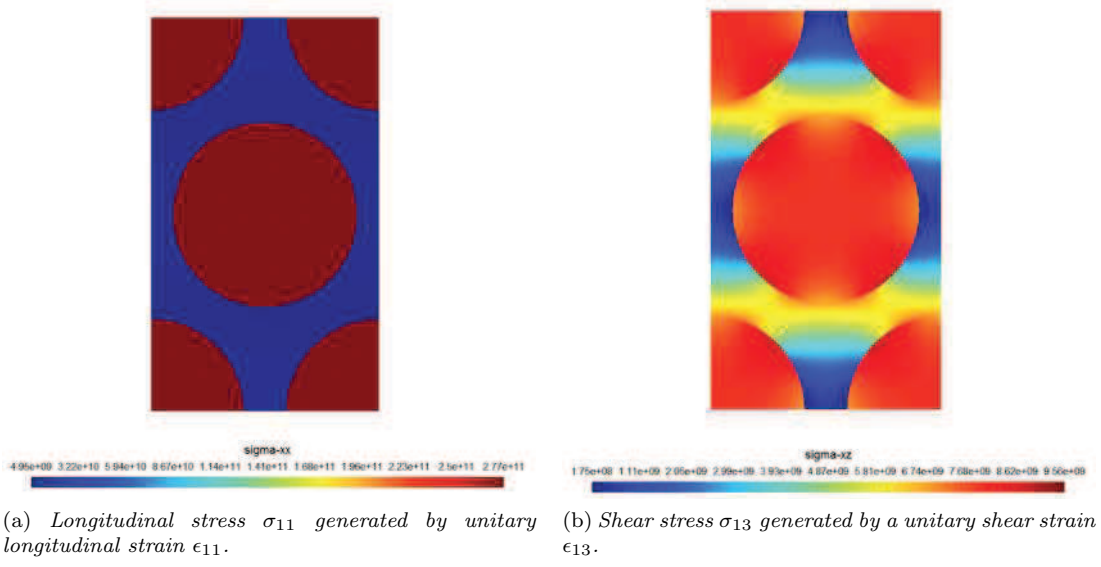


Figure 3.3

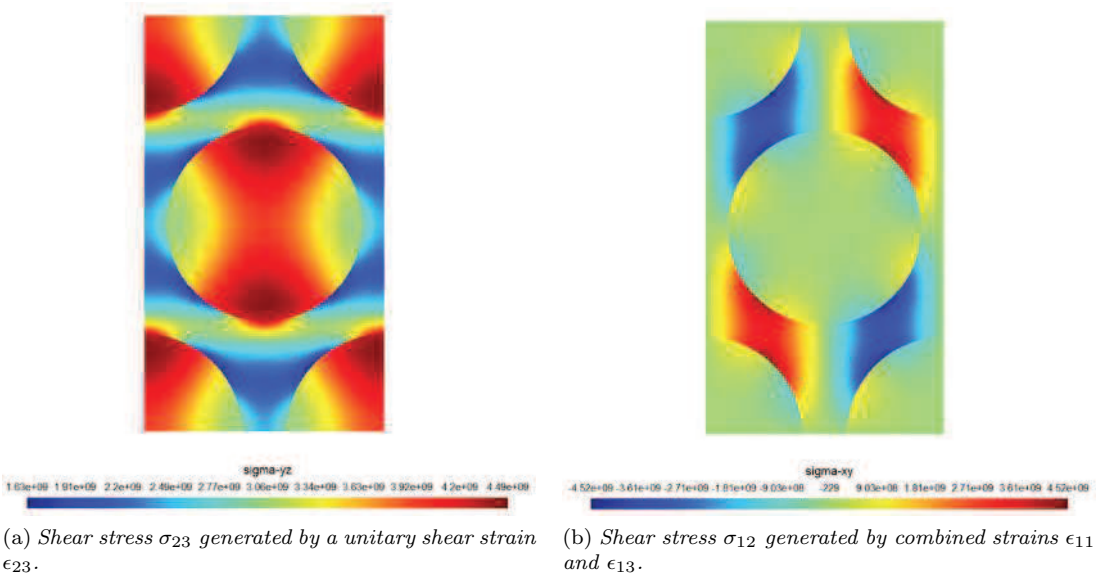


Figure 3.4

### 3.4 Square fibre in square pack with interface

In this section and in the subsequent one is possible to find a bit complex case with respect the previous ones. It has been introduced an interface between the matrix and the fibre.

Differently beforehand, it has been used Lagrangian L9 elements in order to build the mesh. New materials properties are reported in table 3.8.

Geometry of the cell is represented and described in 3.5 and 3.9.

This kind of model is designed by [7] referred to a metamaterial examined in [30]. It is worth to say that, in the interest of candidate training, final geometry described in 3.5 has been reached step by step, considering first a square cross-section fibre and coating (having the same cross-section areas) and then the original one.

It will be show in the following subsections how the results became more precise by using more and more dense meshes.

Material	$E[GPa]$	$\nu$	$\rho[kg/m^3]$
<i>Lead(fibre)</i>	40.8187	0.3697	11.6
<i>Silicone(coating)</i>	0.0001175	0.46875	1.3
<i>Epoxy(matrix)</i>	4.350049834	0.3679	1.18

Table 3.8: Composite material properties

Thickness of silicone coating	2.5mm
Length of unit cell	20.1mm
Radius of lead inclusion	20.1mm

Table 3.9: Model geometry features

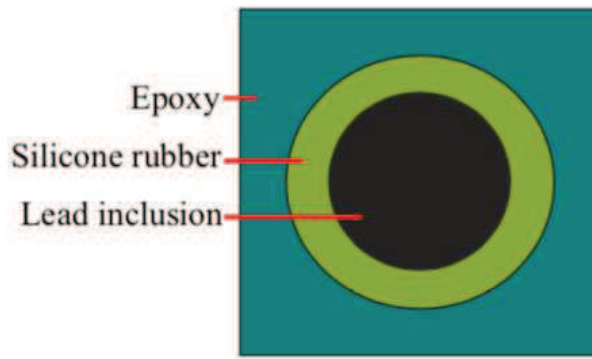


Figure 3.5: Cell geometry sketch [7]

### 3.4.1 Square fibre, square interface in a square pack

Here has been reported the effective properties of resultant heterogeneous material. It should be noticed that the material is transversal isotropic.

For this first case two kind of meshes have been used: a first coarse mesh and a second finer one which properties are listed in table 3.10. Tables 3.11 and 3.12 show a comparison between the effective properties achieved through the homogenization process of the first coarse mesh and the second finer one. Meshes are then shown in figure 3.6.

Mesh	Number of nodes	Number of elements
<i>Coarse</i>	81	17
<i>Fine</i>	137	29

Table 3.10: Properties of the two mesh considered

Mesh	$E_1[GP a]$	$E_2[GP a]$	$E_3[GP a]$	$G_{12}[GP a]$	$G_{13}[GP a]$	$G_{23}[GP a]$
<i>Coarse</i>	9.5456	1.8065	1.8065	0.5972	0.5972	0.1809
<i>Fine</i>	9.5456	1.7362	1.7362	0.5873	0.5873	0.1419

Table 3.11: Effective properties of the Epoxy-Silicone-Lead cell (square pack, square fibre and square interface): Young and shear modulus.

Mesh	$\nu_{12}$	$\nu_{13}$	$\nu_{23}$
<i>Coarse</i>	0.3679	0.3679	0.2246
<i>Fine</i>	0.3679	0.3679	0.2013

Table 3.12: Effective properties of the Epoxy-Silicone-Lead cell (square pack, square fibre and square interface): Poisson's coefficient.

As before, dehomogenization shows the local fields, receiving as inputs macroscopic (real structure) values of displacements and deformation. In this analysis and in the one related to the subsequent section, it has been used nil values for displacements and unitary values for deformations.

Observing figures 3.7 is possible to see how these two introductory meshes can be not really precise: looking at the internal matrix elements edges there are tension gradients (light charming) due to the bad mesh definition. It happens because mesh geometry doesn't describe with enough fidelity the real cell geometry. As one can see, this issue has been improved making the mesh denser, but has not been totally solved.

Remaining on figures 3.7, is worth to notice that the majority of the traction stress ( $\sigma_{yy}$ ) is supported by the fiber, whereas the rubber coating is barely charged and the matrix takes only a small amount of load.

As far as deformation is concerned, plotting deformation  $\epsilon_{xx}$  in figure 3.8 it is possible to notice how, at the same manner beforehand, deformation area doesn't cover exactly real deformation field of the interface. Obviously, the most deformed element will be the rubber coating having smaller Young modulus.

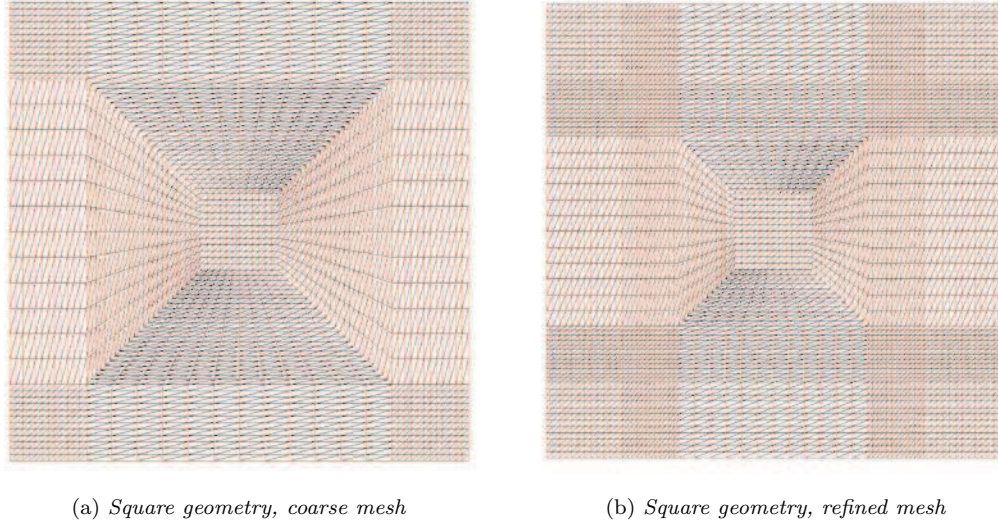
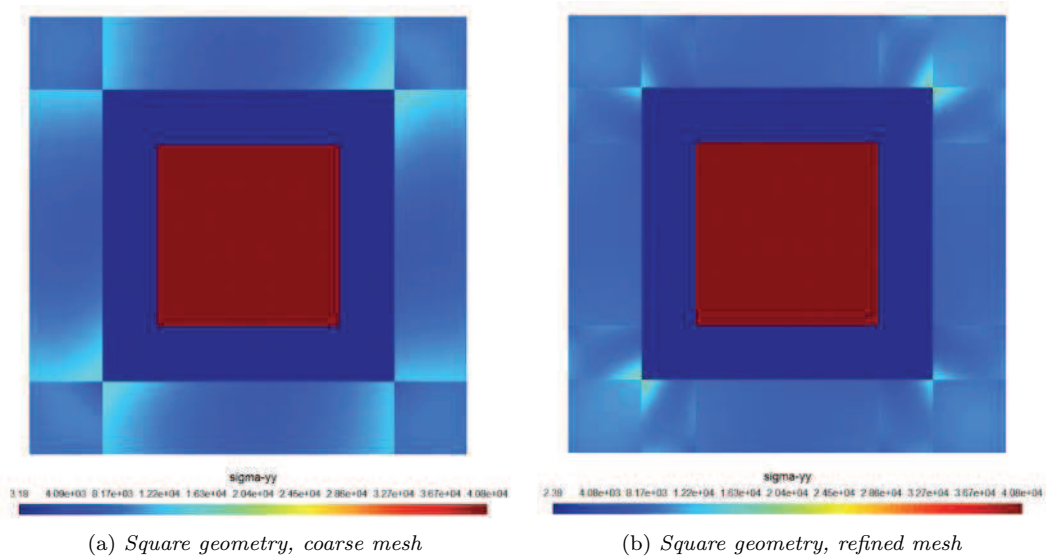


Figure 3.6: Representation of square meshes employed

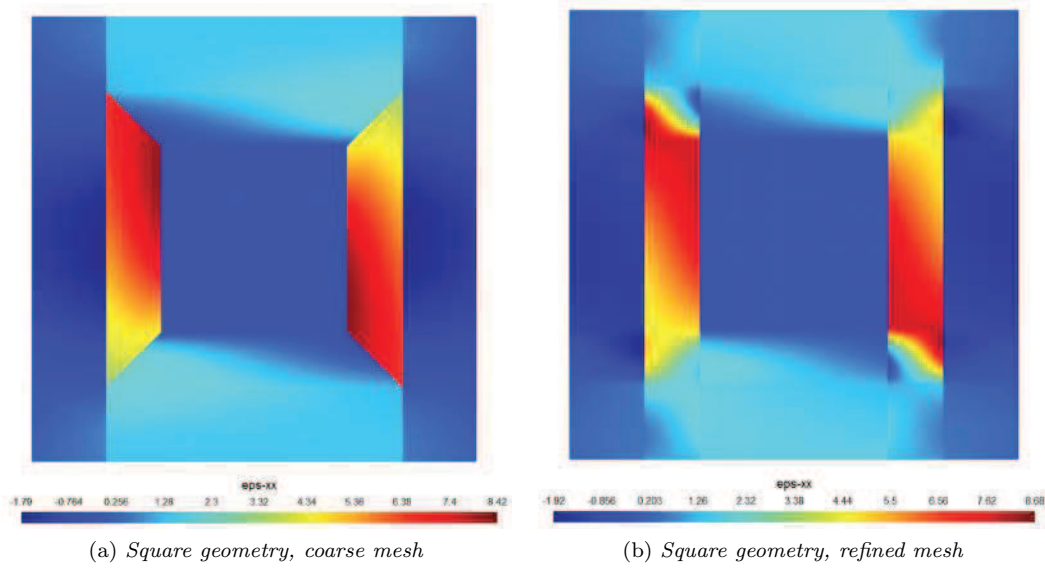
Figure 3.7: Longitudinal stress  $\sigma_{yy}$  generated by unitary longitudinal strain in all directions

### 3.4.2 Original circular fibre, circular interface in a square pack

Here, results are shown for the original cell shape. The mesh employed is quite more complex with respect the square ones already seen in the previous section due to the more difficult connection between the matrix "square - shaped" elements and the coating "circular - shaped" ones.

As it is possible to see in the following, the more is the mesh complexity, the more is the density and consequently the more is the results precision.

As far as the mesh properties are concerned, they have been reported in tables 3.13 and 3.15.

Figure 3.8: Deformation  $\epsilon_{xx}$  generated by unitary longitudinal strain in all directions

Number of nodes	Number of elements
177	40

Table 3.13: Circular mesh properties

As in the previous sections, effective properties of heterogeneous material are given in tables 3.14, whereas the employed mesh is represented in 3.9.

$E_1[GP a]$	$E_2[GP a]$	$E_3[GP a]$	$G_{12}[GP a]$	$G_{13}[GP a]$	$G_{23}[GP a]$
10.3777	1.7704	1.7704	0.6161	0.6161	0.2636

Table 3.14: Effective properties of the Epoxy-Silicone-Lead cell (original model): Young and shear modulus.

Following on from the tension gradient problem presented in previous section, it is clear that it can be considered solved, if one refers at current mesh 3.10.

Also the deformation field along x axis plotted on figure 3.10 is homogeneously distributed on all the interface (similar results are obtained obviously along z axis). In this regard, it should be noted that obviously the matrix along x axis undergoes a little amount of deformation. Contrariwise, the fiber is not significantly deformed.

### 3.5 First dynamic analysis

In this section it has been described the first modal analysis carried out through the old version of  $MUL^2$  code. It is worth to spend a few words about the code structure and characteristics.

First of all, it is edited in *Fortran 77*, a slightly more primitive with respect to the newest

$\nu_{12}$	$\nu_{13}$	$\nu_{23}$
0.3679	0.3679	0.2469

Table 3.15: Effective properties of the Epoxy-Silicone-Lead cell (original model): Poisson's coefficient.

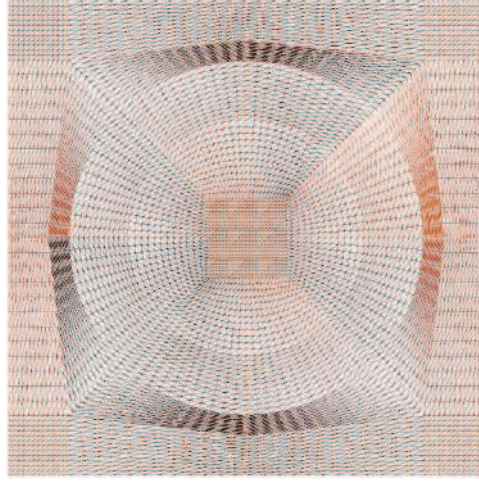


Figure 3.9: Representation of the original geometry mesh

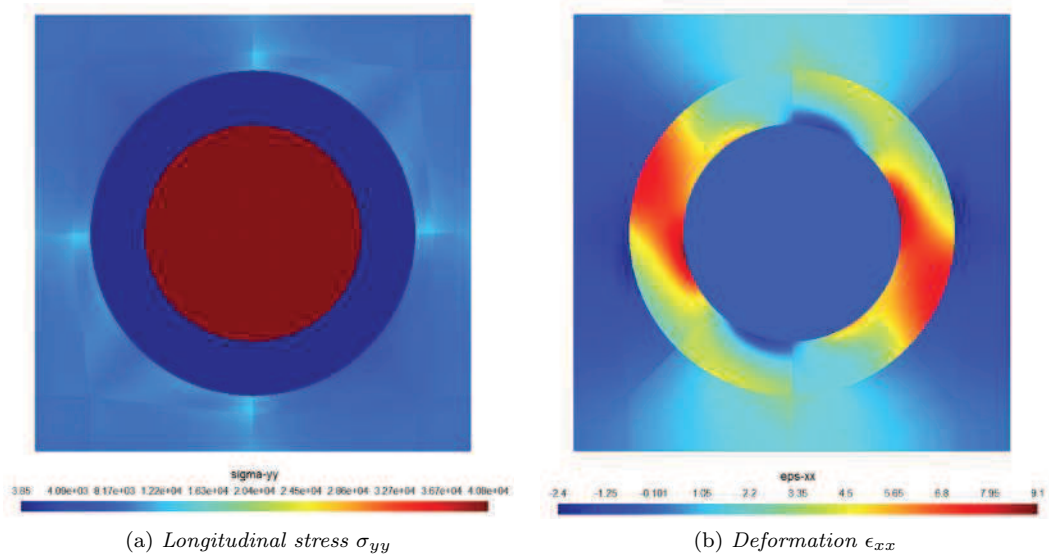


Figure 3.10: Longitudinal stress  $\sigma_{yy}$  (a) and deformation  $\epsilon_{xx}$  (b) generated by unitary longitudinal strain in all directions



version *Fortran 90/95*. The *MUL*<sup>2</sup> code will be used in this entire work is able to run FEM static and dynamic analysis of beam-like structures, basically supported by *CUF* (Carrera Unified Formulation).

As said before, the novelty of *CUF* approach is that it allows to carry out "lighter" analysis from the computational cost point of view, by generating and taking into account the one-dimensional longitudinal mesh and the two-dimensional cross section one, saving useless nodes.

The code is organized by subroutines, namely specific blocks of code, the aim of which is double, that is organizing better the work environment and giving the possibility to call them where they are required.

Getting to the point, the code has been modified in order to run a dynamic analysis taking into account *MSG* (Mechanics of Structure Genome) constraints. In other words it has been implemented the periodicity among the nodes that lie on square pack opposite sides. In practice, one has substituted the existent constraint subroutine with implemented periodicity.

In the next section it will be explained the main meaning of the analysis.

### 3.5.1 Physical meaning of the analysis and introduction to acoustic metamaterials

In order to understand clearly why dynamic analysis is carried out on this particular metamaterial cell, it is wise to take stock of the general topic.

Metamaterials are artificially designed composite materials which can exhibit properties that can not be found in nature [8]. There are several kinds like optics and magnetics metamaterials as well.

In the current case, namely elastic acoustic metamaterials, the abovementioned properties could be for instance the bulk modulus and the density. According to [8] they are used for the fine-tuned, predominantly frequency dependent control of the trajectory and dissipation characteristics of acoustic and stress waves. There are several useful metamaterials applications, but they won't be treated in our study for which is enough to understand the way to achieve such properties.

In order to pursue this aim, heterogeneous materials at appropriate length scales have been created.

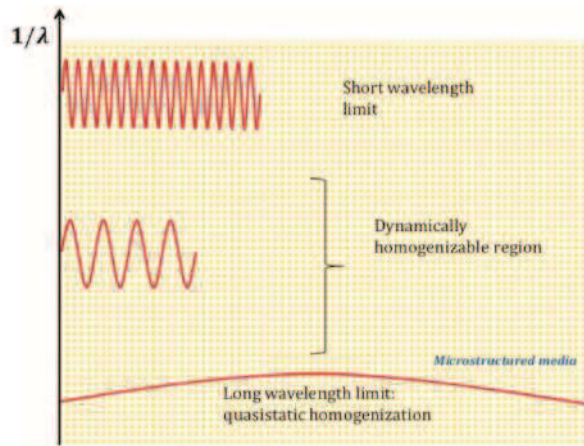


Figure 3.11: Homogenizable region [8]

Briefly, when the metamaterial cell is swept up by the wave, the vibration modes result to be



different mainly depending on the ratio between the wavelength and the microstructural length scale of the material in which it is traveling.

Figure 3.11 clearly shows the three broad regions in which the wave phenomenon can be analysed, here a summary description of these:

- The *low-frequency* region is correspondent also to the lowest one in graph 3.11. The frequency is low and consequently the wavelength is large.  
In comparison with the smaller dimension scale of the material microstructure, the sinusoidal pattern of the wave results to be crushed and lengthened. In that conditions it is possible to approximate the signal/load as quasi-static one by setting periodicity boundary conditions between the nodes that lie on square pack opposite sides.  
By using these BC's it one can state that the opposite sides of the square pack (right and left, upper and lower sides respectively) will deformate with the same elastic behaviour. These conditions are actually what is used in this first quasi-static dynamic analysis, in this region wave characteristics are non - dispersive and propagation is controlled by the static averages of material properties [8].
- At the other end of the scale there is the *high-frequency region*: the wavelength of the wave is on the same scale as or shorter than the length scale of the microstructure. Here is not possible to define effective properties of heterogeneous material by referring to the average homogenized properties, and the wave behaviour is described by scattering at material interfaces.
- In the middle region is possible to find an intermediate region in which effective properties are still defined by the average homogenized properties, but it should be take into account the dispersive nature of wave propagation. In other words, homogenized effective properties have to be frequency dependent.  
The next step of this work will consider this region and its goal will be to obtain particular dispersion curves, that will represent the frequency as a function of the wave number. This matter will be treated more thoroughly subsequently.



## Chapter 4

# Benchmark Analysis Evidence

### 4.1 Introduction

This chapter aims to be the official validation of the thesis work: it focuses on the derivation of the dispersion characteristics for different materials and geometry configurations.

For the sake of comparison, the works of Langlet [9], Geers [10] and Wang [12] have been taken into account. In the proposed approach, it has been applied the Bloch-Floquet theory [31] to an unit cell of periodic material.

Thanks to the modeling and the subsequent analysis of such materials, it has been possible to derive *dispersion curves*.

Mathematical methods for dispersion relation computation considered are cited in bibliography, but basically one can roughly describe the dispersion graph as it is built. For this purpose, on the x - axis  $k$  wave number is found, meanwhile on the y - axis lies the pattern of the  $\omega$  angular frequencies. Taking a look at the wave phase velocity definition 4.1 and thinking about the building of dispersion graph just described, one can realize actually the wave phase velocity is appreciable in the graph as the slope of the dispersion curve.

$$v_p = \frac{\lambda}{T} = \frac{\omega}{k} \quad (4.1)$$

Care must be taken in defining *phase velocity* and *group velocity*. Respectively, the first one accounts for the rate at which the phase of wave propagates in space, more precisely is the velocity at which the phase of any one frequency component of the wave (for instance, the wave crest) travels.

This latter, does not coincide necessarily with a *signal propagation* (so phase velocity could be higher than the light speed without violating special relativity), identified properly by the *group velocity*, that is the speed of each amplitude envelope containing a group of internal waves. Both the phase velocity and the group velocity vary with frequency, and the medium is called *dispersive*, consequently the relation  $\omega = \omega(k)$  is called *dispersion relation*.

Results of physical interest can be appreciated by modelling periodic materials and by plotting their dispersion relations [9]:

- Identification of propagation modes;
- Cutoff frequencies;
- Passbands, stopbands;

- Effective homogeneous properties.

It is worth to highlighth that for these first cases, the material is excited by a plane, monochromatic wave, which direction of incidence is characterized by an angle  $\theta$  (in the next cases it will be considered  $\theta = 0$ , so  $k$  is parallel to  $z$  direction). The incident wave is described by a real vector  $\mathbf{k}$ , the modulus of which is the  $k$  wave number.

As far as the dimensions of the problem are concerned, plain strain condition are used, then it only depends on  $x$  and  $z$  coordinates, considering the material to be infinite in  $y$  direction.

Once understood the main characteristics of the problem and the relevance they cover, in the next sections it is possible to find three benchmarks, respectively in ascending order of complexity. A brief description of each case will be provided.

## 4.2 Langlet: Homogeneous and Isotropic Material

An infinite, homogeneous and isotropic elastic medium is taken into account. The material proposed is Aluminum [9]:

$E[Pa]$	$7.31 \cdot 10^{10}$
$\nu$	0.325
$\rho[kgm^{-3}]$	2770

Table 4.1: Aluminum properties

As already precised in the introduction, material is considered to be infinite in the  $y$  direction using plane strain conditions, and the angle of the incident wave is  $\theta = 0$ . According to Langlet, the unit cell is a homogeneous square with a side length  $2d = 4cm$ . In figure 4.1 is represented the simple mesh configuration utilised.

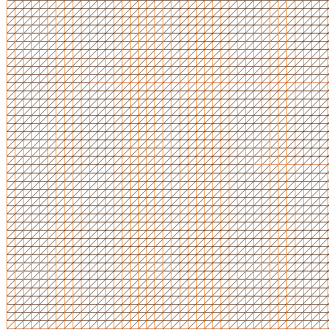
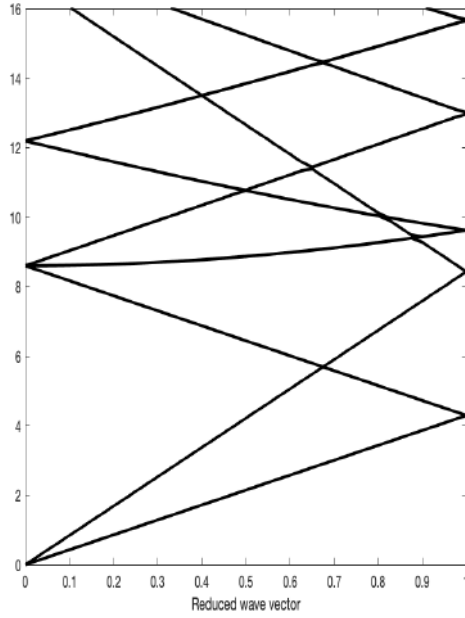


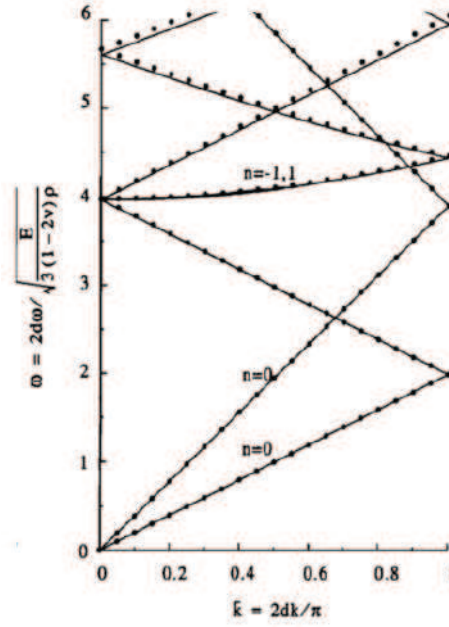
Figure 4.1: Unit cell mesh for homogeneous and isotropic material

In figure 4.2 is represented the final result of the analysis: for each  $k$ -step from 0 to 1 frequencies are calculated and plotted. One could notice that a scale difference is present in the *MUL2* graph, this is due to the fact that Langlet uses dimensionless "reduced" frequency and wave number coefficients, obtained through specific even non-linear expressions. This is irrelevant to the purpose of the present work.

It is worth to notice that in this first case the relation is linear, consequently the lines are straight (except the only one that is curved). Other consideration can be done: there is no band gaps, because all the straight lines coincide at the end of the range. In the next session it is possible to see how band gaps are created introducing an inclusion within the unit cell. Moreover, it is worth to show the first two transversal modes with related frequencies for  $k = 0$  in figure 4.3.

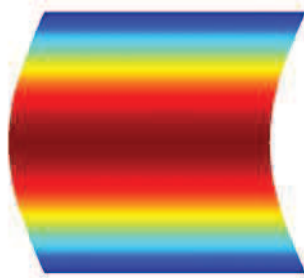


(a)  $MUL^2$



(b) *Langlet*

Figure 4.2: Comparison between dispersion curves for a homogeneous and isotropic elastic medium obtained with  $MUL^2$  micromechanics code (a) and obtained by Langlet et al. [9]



(a) *First mode*



(b) *Second mode*

Figure 4.3: Main views of the first and second mode at  $0.68339 \cdot 10^5 Hz$ .

### 4.3 Langlet: Square Inclusion

As introduced at the end of the previous section, a square brass inclusion of side  $2a$  is included at the center of the unit cell as showed in figure 4.4. Moreover, the inclusion material properties are listed in table 4.2.

Langlet work [9] shows how the maximum band gap is obtainable by varying the square inclusion dimension with respect the main dimension of the unit cell. For the sake of comparison, the ratio between the two sides of the squares chosen for perform the current analysis is  $a/d = 0.25$ .

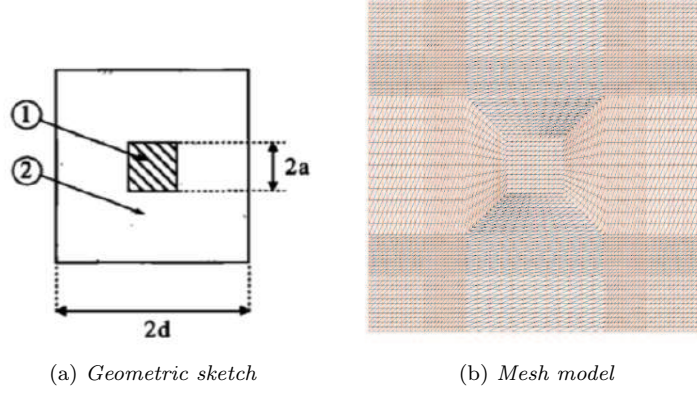


Figure 4.4: Unit cell configuration with a square brass inclusion: geometric sketch (a) and mesh model used (b) [9].

$E[Pa]$	$9.2 \cdot 10^{10}$
$\nu$	0.33
$\rho[kgm^{-3}]$	8270

Table 4.2: Brass properties

Even for this case, dispersion curves are presented as a comparison between  $MUL^2$  micromechanics code (b) and Langlet et al. work (a) [9] in figure 4.5.

As we can notice from figure 4.5, Langlet represents only the first two transversal modes for different  $a/d$  ratio. What is relevant for this work is obtaining the same shape of the modes that Langlet indicates as  $A1$  and  $A2$  and fundamentally the same band gap. Even in this case, numerical values are not correspondent with [9] for the same reason explained in the previous section. Find band gaps in dispersion graphs is really important because it means that a local resonance is experienced from the material. It allows the designer to shield sensible structures from the frequency range of the band gap.

Referring to figure 4.5 Langlet shows that the bigger is the area of the square inclusion, the larger is the band gap obtained and this works only until a certain limit is reached. At this limit, one can get the maximum obtainable band gap. As in the previous section first and second modes are shown in figure 4.6.

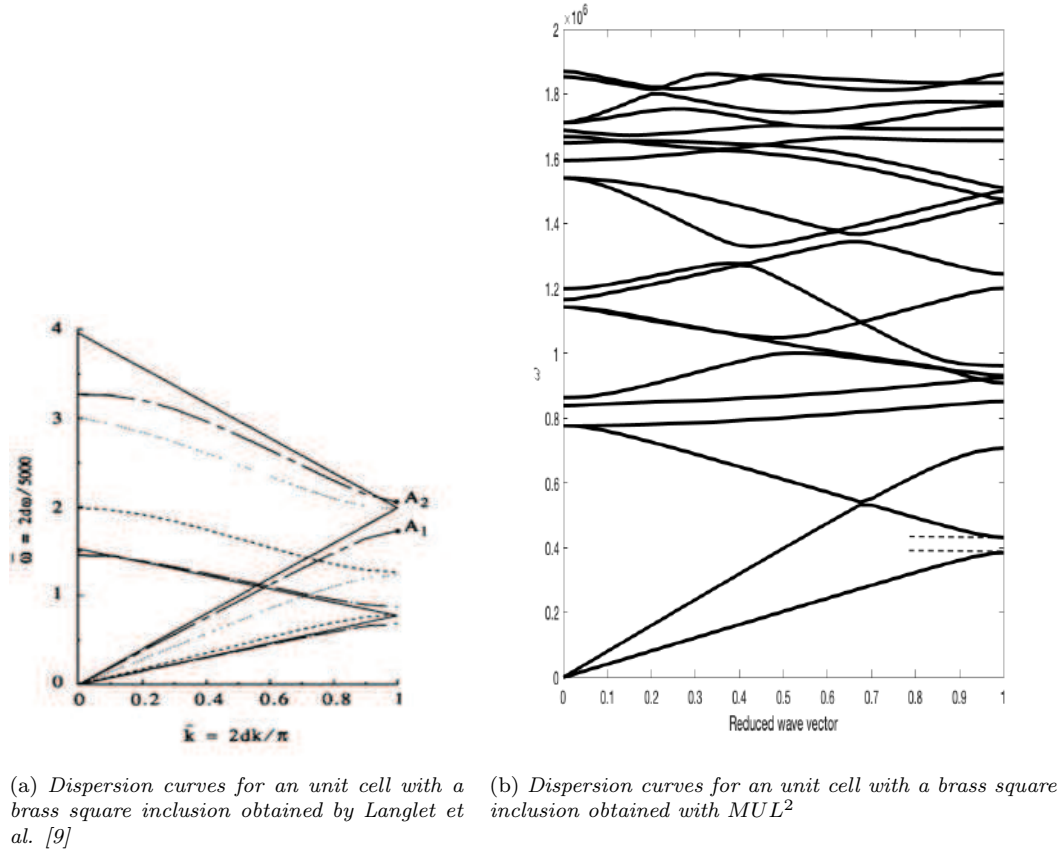


Figure 4.5: Comparison between Langlet dispersion curve (a) [9] and dispersion curves obtained with  $MUL^2$  micromechanics code (b).

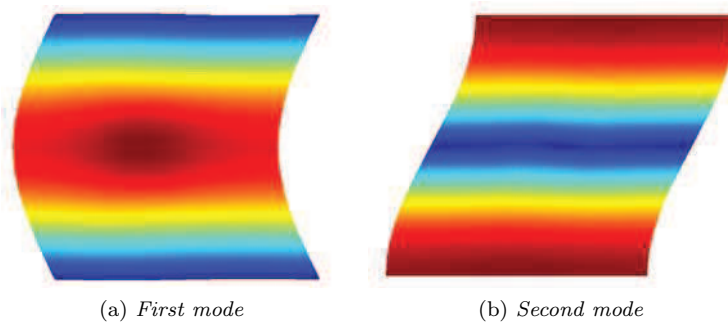


Figure 4.6: Main views of the first and second mode at  $0.6114 \cdot 10^5 Hz$ .



## 4.4 Geers

Taking into account the geometry related to Geers's work [10] one can notice that it has been already defined in figure 3.5 and tables 3.9 and 3.13 as well as materials in table 3.8. This cell looks different with respect the previous already analused due to the presence of a third component between the matrix and the fiber.

In figure 4.7 dispersion curve for this kind of composite material is found. According to Geers, the first stop band should be near the frequency of  $450Hz$ , the second one should be near the frequency of  $1330Hz$ . Still, it is not possible to see them in the dispersion curves plotted in figure 4.7.

Looking to the figures 4.8 and 4.9 it is possible to do a comparison between the results obtained by the  $MUL^2$  micromechanics code and Geers's work. In particular, one can observe how the modes shape is the same for the two cases, but the frequencies are still different.

As one could notice, talking about the mode pictures, it is possible to see some blank elements, due to some problems about connectivity, that could arise when the old version of the academic  $MUL^2$  micromechanics code is used. It is worth to highline that their presence does not influence the main result of the analysis, but they represent only an aesthetic imperfection. As it is possible to see in figure 4.7 the preliminary dispersion curve is very rough due to the scarcity of definition in the  $k$  domain. Geers curves have not a direct benchmark, so it has been a weak proof for what concerns the code validation.

Even thought it is not possible a direct comparison, similar flat mode patterns are easily found in lictérature, for cells having similar geometry.

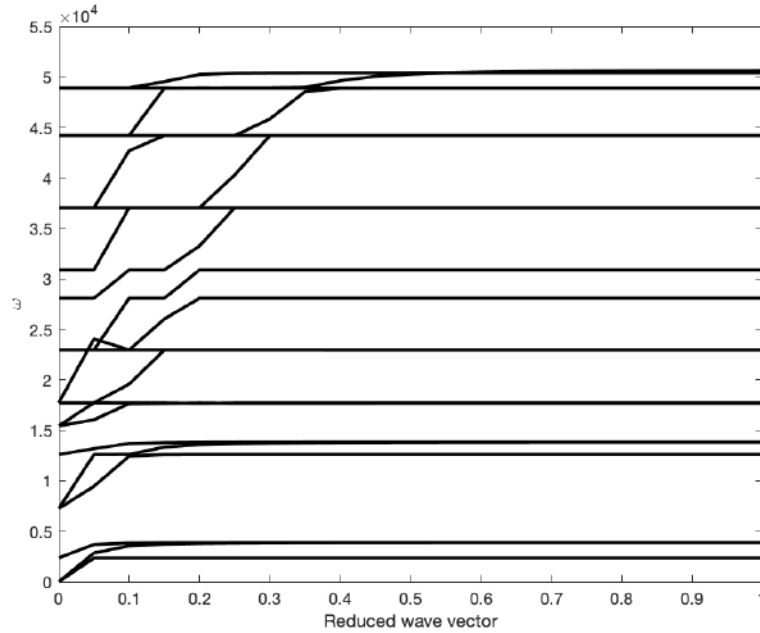


Figure 4.7: Dispersion curve obtained by  $MUL^2$  micromechanics code.

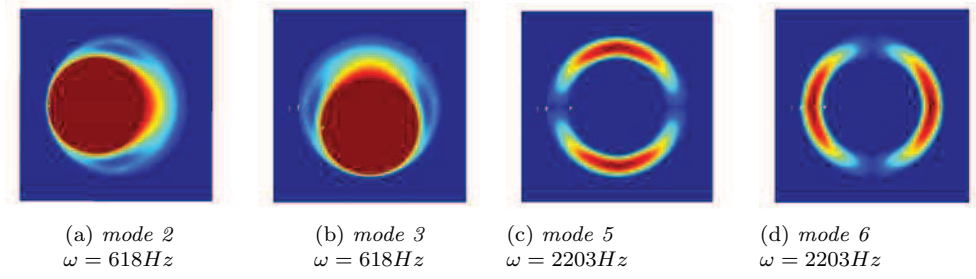


Figure 4.8: Modes obtained by  $MUL^2$  micromechanics code.

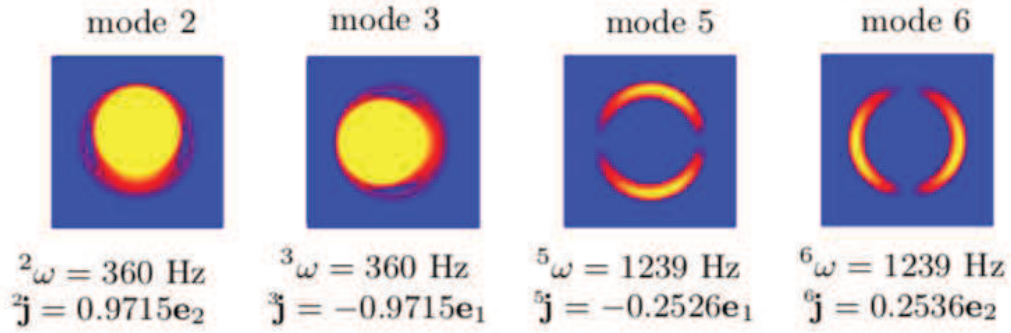


Figure 4.9: Modes obtained by Geers et al. [10]

## 4.5 Wang: Dispersion Curves

The aim of this section is to reproduce the results of Wang et al. [12]. In this case, as the previous ones, a two dimensional ternary locally resonant phononic crystal is considered. As far as it is known, this particular kind of metamaterial is used for vibration control and noise insulation and it is composed by a cylindrical scatterers with uniform coatings in their exterior. Wang et al. [12] have found that a complete band gap is experienced at low frequency. In that bandgap, the propagation of acoustic and elastic waves is prohibited.

Bandgaps are induced mainly by *Bragg scattering* and *local resonance*. Wang et al. results shows that a bandgap at a much lower frequency can be obtained by decreasing the modulus of the coating with the decrease of the bandgap width. Another way to experience bandgaps at a low frequency could consist in decreasing the area or the volume of the coating by introducing holes. The ternary locally resonant phononic crystal taken into account consists of cylindrical metal cores coated by rubber and embedded in the polymer matrix in a square lattice. Materials properties are listed in table 4.4. As said before, geometry is similar to that described in the Geers chapter and it is here revived in figure 4.10:  $r_1$  stands for the metal core diameter and coincides with the inner core of the coating, meanwhile  $r_2$  describes the outer diameter of the coating. As far as the geometry proportions are concerned, the following relations are used:

$$\frac{r_1}{a} = 0.27 \quad \frac{r_2}{a} = 0.4 \quad (4.2)$$

and they lead to the effective geometry dimensions listed in table 4.3.

$a[mm]$	$r_1[mm]$	$r_2[mm]$
20.1	5.427	8.04

Table 4.3: Phononic crystal geometry properties

	<i>Core</i>	<i>Coating</i>	<i>Matrix</i>
$E[Pa]$	$2.1 \cdot 10^{11}$	$1 \cdot 10^5$	$3.5 \cdot 10^7$
$\nu$	0.29	0.47	0.49
$\rho[kgm^{-3}]$	8950	1020	1200

Table 4.4: Phononic crystal materials properties [12]

According to the Wang et al. paper already cited, the band structure is characterised by a particular expression for the reduced frequency 4.3.

$$\Omega = \frac{\omega a}{2\pi c_t} \quad (4.3)$$

Where  $c_t$  is the transverse wave velocity of the matrix and it is not provided by the authors. Referring to the wave equation for a 1D case, it is possible to derive its expression 4.7. Starting from:

$$EA \frac{\partial^2 u}{\partial x^2} = \mu \frac{\partial^2 u}{\partial t^2} \quad (4.4)$$

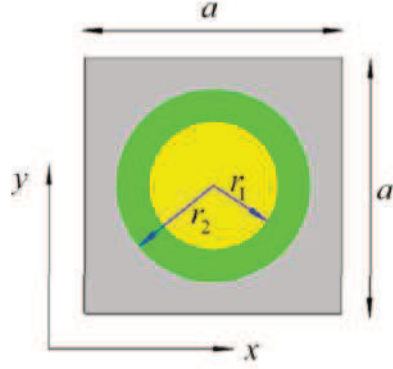


Figure 4.10: Phononic crystal geometry sketch [11]

And rearranging:

$$\frac{EA}{\mu} \frac{\partial^2 u}{\partial x^2} = \frac{\partial^2 u}{\partial t^2} \quad (4.5)$$

it holds:

$$c_t^2 \frac{\partial^2 u}{\partial x^2} = \frac{\partial^2 u}{\partial t^2} \quad (4.6)$$

Then

$$c_t = \sqrt{\frac{EA}{\mu}} = \sqrt{\frac{E}{\rho}} = 170.7825128 \frac{m}{s} \quad (4.7)$$

Before the results comparison, it is necessary a brief introduction to the notation used as far as the *First Brillouin Zone* is concerned.

In mathematics and solid state physics, the first Brillouin zone is a uniquely defined primitive cell in reciprocal lattice. The latter represents the Fourier transform of another lattice (usually a Bravais lattice)

The importance of the Brillouin zone stems from the Bloch wave description of waves in a periodic medium, in which it is found that the solutions can be completely characterized by their behavior in a single Brillouin zone. So it is possible give a definition: "*The first Brillouin zone is the locus of points in reciprocal space that are closer to the origin of the reciprocal lattice than they are to any other reciprocal lattice points*" [32].

That concept is important because Wang et al. plot the band structures along a path that is defined as  $\Gamma - X - M$ , according to the figure 4.11, delimiting the first Brillouin zone.

As one can notice in the figure, for the geometrical properties of the cell, the triangular area defined by the three segments is sufficient to describe the behaviour of the structure in terms of wave propagation. Following this reasoning, one has to plot the dispersion curves taking into account three main directions of the wave vector listed in table 4.5.

Figure 4.12 shows the three sectors just described together in a single image. One can notice that the first sector ( $\Gamma - M$ ) is mirrored for the sake of clarity in the representation.

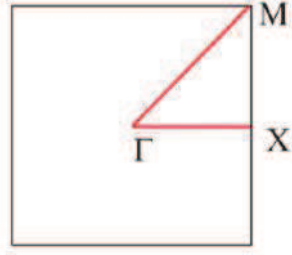


Figure 4.11:  $\Gamma - X - M$  path delimiting the first Brillouin zone [11]

$\Gamma - X$	$0^\circ$
$X - M$	$90^\circ$
$\Gamma - M$	$45^\circ$

Table 4.5: Three main directions of the first Brillouin zone [11]

Having laid the foundations for understanding the main concepts for the comparison, the results found out by carrying out the analysis with  $MUL^2$  micromechanics code are represented in figure 4.15.

In figure 4.13 it is possible to see that the  $MUL^2$  micromechanics code reproduce perfectly

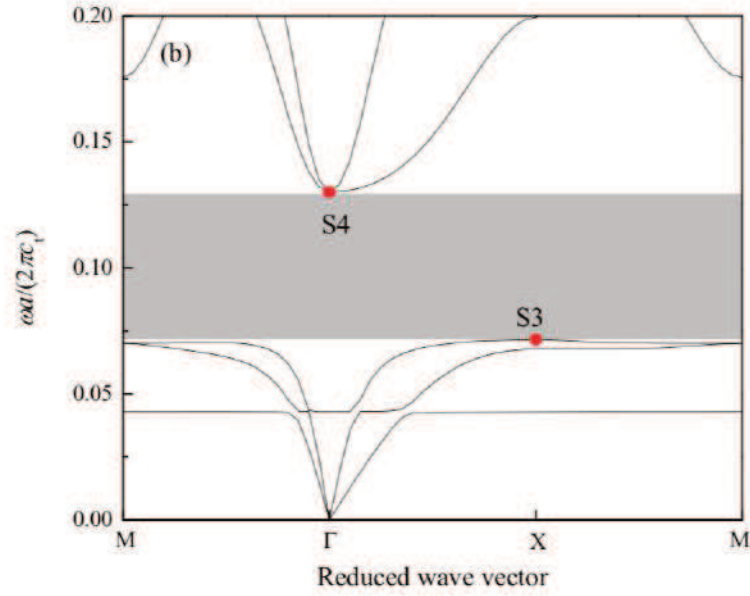


Figure 4.12: Dispersion curves obtained by Wang et al. [12]

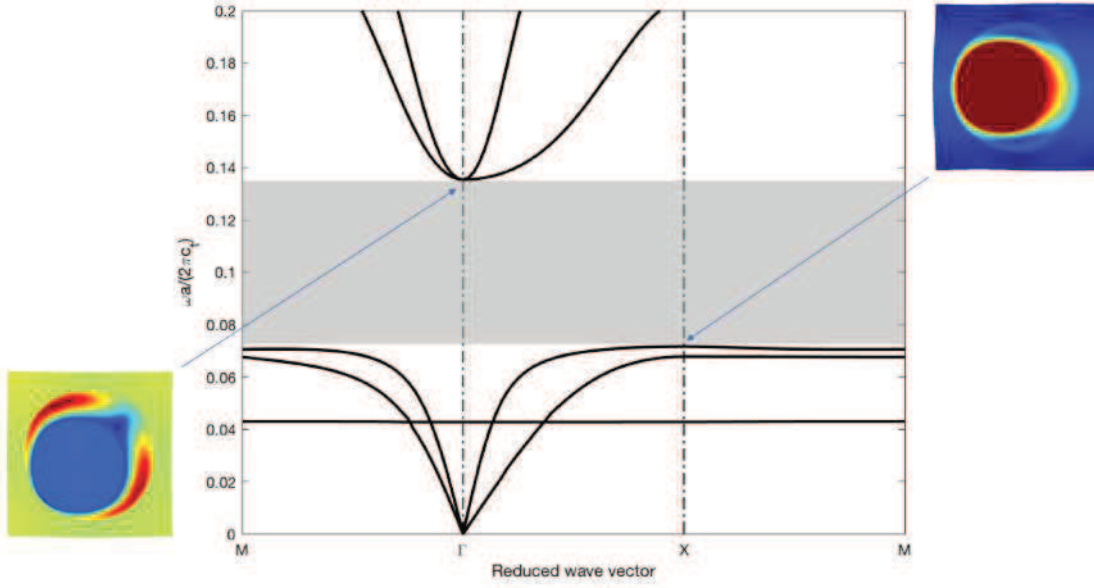


Figure 4.13: Dispersion curves obtained by  $MUL^2$  micromechanics code showing extreme band-gap modes.

Wang curves shown in figure 4.12. Thanks to this detail one can figure out the locally resonant nature of the lower bandgap because its maximum extreme point is "shifted" with respect the minimum one as explained in the theory part. Another comparison that is worth to carry out is the one related to modes of point S3 and S4 highlighted in figure 4.12. These modes are relevant due to their capacity to describe the motion of the structure at the extreme ends of the bandgap. As described in Wang et al. paper, at the lower edge of the bandgap, the core oscillates as a rigid sphere and the coating act as springs. While at the upper edge of the bandgap, the core and the matrix oscillates in a reverse phase [12].

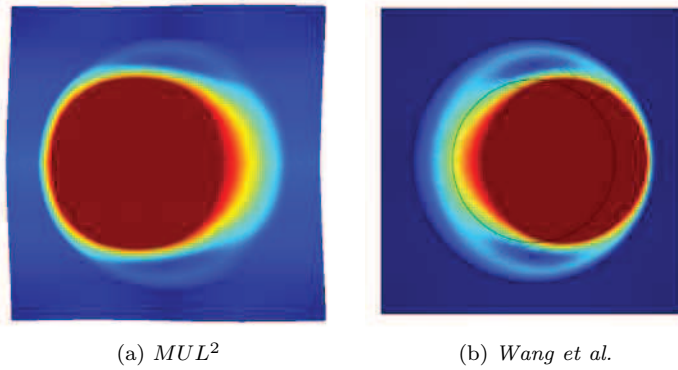


Figure 4.14: Comparison of the S3 point mode between  $MUL^2$  micromechanics code and Wang et al. results

For the sake of completeness, in figure 4.17 are reported the complete dispersion curve for two

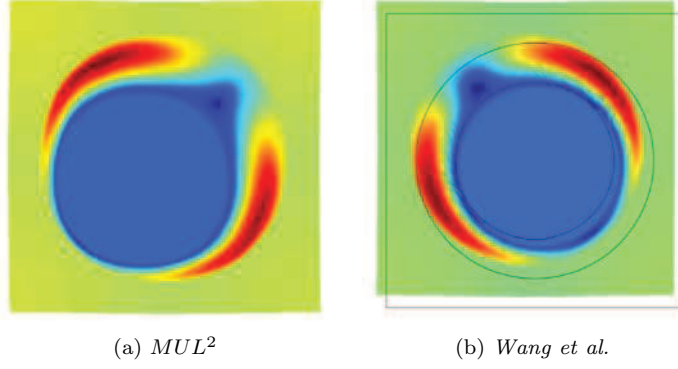


Figure 4.15: Comparison of the S4 point mode between  $MUL^2$  micromechanics code and Wang et al. results

of the three direction of the  $k$  wave vector.

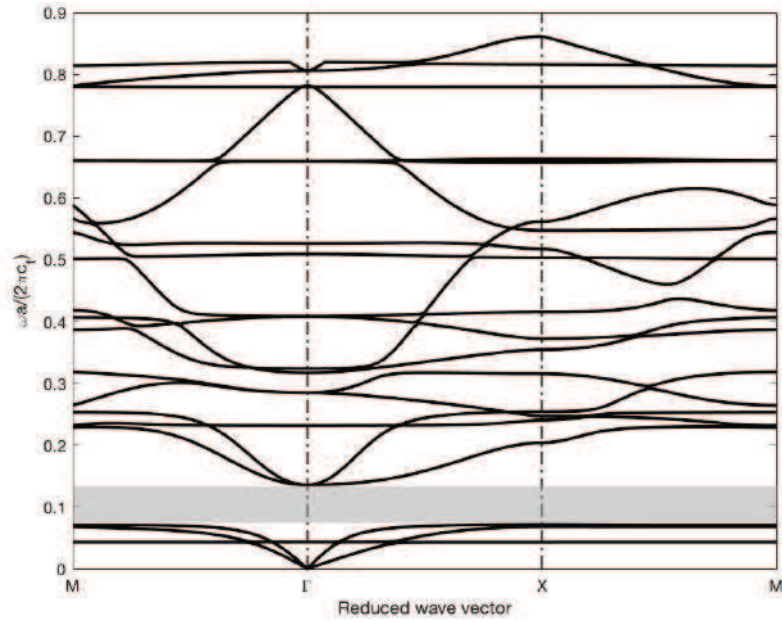


Figure 4.16: Full reduced dispersion curves obtained by  $MUL^2$  micromechanics code.

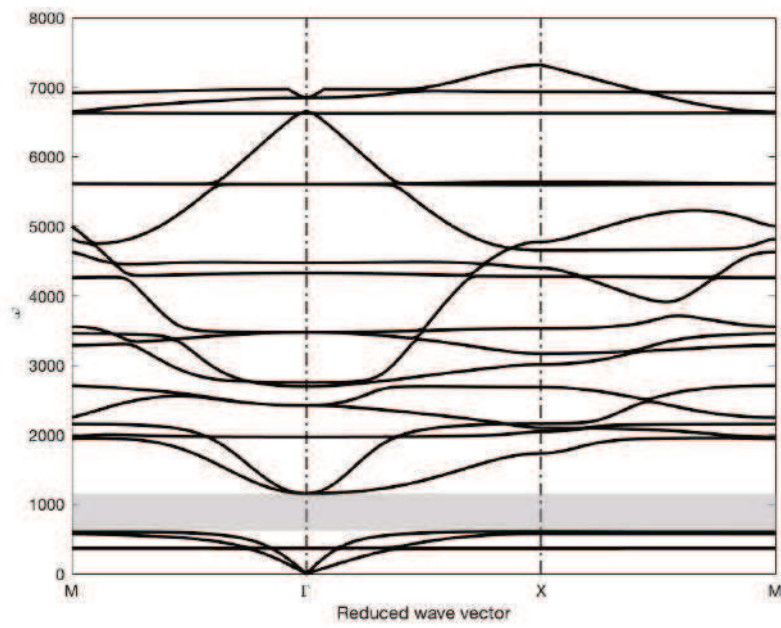


Figure 4.17: Full dispersion curves obtained by  $MUL^2$  micromechanics code.



## 4.6 Wang: Transmission curves

The transmission properties evaluation of a finite metamaterial system composed of eight unit cells is a really good way to display in another manner the properties of the bandgap on the wave propagation within the system itself. In figure 4.18 is possible to understand how the of the analysis has been set.

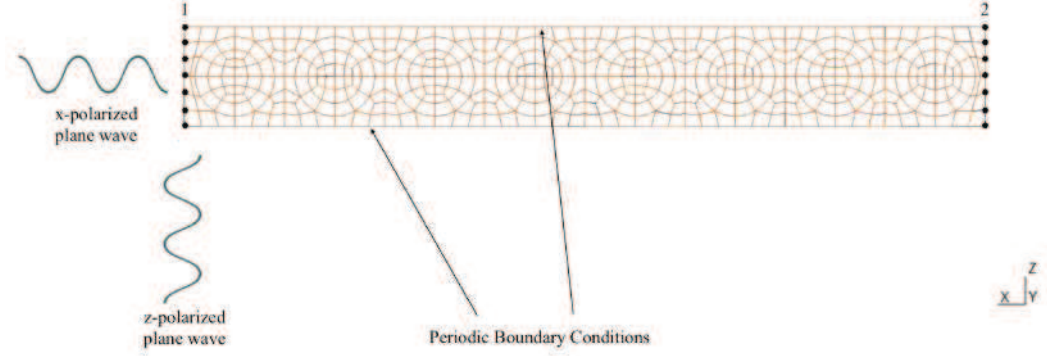


Figure 4.18: Transmission curves analysis set up

For first, a plane wave with unit amplitude is launched at the left boundary of the structure along the  $x$  direction. That particular kind of waves is called  $x$ -polarized (pressure wave). Secondly, it has been observed the propagation of the wave into the metamaterial with the concept of *transmission*, that in this work is defined as:

$$TCx = \log \left( \frac{\int_0^a |u_2| dx}{\int_0^a |u_1| dx} \right) \quad (4.8)$$

where:

- $|u_2|$  is the amplitude of the transmitted wave;
- $|u_1|$  is the amplitude of the incident wave, easily approximated to the unit value.

In figure 4.19 it is possible to see the analysis result, and particularly the bandgap between 512.5 Hz and more or less 820 Hz. Transmission relation allows to notice that the effective transmission bandgap could be involved into the dispersion curve bandgap. In other words, dispersion curves provide a bandgap that gives information about the frequency spectrum effectively cloaked, meanwhile transmission curves allow the understanding of "how much" the cloaking is good, giving a measure of the propagation of the wave into the finite medium. Every time a peak is represented in the transmission curve a maximum (or a minimum in the case of the bandgap) of the wave amplitude is reached, and a change in the wave phase occurs. The transmission curve is plotted only along the  $\Gamma - X$  direction of the first Brillouin zone.

A more detailed image is provided in figure 4.20, where the most important modes shapes are shown, such as the first and the ones at the extremes of the lower bandgap. The propagation attenuation is graphically really clear displaying the modes. The transmission has a sharp minimum at 537.5 Hz, where less than 1/8 of the array is involved in propagation.

Considering a z-polarized wave (shear wave), it is possible to get the transmission curve in the same way using the transmission relation:

$$TCz = \log \left( \frac{\int_0^a |u_2| dz}{\int_0^a |u_1| dz} \right) \quad (4.9)$$

leading to the result shown in figure 4.21.

For the y-polarized source, the transmission dip is larger and deeper and is seen in figure 4.23 and consequently attenuation of the y-polarized wave is larger than that of the x-polarized wave at all frequencies within the bandgap.

As for the x- polarized transmission curve, it is worth to visualize the most important modes shapes in a transmission curve detail. It is done in figure 4.22. The bandgap begins at 450 Hz and ends at more or less 820 Hz, with the minimum transmission point at 650 Hz.

As far as the two graphs are concerned, one can notice that wave propagation is clearly attenuated inside the bandgap and the bandgap width is almost the same for both the x- and z- polarizations.

The shape of the transmission curves is different due to the variations of the smallest imaginary part of the wave vector in the complex wave structure (not shown in this work) [11].

Finally, for the sake of benchmarking, a comparison between the transmission curves obtained through the *MUL*<sup>2</sup> micromechanics code 4.23 and the results obtained by Wang [11] 4.24 is proposed. Wang use a y-polarization source because z axis is considered as the longitudinal one in his analysis.

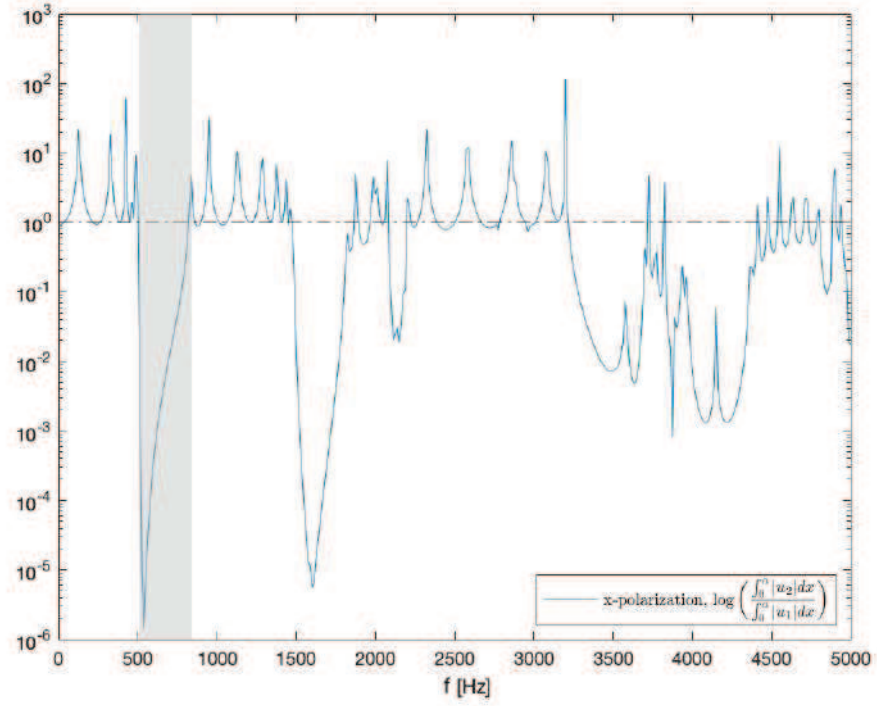


Figure 4.19: Transmission curve for a x-polarized plane wave

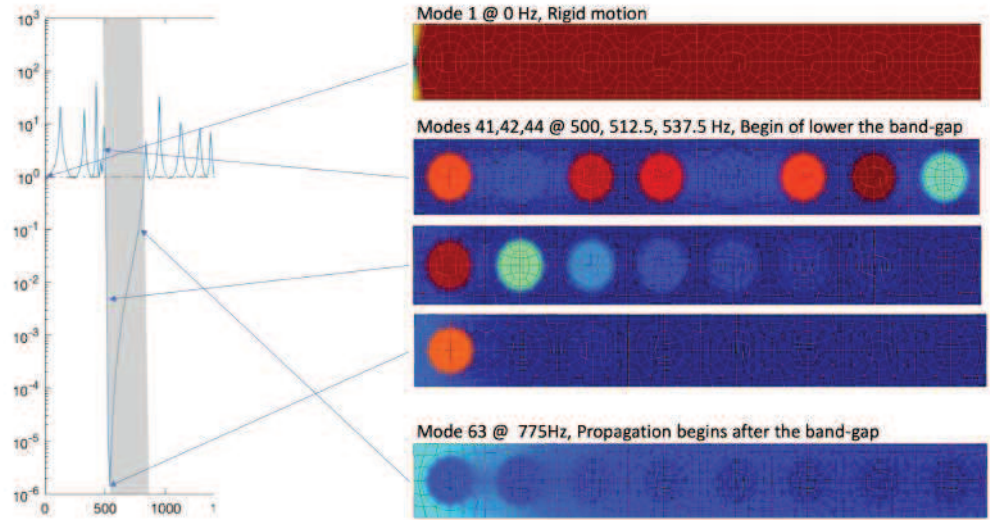


Figure 4.20: Detail of the transmission curve for a x-polarized plane wave, showing most important modes shapes

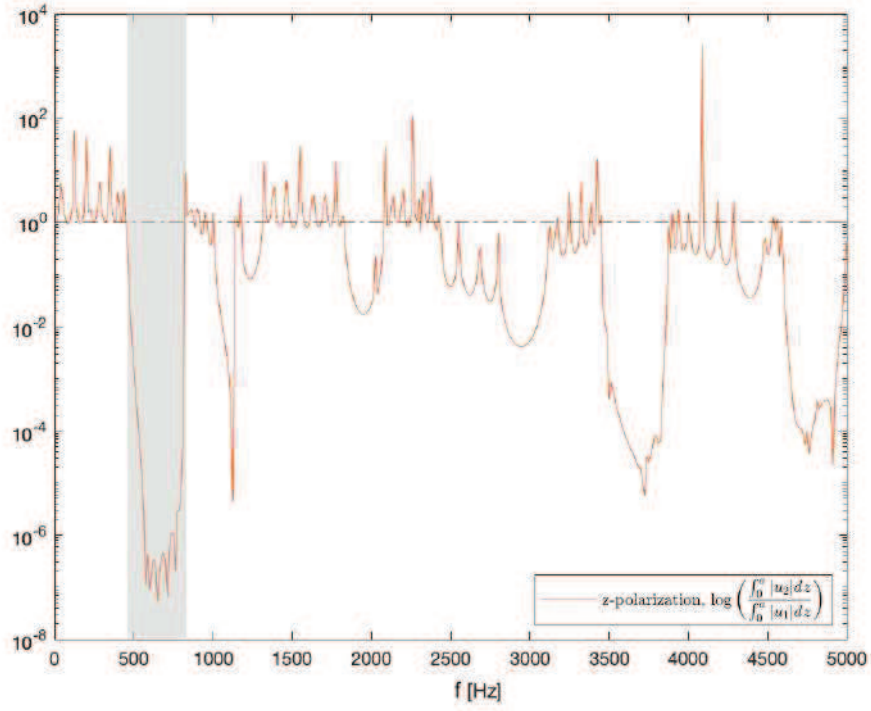


Figure 4.21: Transmission curve for a z-polarized plane wave

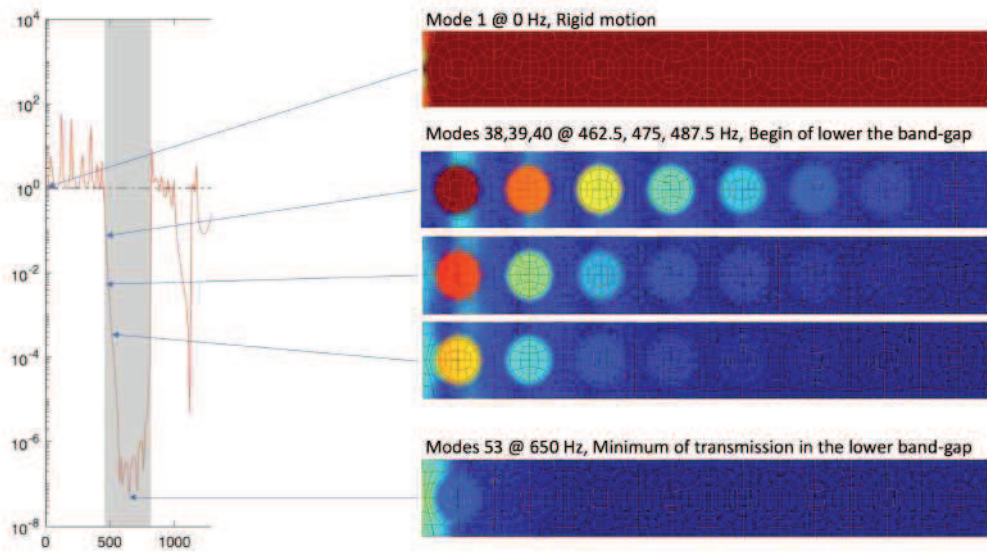


Figure 4.22: Detail of the transmission curve for a z-polarized plane wave, showing most important modes shapes

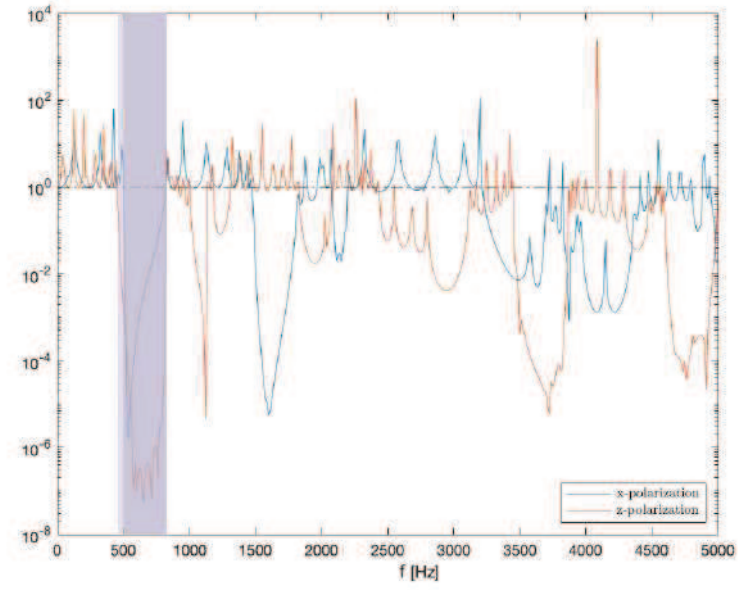


Figure 4.23: Transmission curves for both x- and z- polarized plane waves

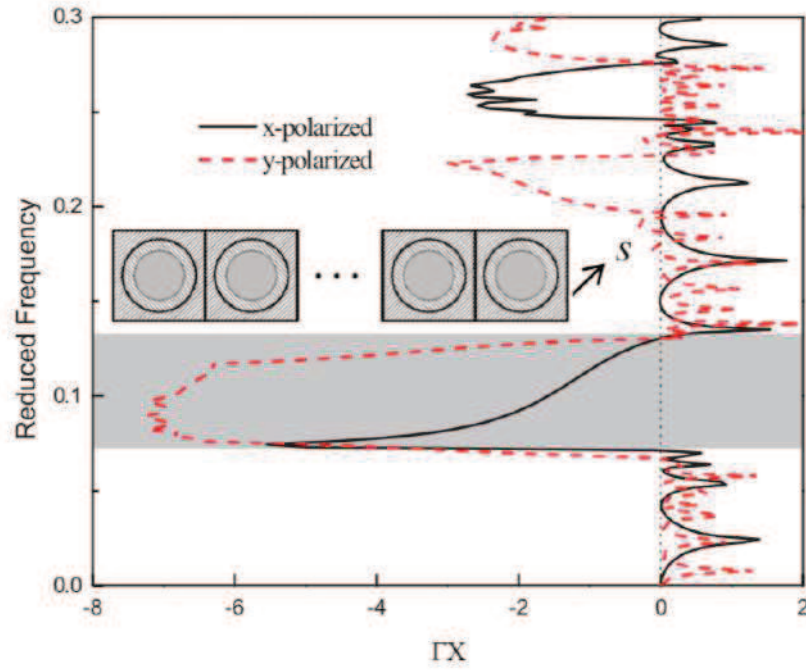


Figure 4.24: Transmission curves for both x- and z-polarized plane waves obtained by Wang [11]



## Chapter 5

# Case Study: Metamaterial for Aeronautical Applications

### 5.1 Introduction

This chapter could be considered the real "core" of the entire thesis work, because it investigates the soundproofing properties of a new passive metamaterial for aeronautical applications. The metamaterial taken into account is made of Melamine Foam and cylindrical Aluminium inclusions. Melamine is an organic compound having the formula  $C_3H_6N_6$  (fig.5.1) and it contains 67% Nitrogen by mass, and the massive presence of this element give it the fire retardant property due to its release of nitrogen gas when burned or charred. Beyond the fact that it is used as a good soundproofing, Melamine Foam is used in polymeric such a "Magic Eraser" as well. Moreover, Melamine is prohibited in the food industry due to its toxicity [13].

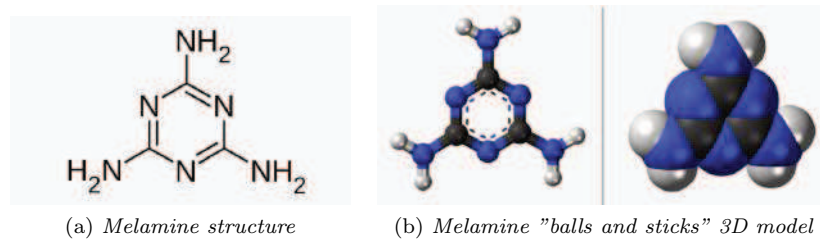


Figure 5.1: Melamine chemical description [13]

In that case, investigation is carried to use them for the improvement of aircraft cabin quietness. This work performs a deeper focus on the transmission and dispersion properties of the Melamine Foam - Aluminum passive acoustic metamaterial already taken into account by Cinefra et al. in [2]. According to the studies of Rayleigh [33] and Beranek [34], the problem of sound and vibration in the cabin is faced. It is worth to remind that regulations like FAR and EASA have to be considered as safety standards. These regulation do not provide a quantitative information of internal noise requirement, but only a qualitative indication. As Cinefra et al. [2] describe, standards highlight safety aspect and for the sake of clarity some examples can be provided. For instance, it is requested that vibration and noise of cockpit equipment do not interfere with safe operation of the aircraft, and that means that noise levels should allow a safe and easy communication among pilots and

flight crewmembers, but also that they should not cause distraction or nuisance.

Military standards cite internal noise requirements, but they are not concerned to the comfort aspect. This topic is also relevant in civil aviation. In fact, internal noise requirements mainly derived from airline requests, which are made directly to aircrafts manufacturers and that are based on passengers and cabin crew subjective response collected, for example, by means of questionnaires.

As explained in [1], noise in civil ariplanes is mainly produced by two sources: fuselage boundary layers and turbojet exhaust. Other four relevant sources are turbomachinery, cabin conditioning and pressurization system, structure and aerodynamic flow. Noise is transmitted to the cabin along airborne paths through the fuselage sidewall and along structure borne paths through the engine mounts or the wing structure. Every airplane has the same has its own characteristic sound, used by pylots as a diagnosys system. Usually, sound pressure level is comprised between 60 and 88dB, but it has been experienced that a long exposure over 85dB could cause hearing lost. Considering that for a turboprop airplane the near field noise excitation is mainly due to the propeller and then the major part of the acoustic energy is concentrated in the low frequency range (0 – 200Hz). An aspect of fundamental importance in defining internal noise requirements is referred to the acoustic treatments (alla the technical solutions or means installed on board) to increase the noise attenuation through the fuselage wall and to control the internal noise sources.

Thermo-acoustic blankets, skin damping, furnishing panels, mufflers and active noise control system are examples of noise treatment items. Basically, the system configuration needs to be designed taking into account several parameters, but the two most important factors that cover really important role (in aeronautic applications) are weight and cost. As far as the weight is concerned, if a regional turboprop is considered, the mass of fuselage blankets should be less than the 1.4% of the MEW (Manufacturer's Empty Weight, the weight of the aircraft "as built").

Acoustic metamaterial are made from assemblies of multiple element fashioned from composite materials such as metals,foam or plastics.

As said in the previous chapter and in th etheory section of this work , the main concept of metamaterial is to replace the molecules with man-made structures called unit cells. they can be seen as a sort of "artificial atoms" that are usually arranged in repeating patterns on a scale much less than the relevant wavelength of the phenomena they influence, (see Bragg scattering).

The principle idea is that locally-resonant acoustic metamaterials can be conveniently applied to aircraft interior, airframe noise in naval vessels, and controlling noise in automobiles as the order of magnitude of the wavelength is 1 m and this is much greater than the reasonable thickness of classical damping materials [2].

The aim of this work is to improve upon the scientific literaturew by further investigating a heterogeneous material and developing an efficient finite element model to evaluate the bandgap that the material experiences and how it change by changing the volume fraction of the unite cell. Moreover, transmission properties are going to be evaluated for understanding better how much the wave actually is propagating within an array composed of eighth unit cells of Melamine Foam Aluminium metamaterial.

## 5.2 Melamine Foam and Aluminum properties

Melamine is an orthotropic material that exhibits a viscoelastic behavior, and pratically it means that some of its properties are characterized by a real and an imaginary part (e.g. Young modulus). In several paper is shown that increasing the viscosity has no effect on the position of the extremes point of the bandgap, that remains unchanged. For instance, one can take into consideration the transmission curves plotted by Wang et al. [11] as shown in figures 5.2, plotted by increasing



the viscosity coefficient: it is possible to see that the position of bandgap does not change when viscosity increases.

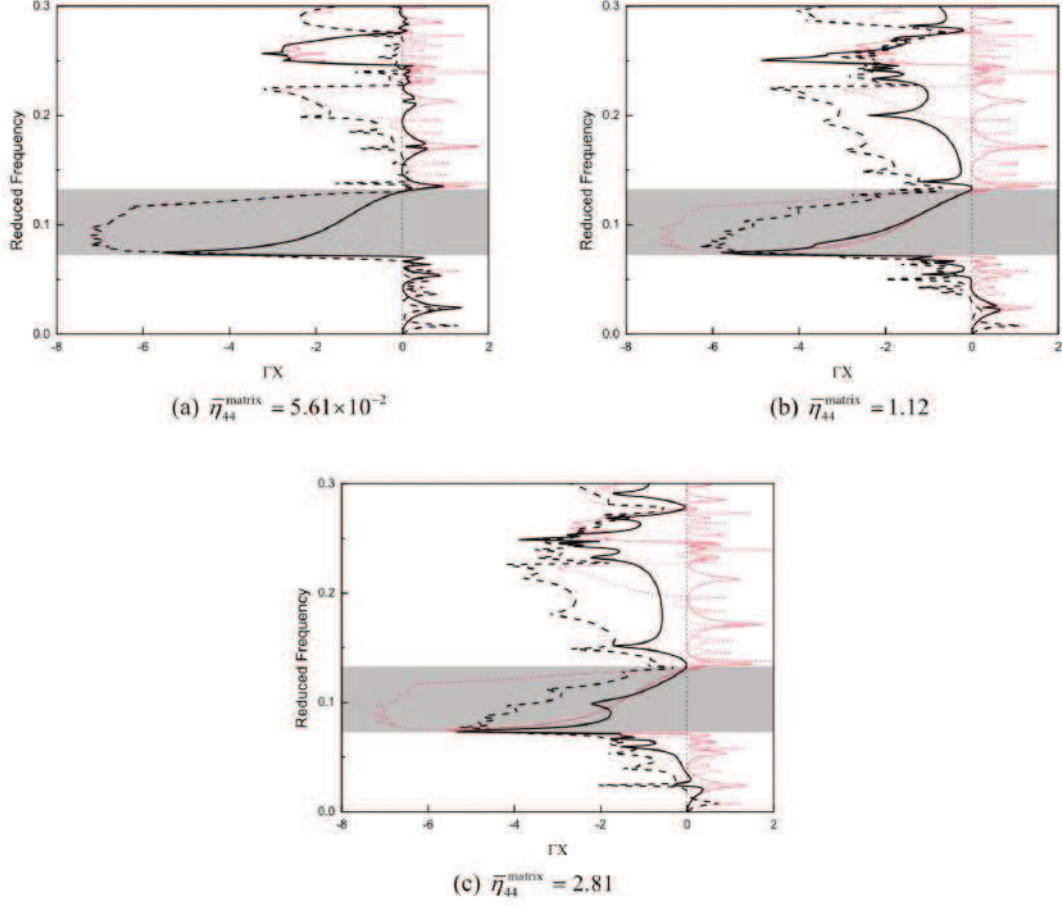


Figure 5.2: Transmission curve plotted by Wang et al. by changing the matrix viscosity coefficient [11].

After this consideration it is easier to understand that it is possible to evaluate the position of the bandgap even without considering the viscosity, namely without considering the imaginary part of the properties of melamine, that are fully described in tables 5.1, 5.2, 5.3. The properties shown are an average computed over a range of frequencies between 0 Hz and 4000 Hz.

$\rho[Kg/m]$	$E_1[Pa]$	$E_2[Pa]$	$E_3[Pa]$
8	458968.10125	21615.6615	174162.23625

Table 5.1: Density and Real Young modulus for Melamine [2].

On the other side, the inclusion is a cylinder made of Aluminum whose properties are listed in table 5.4

$G_{12}[Pa]$	$G_{23}[Pa]$	$G_{13}[Pa]$
103673.149375	106345.228125	127035.969375

Table 5.2: Real Shear modulus for Melamine [2].

$\nu_{12}$	$\nu_{23}$	$\nu_{13}$
0.445	0.433	-0.514

Table 5.3: Poisson coefficient for Melamine [2].

### 5.3 Geometrical features

As far as the geometrical characteristics of the Unit Cell are concerned, a Volume fraction of 0.0267 is taken into account. The side length is set to 5cm. The diameter of the inclusion is derived from this parameter through the formula 5.1 as defined in [1].

$$d = \sqrt{\frac{V_f}{\pi}} \cdot 2a \quad (5.1)$$

where  $d$  is the diameter of the aluminum inclusion,  $a$  is the side length of the square Unit Cell and  $V_f$  is the volume fraction (Volume of the inclusion / Volume of the matrix).

All the geometric data is collected in table 5.5

The Periodic Unit Cell of the Metamaterial with matrix of viscoelastic foam and cylindrical inclusions of aluminum is shown in figure 5.3.

### 5.4 Mesh

The Unit Cell mesh has been done with Abaqus CAE and then subsequently converted in a numerical input data through to a CUF tool. The elements chosen are quadratic and they are characterized by the L9 type, that it means Lagrange Expansion - 9 nodes for each element. For the sake of computational simplicity the mesh seed is set to 4 reference nodes for each side and to 8 nodes for the boundary of each inclusion.

Referring to the picture 5.4, one can see the mesh model of the array composed of eight Unit Cells used for the computation of the transmission properties of the metamaterial.

### 5.5 Dispersion Curves

Taking into account the single cell, and changing properly the angle of the incident wave it is possible to plot the dispersion curves for the Melamine-Aluminum metamaterial. In order to understand how to correctly read the dispersion curves, a consideration has to be done. Melamine

$E[Pa]$	$\nu$	$\rho[Kg/m]$
$6.75 \cdot 10^{10}$	0.34	2700

Table 5.4: Properties for Aluminum [2].

$a$	$5\text{ cm}$
$V_f$	$0.0267$
$d$	$0.9218933\text{ cm}$

Table 5.5: Geometric features of the Unit Cell [1].

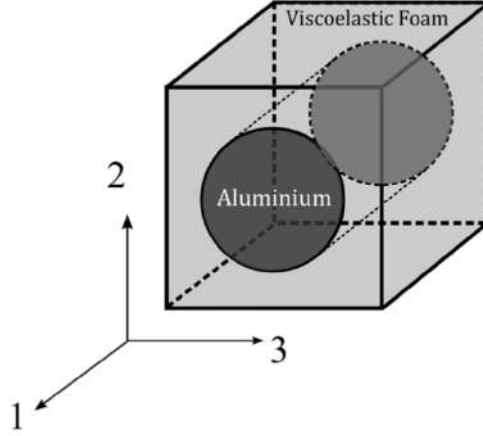


Figure 5.3: Periodic Unit Cell of the metamaterial with matrix of viscoelastic foam and cylindrical inclusions of aluminum [1].

is an orthotropic material, namely, it shows a different behaviour in  $x$  axis with respect the  $z$  one. This fact lead to consider a wider First Irreducible Brillouine Zone, with the aim of capturing all the existing propagation modes. In figure 5.5 it is possible to figure out all of the zones and contours that has been taken into consideration for building the Dispersion Curves.

The  $\Gamma - X_1$ ,  $X_1 - M$  and  $\Gamma - M$  paths are obtained as in the previous analysis, meanwhile the  $M - X_2$  and  $X_2 - \Gamma$  paths are obtained differently:

- $M - X_2$  path is obtained by varying the incident wave angle from  $90^\circ$  to  $0^\circ$  taking only the wave reduced number  $k = 1$  component of the vector;
- $X_2 - \Gamma$  path is obtained by keeping the incident wave angle to  $0^\circ$  and by varying the wave reduced number from 1 to 0.

The dispersion curves are reported in figure ??.

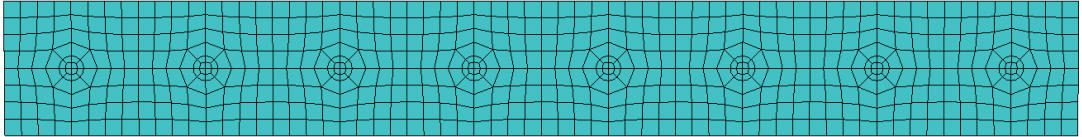


Figure 5.4: Mesh model of the array composed by eight Unit Cells mad with Abaqus.

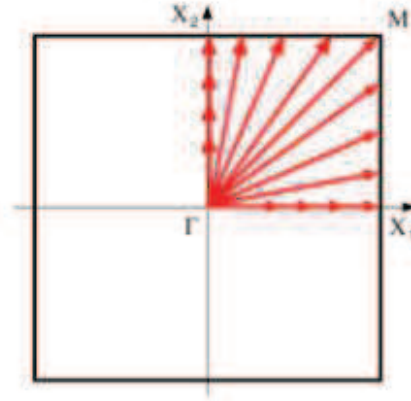


Figure 5.5: First Irreducible Brillouin Zone for an orthotropic material [14].

A careful analysis of the modes is required in order to understand the origin of the bandgap and the propagation properties of the Melamine-Aluminum metamaterial at low frequency. Then, the dispersion curves evidences will be compared with the transmission curves ones.

### 5.5.1 Bandgap Analysis

For the sake of clarity, the first five/four modes are plotted for the horizontal and vertical directions of propagation:  $\Gamma - X_1$  and  $X_1 - M$ .

If one is interested in exploring  $X_1 - M$  and  $M - X_2$  contours of the First Irreducible Brillouin Zone, it could discover that the modes are pretty messy due to both the effect of the angle of the incident wave and the effect of the orthotropic behaviour of the Melamine matrix.

As it is possible to notice giving a first sight at the dispersion curves in figure 5.6, the bandgap minimum frequency value of the higher extreme mode is "shifted" with respect the maximum frequency value of the lower extreme mode.

That consideration allows to touch base with the local resonance origin of frequency bandgap.

Another particular that one could be notice is that the bandgap is, let's say, "interrupted" by a plane mode that propagate indefinitely throughout the entire reduced wave number area. This kind of propagation is only apparent, because, as it is possible to see in figures 5.7, 5.8, 5.9, 5.10 and 5.11, this is a torsional mode that involve only the boundary of the inclusion. After a talk with Paolo Celli at California Institute of Technology, it was found that this kind of mode doesn't propagate normally, but only if it is properly excited.

The  $M - \Gamma$  area of dispersion curve represents the diagonal direction ( $45^\circ$ ) of the square shaped First Irreducible Brillouine zone, and it is added to the original square contoured dispersion zone for the sake of completeness.

An important consideration that one can do as far as the dispersion curve is concerned, namely that it is possible to see graphically the orthotropical behaviour of the matrix: if the matrix were isotropic, the curves would be symmetrical with respect to the axis  $k = M$ .

As it is possible to see from dispersion curves and better in figures 5.7, 5.8, 5.9, 5.10 and 5.11, the first and the fifth modes move transversally with respect the propagation direction, whilst the second and fourth move longitudinally. This fact is confirmed by the transmission curves in the next section, because the bandgap is thinner in the pressure wave polarization case and wider in the shear wave polarization one.

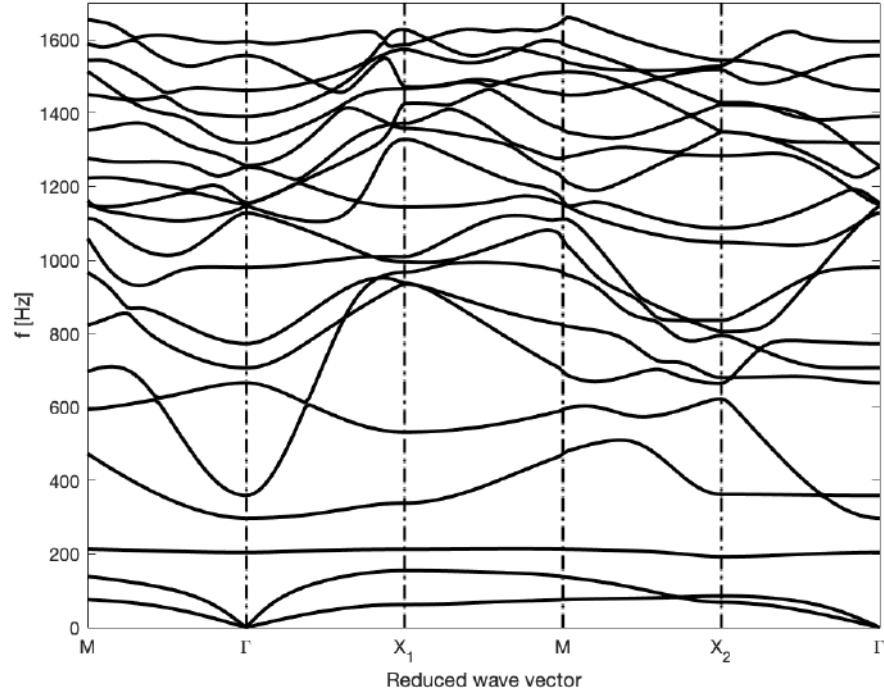
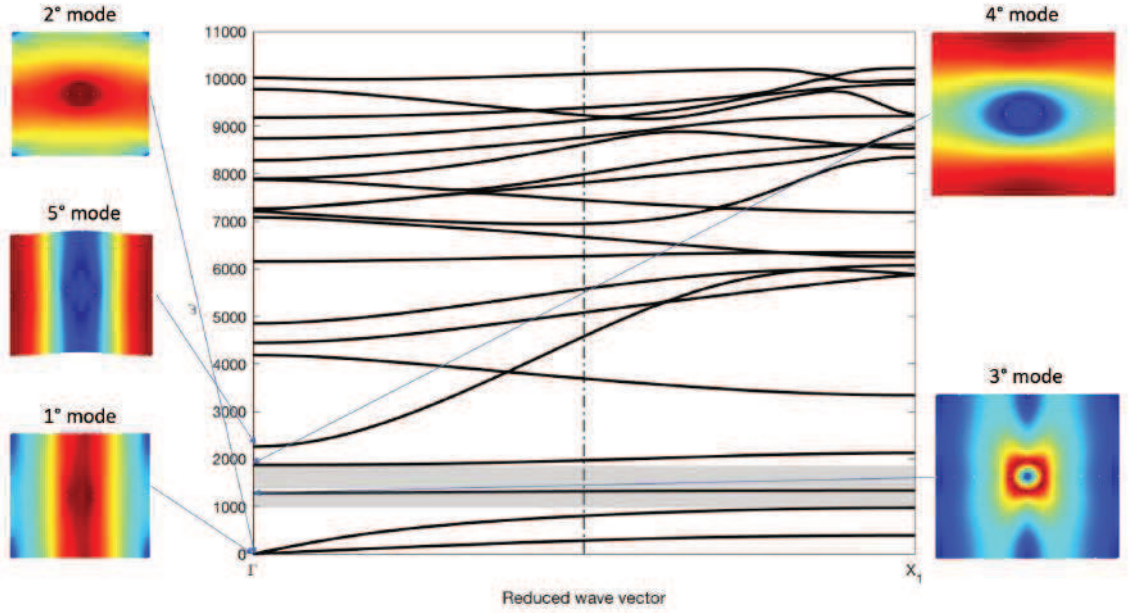


Figure 5.6: Complete Melamine-Aluminum metamaterial dispersion curve.


 Figure 5.7: First five modes of propagation in the  $\Gamma - X_1$  direction for  $k = 0$ .

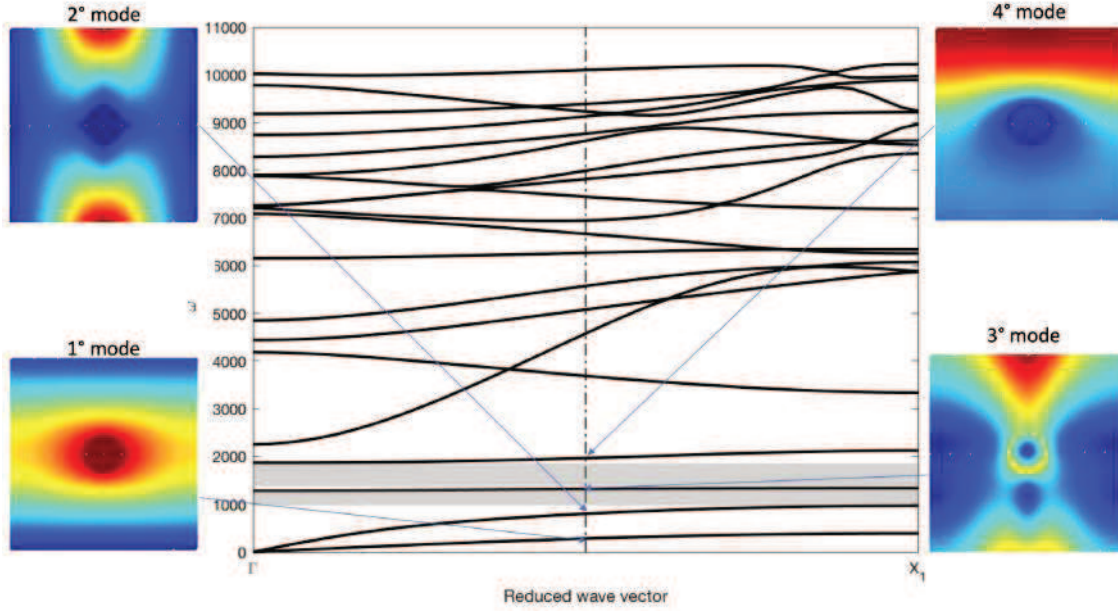


Figure 5.8: First four modes of propagation in the  $\Gamma - X_1$  direction for  $k = 0.5$ .

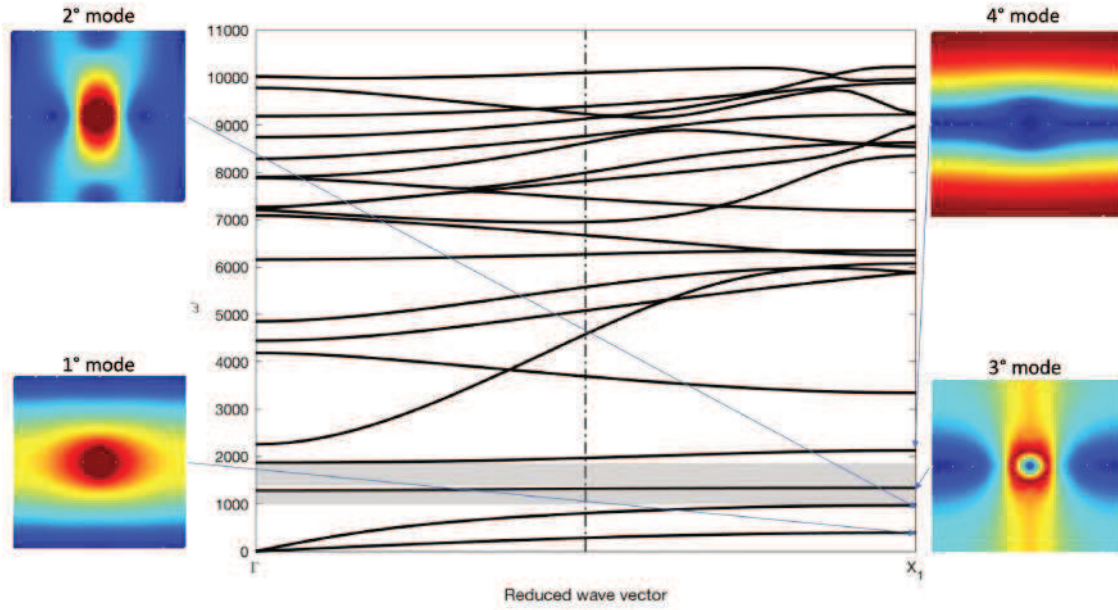


Figure 5.9: First four modes of propagation in the  $\Gamma - X_1$  direction for  $k = 1$ .



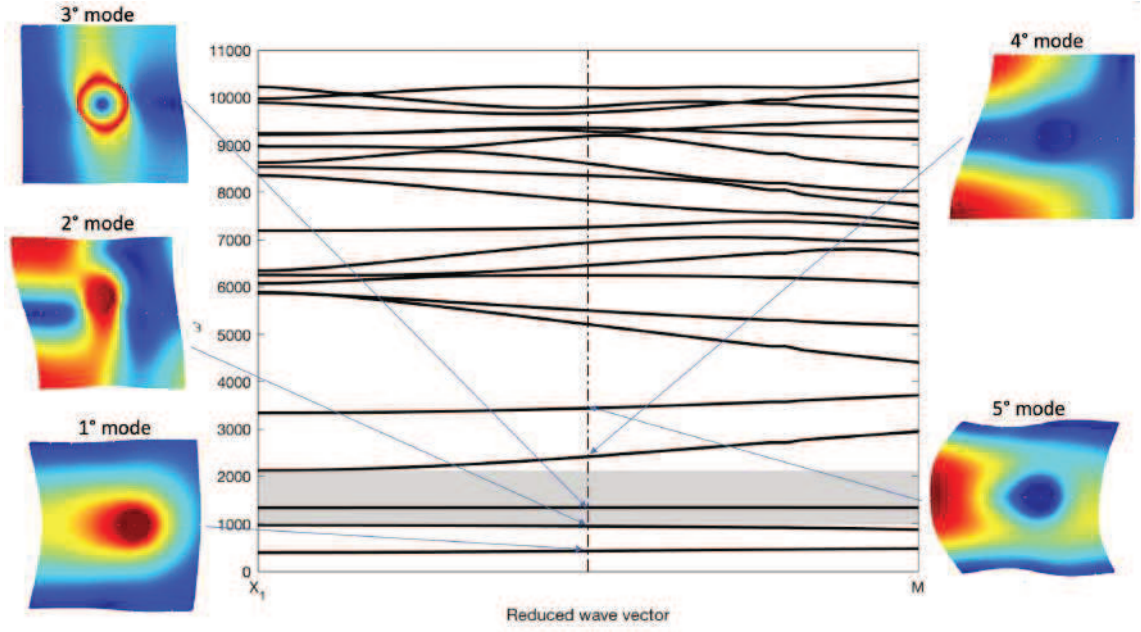


Figure 5.10: First five modes of propagation in the  $X_1 - M$  direction for  $k = 0.5$ .

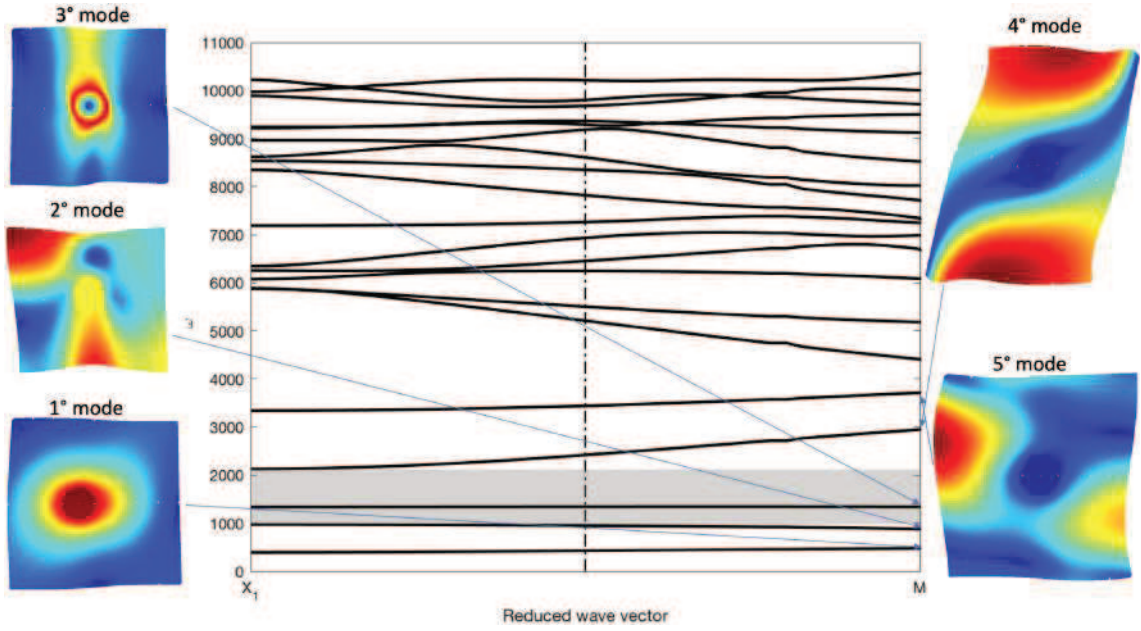


Figure 5.11: First five modes of propagation in the  $X_1 - M$  direction for  $k = 1$ .

## 5.6 Transmission Curves

### 5.6.1 Pressure Wave Polarization

As in previous cases analyzed, in this section Transmission curves are calculated and compared with the dispersion ones, in order to understand and confirm the existence of the frequency bandgap. Again, pressure and shear polarization wave response analysis are carried out and plotted in figures 5.12 and 5.14 as previously described in "Wang: Transmission Curves" chapter. As one can notice from picture 5.12, dispersion and transmission curves are plotted and compared, considering a common frequency axis representing the frequency range starting from  $0\text{ Hz}$  to  $1400\text{ Hz}$ . This kind of representation allows to compare bandgap width. One can notice that the pressure wave polarization bandgap, that is described through the second and fourth mode of the dispersion curve (longitudinal propagation modes), doesn't fit perfectly the dispersion curve one. This could be due to the preliminary mesh, too much coarse to capture the right frequencies in a better way. Unfortunately, mesh is deliberately coarse, for computational costs reasons, but for this preliminary analysis, obtained results are considered satisfactory.

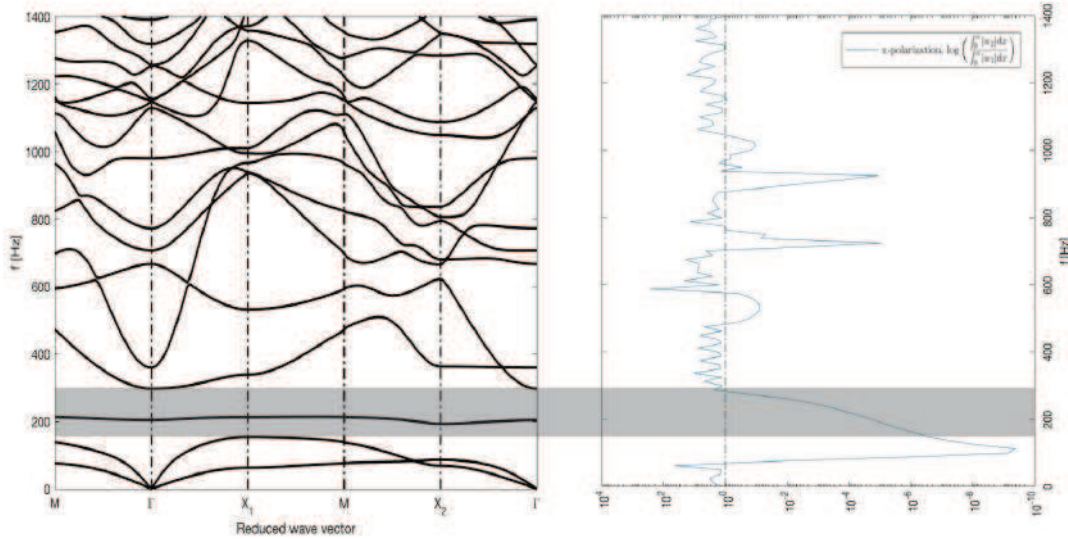


Figure 5.12: Comparison between Melamine-Aluminum metamaterial dispersion and transmission curves for pressure wave polarization case.

For the pressure wave polarization case the modes of propagation through the eight-cell array for the most relevant points has been analyzed in figure 5.13.

### 5.6.2 Shear Wave Polarization

For the shear wave polarization case, looking at figure 5.14 one can notice that the dispersion curve bandgap fits better then the pressure wave polarization case. Recalling figures 5.7, 5.8, 5.9, 5.10 and 5.11, it is possible to see the shear contribution of the third torsional mode on the shear wave polarized transmission curve around  $200\text{ Hz}$ .

In this case, bandgap extremes modes are transversal with respect the main propagation direction, and bandgap itself is wider than the previous one.



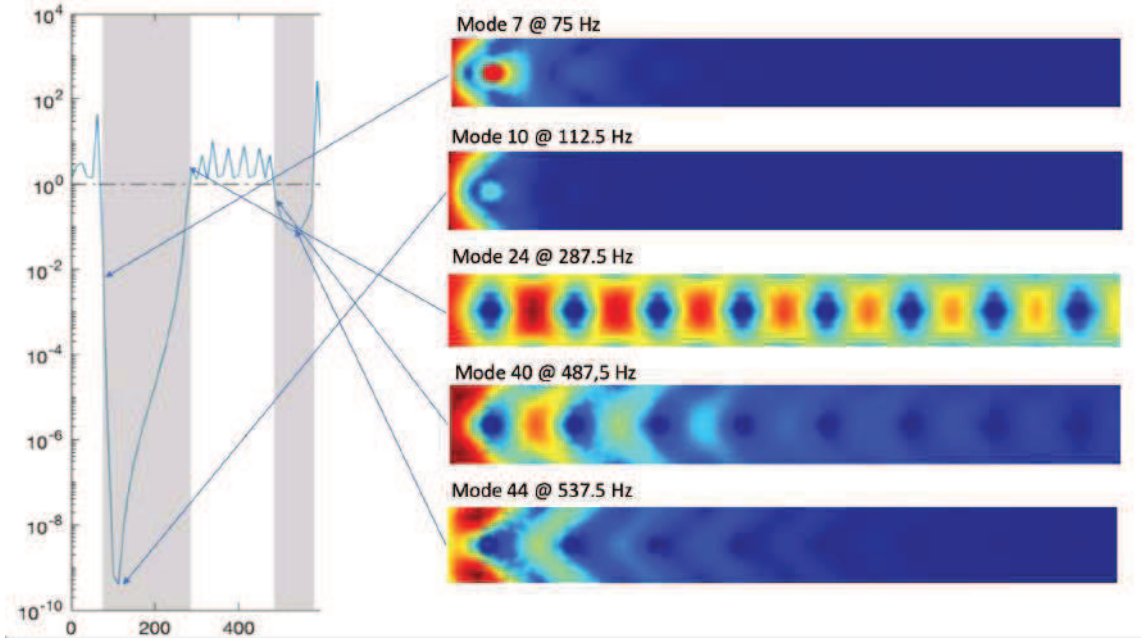


Figure 5.13: Mode propagation analysis of the most relevant points of pressure wave polarization transmission curve.

The effective bandgap is the one having the longitudinal modes as extreme modes, due to the fact that is within the wider transversal bandgap. In other words, all the kinds of waves don't propagate at all only within the pressure wave polarized bandgap.

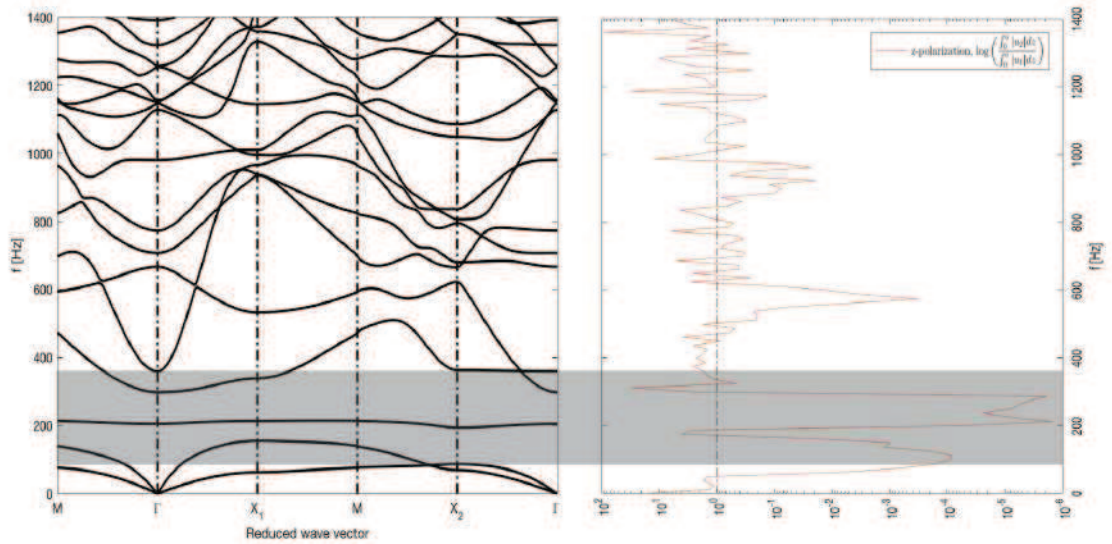


Figure 5.14: Comparison between Melamine-Aluminum metamaterial dispersion and transmission curves for shear wave polarization case.

## 5.7 Parametric Analysis

This final section aims to provide some results concerning the variation of the frequency bandgap width by changing the Aluminum inclusion diameter.

Naturally, if the diameter of the inclusion tends to 0, namely there is no inclusion into melamine matrix, obviously the bandgap does not exist.

The parametric results are listed in figure 5.15. The graph has been obtained by replicating the analysis for eleven times, by covering a Volume fraction  $Vf$  range starting from 0 to 0.0267, that is the maximum value that is allowable for boundary constraint reasons.

As before, the side length of the Unit Cell remains fixed at the value of 5 cm, meanwhile the expression that link all the parameter with the volume fraction is shown previously (eq. 5.1).

Lower abscissa refers to the volume fraction variation, meanwhile the upper one shows for every  $Vf$  value the difference between the upper and the lower bandgap extreme, namely the bandgap width.

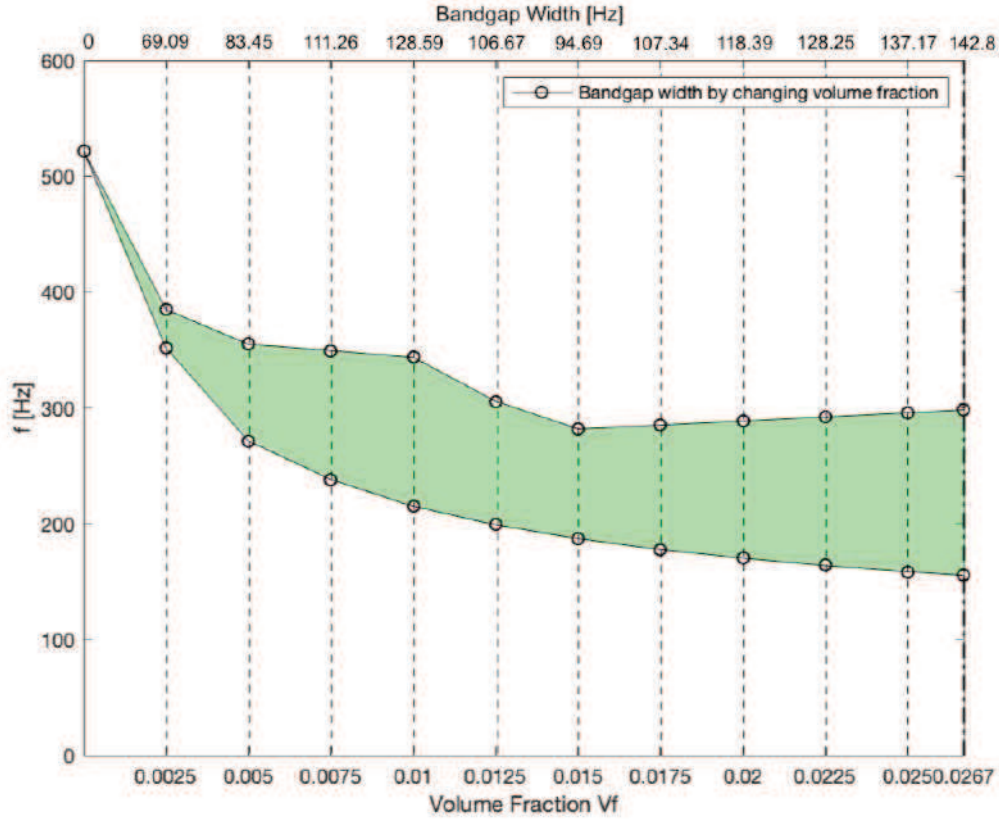


Figure 5.15: Bandgap width by varying the volume fraction of the Unit Cell

As is possible to observe looking at the graph, the more the volume fraction increase, the more the bandgap lower extreme maximum decreases with a smooth steepness approaching the boundary constraint  $Vf = 0.0267$ . Moreover, the bandgap lower extreme maximum has a peak where  $Vf = 0.01$ , then decreases until  $Vf = 0.015$  where reaches its minimum value and then slowly increases until more or less the frequency value of  $300\text{Hz}$ . In figure 5.16, is reported as a

series of images, the graphical evolution of the dispersion curves as the volume fraction increases.

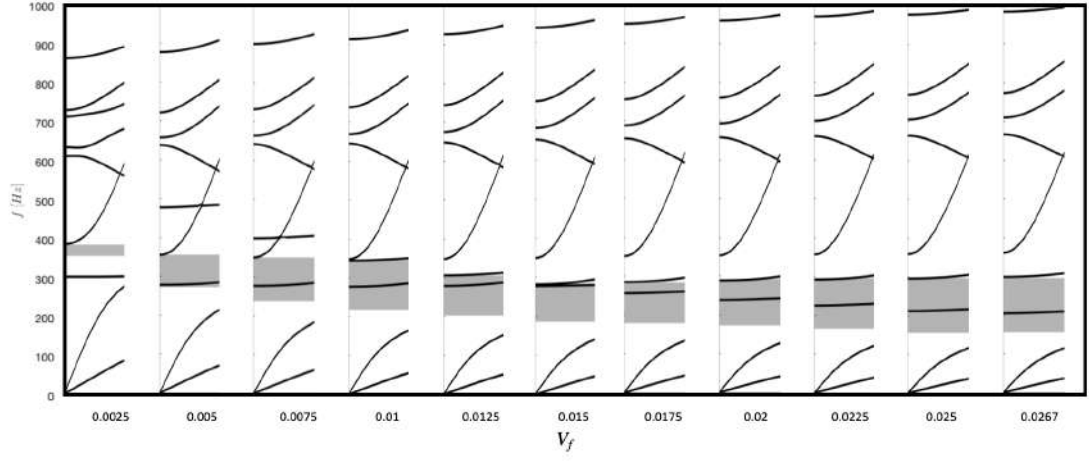


Figure 5.16: Graphical evolution of the bandgap width by increasing volume fraction.



## Chapter 6

# Conclusions

As far as this thesis work is concerned, it is worth to highlight its main desired goals that has been achieved:

- Implement a CUF tool able to provide dispersion curves;
- Test the CUF tool by using benchmarks;
- Obtain transmission curves with the aim to locate and compare bandgap frequency range with respect dispersion curves;
- Analyse the problem proposed by CASTLE project and plot dispersion and transmission curves;
- Carry out a parametric analysis in order to find out the maximum width of the frequency bandgap.

Naturally, as highlighted in chapter 5, in order to carry out a very precise analysis, viscoelasticity should had to be considered and correctly implemented.

The future developments of the study will first have to implement viscoelasticity to obtain new and more precise results.

After that, new dispersion curves can be plotted considering a thicker mesh and new transmission curves can be studied taking into account an higher number of unit cells. This could improve the benchmark between the two curves in terms of bandgap position.

Further development to this work can be done by carrying out dynamic homogenization starting from the heterogeneous material. Then, it could be possible to move from the preliminary study to the problem application, namely, to create a curved tube-shaped layer of metamaterial, and to study the effective soundproofing properties when the system is subject to a real range of frequencies.

Bt implementing the complex solver to the  $MUL^2$  micromechanics code, it is possible to obtain the imaginary dispersion curves, that wil be able to reveal evanescent modes and will provide more information about bandgaps that could be useful in understanding the behaviour of the system.



# Bibliography

- [1] M. Cinefra, G. Petrone, “SEA analysis in the cabin of a regional turboprop with metamaterial lining panels” in *AIAA Scitech Forum*, 7-11 January 2019.
- [2] M. Cinefra, G. D’Amico, A. De Miguel, M. Filippi, A. Pagani, E. Carrera, in “Numerical evaluations of transmission loss in acoustic metamaterials for aeronautical applications”
- [3] E. Carrera, M. Cinefra, M. Petrolo, E. Zappino, *Finite Element Analysis of Structures through Unified Formulation* Wiley, 2014.
- [4] W. Yu, *Multiscale Structural Mechanics* Wiley, 2016.
- [5] S. H. Lee, O. B. Wright, “Origin of Negative Density and Modulus in Acoustic Metamaterials” in *Phys. Rev. B*, v. 93, p. 024302, Jan 2016.
- [6] S. Huber, *Mechanical Metamaterials* ETH, Zurich, ETH, 2018.
- [7] Z. Liu, X. Zhang, Y. Mao, Y. Zhu, Z. Yang, C. Chan, P. Sheng, “Locally resonant sonic materials” in *Science*, v. 289, pp. 1734–1736, 2000.
- [8] A. Srivastava, “Elastic Metamaterials and Dynamic Homogenization: A Review” in *arXiv:1411.3001 [cond-mat.mtrl-sci]*, February 2015.
- [9] P. Langlet, A. C. Hladky-Hennion, J. N. Decapigny, “Analysis of the propagation of plane acoustic waves in passive periodic materials using the finite element method” in *The journal of Acoustical Society of America*, v. 98, 2792, pp. 286–300, 29th May 1995.
- [10] A. Sridhar, V. G. Kouznetsova, M. G. D. Geers, “Homogenization of locally resonant acoustic metamaterials towards an emergent enriched continuum” in *Comput Mech*, v. 57, pp. 423–435, 8th February 2016.
- [11] Y. Wang, Y. Wang, V. Laude, “Wave propagation in two-dimensional viscoelastic metamaterials” in *Phys. Rev. B*, v. 92, p. 104110, September 2015.
- [12] Y. Wang, Y. Wang, L. Wang, “Two-dimensional ternary locally resonant phononic crystals with a comblike coating” in *J. Phys. D:Appl.Phys.*, v. 47, December 2014.
- [13] Wikipedia contributors, “Melamine — Wikipedia, The Free Encyclopedia” 2019, [Online; accessed 18-June-2019]. [Online]: <https://en.wikipedia.org/w/index.php?title=Melamine&oldid=902295996>
- [14] S. Hashmi, F. Bathalta, C. Van Tyne, Y. Bekir, *Comprehensive Material Processing* Elsevier, 2014.
- [15] Wikipedia contributors, “Metamaterial — Wikipedia, The Free Encyclopedia” 2019, [Online; accessed 2-July-2019]. [Online]: <https://en.wikipedia.org/w/index.php?title=Metamaterial&oldid=903198122>
- [16] —, “Marie Skłodowska-Curie Actions — Wikipedia, The Free Encyclopedia” 2019, [Online; accessed 10-July-2019].
- [17] R. Walser, “Metamaterials: what are they? What are they good for?” in *APS March Meeting Abstract*, p. 5001, 2000.

- [18] T.-Y. Huang, C. Shen, Y. Jing, “Membrane- and plate- type acoustic metamaterials” in *The Journal of Acoustical society of America*, v. 3240-3250, pp. 1734–1736, June 2016.
- [19] Z. Liu, X. Zhang, Y. Mao, Y. Zhu, Z. Yang, C. Chan, P. Sheng, “Locally Resonant Sonic Materials” in *Science*, v. 289, pp. 1734–1736, September 2000.
- [20] Wikipedia contributors, “Wavelength — Wikipedia, The Free Encyclopedia” 2019, [Online; accessed 22-May-2019]. [Online]: <https://en.wikipedia.org/w/index.php?title=Wavelength&oldid=898267104>
- [21] T. Chang, L.-Y. Wu, C.-N. Tsai, L. Chen, “A multilayered acoustic hyperlens with acoustic metamaterials” in *Applied Physics A*, v. 103, pp. 355–359, 2011.
- [22] M. Chen, D. Meng, H. Jiang, Y. Wang, “Investigation on the Band Gap and Negative Properties of Concentric Ring Acoustic Metamaterial” in *Shock and Vibration*, v. 2018, January 2018.
- [23] K. H. Matlack, A. Bauhofer, S. Krödel, A. Palermo, C. Daraio, “Composite 3D-printed metastructures for low-frequency and broadband vibration absorption” in *Proceedings of the National Academy of Sciences*, v. 113, n. 30, pp. 8386–8390, 2016. [Online]: <https://www.pnas.org/content/113/30/8386>
- [24] P. Celli, “Methods to Compute the Dispersion Relation for the Wave Propagation Characterization of a Periodic Medium” in *Department of Civil, Environmental, and Geo - Engineering University of Minnesota*, October 2014.
- [25] A. G. de Miguel, *MUL2-UC: Micromechanics code: beam modeling of periodically heterogeneous composites*, Politecnico di Torino, 24 Corso Duca degli Abruzzi, 10129 Turin (TO), Italy, June 9th, 2017.
- [26] A. G. de Miguel, A. Pagani, W. Yu, E. Carrera, “Micromechanics of periodically heterogeneous materials using higher-order beam theories and the mechanics of structure genome” in *Composite Structures*, pp. 484–496, 10th August 2017.
- [27] W. Yu, “A unified theory for constitutive modeling of composites” in *J Mech Mater Struct*, v. 41(6), 2016.
- [28] V. Berdichevskii, “On averaging of periodic systems” in *J Appl Math Mech*, v. 41(6), pp. 1010–23, 1977.
- [29] E. Carrera, A. G. de Miguel, A. Pagani, “Hierarchical theories of structures based on Legendre polynomial expansions with finite element applications” in *Int J Mech Sci*, v. 120, pp. 286–300, 2017.
- [30] A. Sridhar, V. Kouznetsova, M. Geers, “Homogenization of locally resonant acoustic metamaterials towards an emergent enriched continuum” in *Comput Mech*, v. 57, pp. 423–435, February 2016.
- [31] L. Brillouin, *Wave Propagation in Periodic Structures*, Dover, New York, 1953.
- [32] Wikipedia contributors, “Brillouin zone — Wikipedia, The Free Encyclopedia” 2019, [Online; accessed 26-March-2019]. [Online]: <https://en.wikipedia.org/w/index.php?title=Brillouin.zone&oldid=886197840>
- [33] J. Rayleigh, *The theory of sound* London, Macmillan and Co., 1877.
- [34] L. Beranek, *Noise Reduction* NY, McGraw-Hill Book Company Inc., 1960.